Analysis of the Dissolution Behaviour of Flax Based Yarn in an Ionic Liquid

James. E. Hawkins

University of Leeds

School of Physics and Astronomy

Submitted in accordance with the requirements for the degree of

Doctor of Philosophy

January 2021

The candidate confirms that the work submitted is his own, except where work which has formed part of jointly authored publications has been included. The contribution of the candidate and the other authors to this work has been explicitly indicated below. The candidate confirms that appropriate credit has been given within the thesis where reference has been made to the work of others.

I would like to dedicate this thesis to my grandfather, whose support and encouragement have made this possible.

Acknowledgements

I would like to take the time briefly acknowledge some of the people who have made this whole process feel seamless.

As is the case with PhD research, there have been moments of progress and moments of despair. Fortunately, however, the former has been far more frequent during this work. I believe that the frequency and magnitude of these breakthroughs has been of a direct result of the flawless supervision provided by Prof. Michael Ries and Dr. Peter Hine. It has been a pleasure to work with such enthusiastic and helpful supervisors, always full of good ideas (and tea/coffee!)

To have been part of such a friendly, diverse and ever-growing research group has been a joy. Of this group, I would like to thank Yunhao Liang in particular for our many hours of meandering discussion, from which many interesting ideas and insights came.

Dr. Dan Baker has in many ways acted as the glue holding the PhD together- working tirelessly to have the research equipment in working order and always willing to lend a hand (though it was normally a hand covered in ionic liquid from a spillage on my part, apologies Dan!)

I would also like to thank Stuart, Trevor, Will, Keith and Leigh of the mechanical workshop for constantly giving their full imagination and expertise when building vital pieces of apparatus for us.

Lastly, but perhaps most importantly, I would like to acknowledge the unparalleled support of my family, who have had to bear with me mulling over ideas and mumbling to myself about cellulose at the dinner table for the past few years.

The pandemic has impacted our research in many ways, but our online meetings have been just as enjoyable and productive as they were in person – each one overrunning just as much as they used to in the real world, too full of new ideas to wrap up on time!

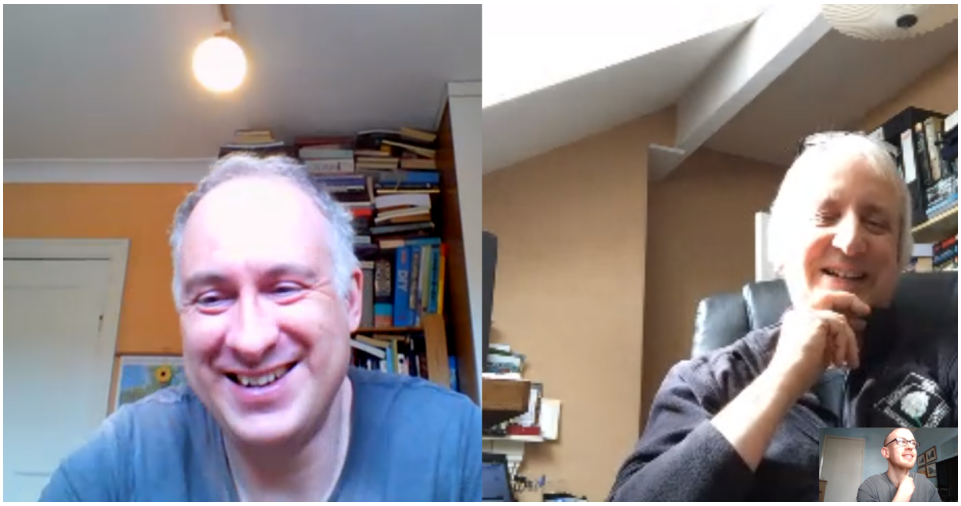

Weekly meeting on Microsoft Teams during the COVID pandemic.

Author's Publications

Time temperature superposition of the dissolution of cellulose fibres by the ionic liquid 1-ethyl-3-methylimidazolium acetate with cosolvent dimethyl sulfoxide

James E Hawkins, Yunhao Liang, Michael E Ries, Peter J Hine
Carbohydrate Polymer Technologies and Applications, Volume 2, 2021, 100021
ISSN 2666-8939
https://doi.org/10.1016/j.carpta.2020.100021.

Dissolution of cotton by 1-ethyl-3-methylimidazolium acetate studied with time–temperature superposition for three different fibre arrangements

Liang, Y., Hawkins, J.E., Ries, M.E. et al.
Cellulose, 28, 715–727 (2021). 19 November 2020
ISSN 0969-0239
https://doi.org/10.1007/s10570-020-03576-x

Abstract

Flax based yarn has been dissolved in the ionic liquid 1-ethyl-3-methylimidazolium acetate [C2mim][OAc] and the dissolution behaviour studied as a function of time, temperature, co-solvent and anti-solvent concentration. With pure ionic liquid, dissolution is seen to occur from the outside in, with a coagulated outer layer forming and growing around the fibrous core with time. Following dissolution, yarns were coagulated in water and left to dry at room temperature. Three key methods of analysis have been used to study the resultant yarns: optical microscopy, X-ray diffraction and mechanical testing- with each method allowing for a distinct means of tracking the amount of dissolution. The resulting data displays an equivalence between dissolution time and temperature, verified by the creation of master curves via the shifting of data sets in the time domain, much like time-temperature superposition in rheological systems. The shift factors used to generate master curves have been plot against the inverse of their respective dissolution temperatures and upon doing so, a linear relation has revealed Arrhenius behaviour in the system. As a result, an activation energy has been calculated describing the energy needed for the dissolution of flax yarns in [C2mim][OAc]. This energy was found to be 100 $\pm$ 10 kJ/mol, with agreement across the various experimental techniques.

With the introduction of the co-solvent dimethyl sulfoxide (DMSO), the growth of the coagulated material is again found to follow an Arrhenius equation with a single activation energy of 98 $\pm$ 2 kJ/mol. This value is, surprisingly, independent of the weight fraction of DMSO. The addition of DMSO does, however, strongly alter the time-scales taken for dissolution, but interestingly not the temperature dependence of these time-scales. The composition for the peak dissolution

rate is determined, which occurs at an equal weight fraction of DMSO and [C2mim][OAc].

The inclusion of small amounts of the anti-solvent water has also been found to drastically alter the time-scales of dissolution, with a sharp exponential decay in the dissolution rate seen as a function of H_2O concentration. Despite the substantial effect of water on the dissolution rate, the activation energy is found to be remarkably constant-within error of the activation energies determined when using both pure ionic liquid and ionic liquid/co-solvent mixtures. As little as 8 % water by weight is shown to be sufficient to halt the dissolution process on experimental time-scales.

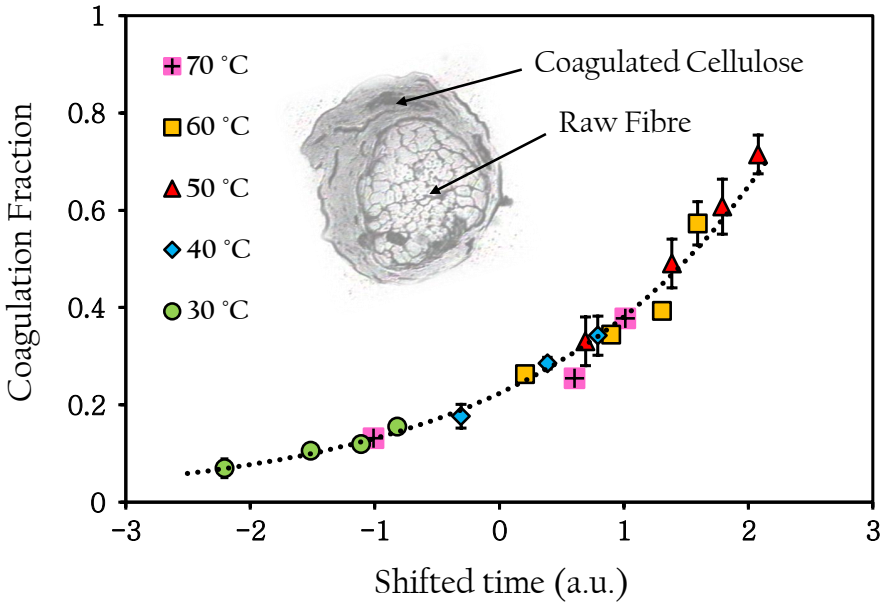

Graphical Abstract

Contents

List of Figures

Chapter 1

Introduction

1.1 Cellulose

Cellulose, first discovered in 1838 by Anselme Payen [1] is a naturally occurring linear biopolymer consisting of D-anhydroglucopyranose units joined by $\beta(1\rightarrow4)$ glyosidic bonds [2] - the molecular structure of which can be seen in Figure 1.1. Found primarily in the cell wall of plants, alongside other polysaccharides and lignin, it provides strength and rigidity to plant stems, leaves and branches. Cellulose is the most abundantly available raw material on Earth [3] and has a highly ordered crystal structure [4, 5, 6], giving rise to impressive mechanical properties [7, 8]. Within biomass, cellulose forms helical micro-fibrils and can be found in both crystalline and amorphous states. This polymer can also be obtained in micro-crystalline form from algae, bacteria, fungi and several other living species [9, 10]. The degree of polymerisation of cellulose can vary widely depending on its source, ranging from a few hundred in wood pulp to a few thousand in cotton [11, 12].

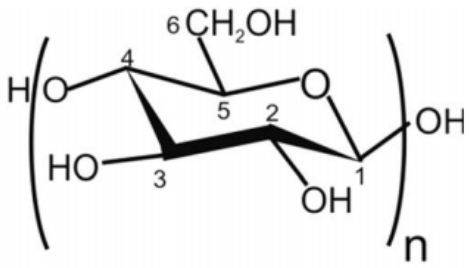

Figure 1.1: The repeat unit of cellulose, consisting of a single glucose molecule. Credit: French et al. [13]

Cellulose polymers attract each other via van der Waals forces and hydrogen bonds (h-bonds) to form small sheets, which in turn stack to form the micro fibril [5, 14]. The presence of many intra- and inter-molecular h-bonds as seen in figure 1.2 play an important role in the stabilising and stiffening of cellulose chains - as such bonds prevent the free rotation of the rings along the chain axis. There are three distinct types of hydrogen bonds within native cellulose, differing in their bond distances (ranging from 1.7 to 1.9 Å) and strength (with energies found between 8.6 and 14.9 kJ/mol.) [15].

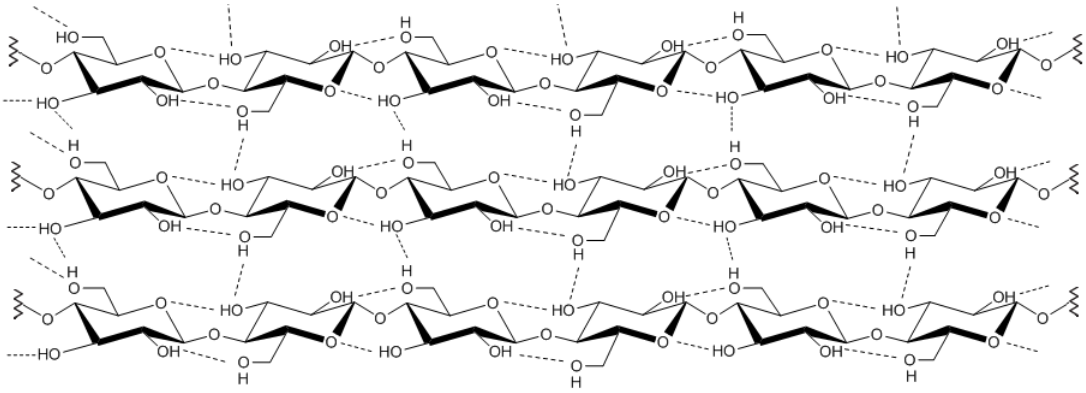

Figure 1.2: The inter- and intra molecular h-bond network within native cellulose. Credit: W. Pires [16]

Cellulose features a monoclinic unit cell and is found in nature to exist in two sub-forms - Iα alpha and Iβ. Though remarkably similar, these structures differ in the relative displacement of their cellulose sheets and have slightly different unit cell parameters [17]. Both sub-forms can be found existing alongside each other, even along a given micro-fibril. Figure 1.3 displays the Cellulose Iα unit cell.

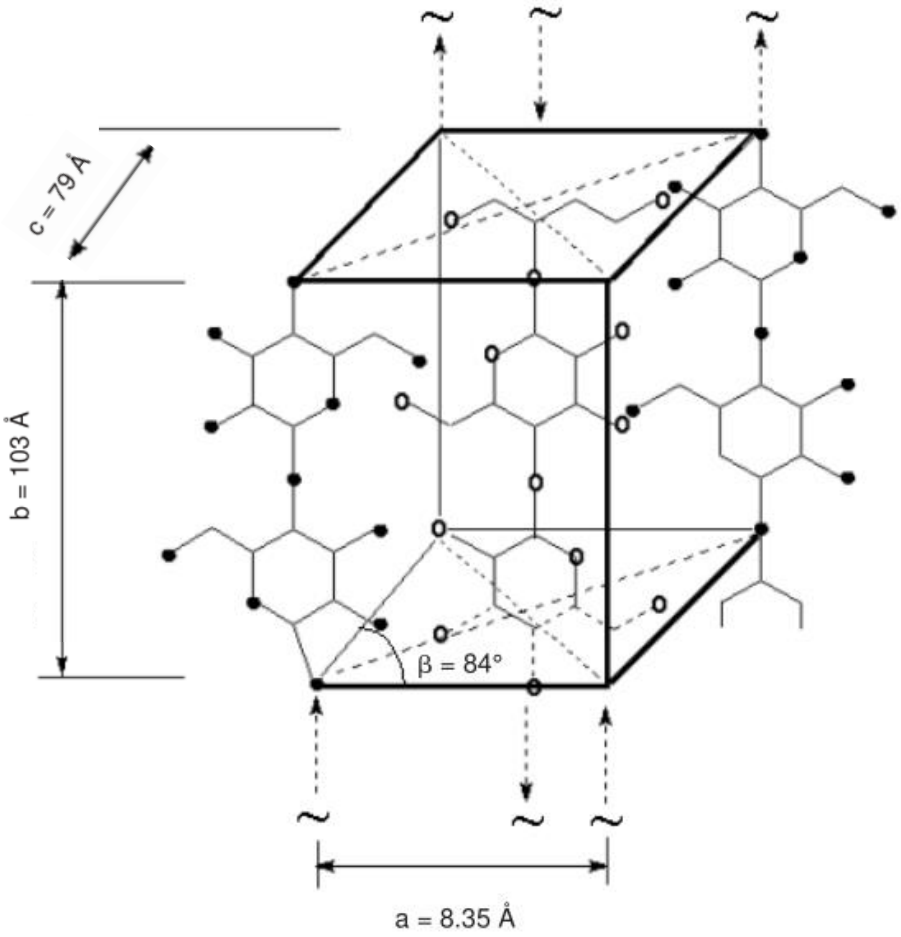

Figure 1.3: The unit cell of cellulose I. Image adapted from the work of Horne et al. [18]

Alongside the well studied 'cellulose I', another common allomorph- 'cellulose II' is often documented. Cellulose I may be converted into cellulose II (a transition elaborated on in section 1.8), however; subtle structural differences between the two result in a thermodynamic favourably of the latter- rendering the transition irreversible. Such differences include the packing orientation and intra-molecular h-bond locations (see figure 1.4) [19]. The polymer chains, which align themselves parallel in CI, exist in an antiparallel configuration in CII [20]. At least four other allomorphs of cellulose have been identified and can be created via chemical modifications or by treating with liquid ammonia [21, 6]. The work presented in this thesis however, focuses exclusively on the cellulose I and II structures.

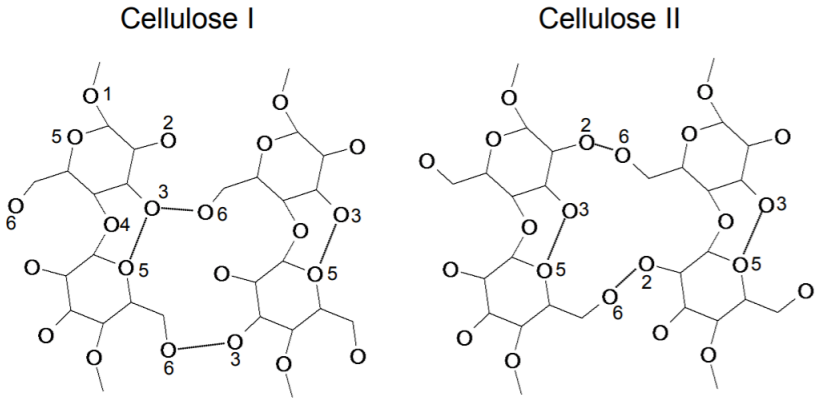

Figure 1.4: The differing hydrogen bond locations between cellulose I and II. H-bonds shown with solid, dark lines. Credit: Blackwell et al. [17].

Cellulose, like many polymer systems, features both crystalline and amorphous regions. For this reason, the polymer is described as 'semi-crystalline'. Such regions can often exist adjacent to each other along the axis of a micro-fibril and individual cellulose chains may pass through many crystalline-amorphous boundaries [22, 23]. See Figure 1.5.

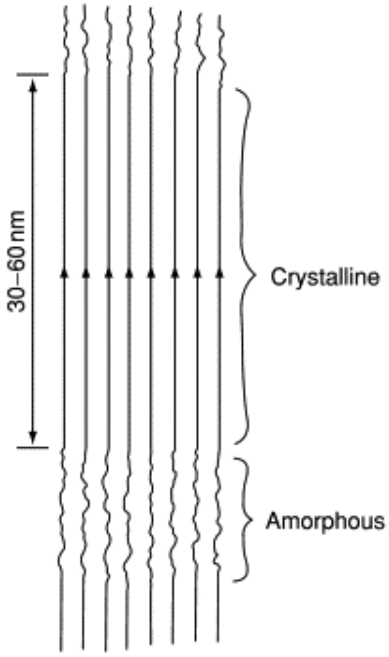

Figure 1.5: Theoretical microstructure of a cellulose microfibril, showing the highly ordered crystalline regions which alternate with less ordered amorphous segments. (Known as the traditional 'two phase' model.) Credit: W. Pires [24]

Cellulose features many hydroxyl groups, giving the polymer a high level of hydrophilicity, though the presence of hydrophobic planes within the crystal structure are also well documented [25, 26]. Figure 1.6 highlights both the hydrophobic and hydrophilic areas surrounding the cellulose polymer.

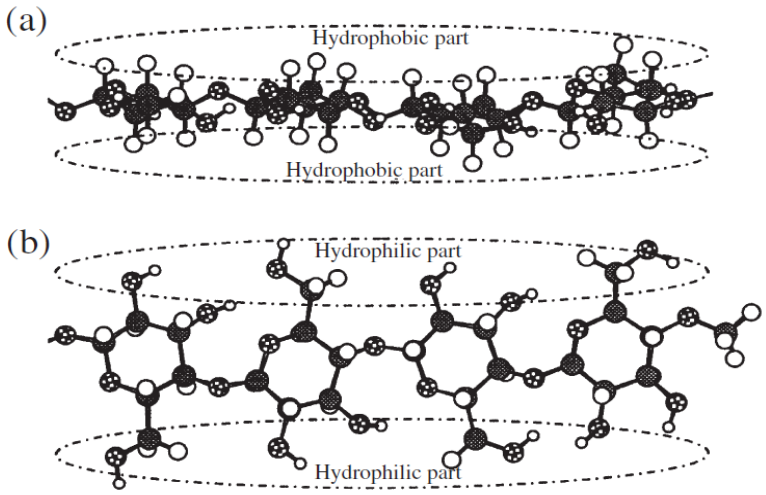

Figure 1.6: Hydrophobic and hydrophilic parts of the cellulose molecule: (a) side view of the glucopyranose ring plane highlighting the hydrophobic regions and (b) front view of the glucopyranose ring plane showing the hydrophilic locations. Credit: Yamane et al. [27]

1.2 Flax

Flax is a naturally occurring bast fibre and is used as the source of cellulose during this work. The flax plant grows worldwide and has been used for its textile, mechanical and edible properties for over 30,000 years [28]. Flax is cheap and plentiful, with over 2.7 million tonnes produced during 2017 alone [18]. This plant will grow in almost any climate, even with poor soil quality [29] and is commonly

found to consist of approximately 70 % cellulose and 27 % hemicellulose, with a small amount of lignin (3%) [30]. The flax fiber is also one of the longest known linear textile polymers, with a degree of polymerisation of around 4,000 [31, 32]. These long polymer chains allow for the formation of many inter-chain bonds, stiffening the polymer system and resulting in a high tensile modulus relative to other natural fibres, such as cotton or hemp [33, 34].

1.3 History of Cellulose Processing

As a result of the strong bonding network within cellulose, the polymer is both chemically and thermally stable - making it highly resistant to dissolution in traditional solvents such as water or ethanol [35, 36, 37]. It is also naturally recalcitrant to microbial and enzymatic degradation [38].

Despite these complications, the dissolution and processing of cellulose is still an area of great interest- as many industrial procedures rely on the controlled deconstruction of this polymer in order to make fuels, chemicals and materials [39]. The pulping industry, for example, uses an acidic solution in conjunction with heat and pressure to process wood chips and bark. The creation of cellophane involves the dissolution of cellulose and areas within bio-composite science require the partial dissolution of fibres in the preparation of eco-friendly composites [40, 41]. Dissolution is crucial, as unlike many petroleum-based polymers, cellulose will not melt but decompose at elevated temperatures [42]. Decomposition will occur at different temperatures depending on the source of cellulose, though normally occurs around 300 °C [1, 43]. Though dissolution is not totally understood, there is a consensus that solvents must be able to disrupt the strong inter- and intra-molecular interactions (both h-bonds and hydrophobic forces) within the crystal [44, 15, 45]. The earliest mention of cellulosic dissolution dates back to 1894, when English chemists Charles F. Cross, Edward J. Bevan and Beadle Clayton dissolved wood pulp using aqueous sodium hydroxide in the presence of carbon disulphide [46]. This procedure eventually became known as the 'Viscose' process and is widely used commercially to this day, despite the corrosive nature of the solvents used [47].

The structural modification of the cellulose polymer has been commonplace since the mid-1800's. Such modifications have included the reaction of cellulose with acetic anhydride to produce cellulose acetate, or nitric acid to produce nitrocellulose [48, 49]. These modified variants of the polymer are processable with common industrial solvents and have led to the production of such things as rayon fibres [50].

Recently, a new class of solvents for cellulose- known as 'ionic liquids' have become increasingly popular. These eco-friendly liquid salts are to be described in detail in section 1.6.

The physics underlying cellulosic dissolution at the microscopic level is still debated, as commonalities between different solvents are not immediately evident [51]. The non-covalent interactions binding the cellulose chains together appear to constitute the main barrier to processing and require a solvent to be able to diffuse into the structure in order to facilitate dissolution [52].

1.4 Dissolution Mechanics

As mentioned in section 1.1, cellulose features a robust hydrogen bond network. It is widely believed that in order to dissolve cellulose, a solvent must be able to infiltrate the polymer network and supplant these bonds [53, 54, 55]. A solvent's ability to modify cellulosic biomass is often hindered however, by either 'direct' or 'indirect' factors. An example of a direct factor may be a limited amount of exposed surface area, whereas the amount of crystallinity/degree of polymerisation may be considered indirect factors [56]. Such barriers to dissolution are in part caused by the complex interlinks between cellulose and other substances within plant mass- such as lignin, pectin and hemicelluloses [57]. During dissolution, it is theorised that individual cellulose chains are 'peeled' away from the crystal lattice- as show in Figure 1.7 [37].

In order to negate some of these obstacles, pre-treatments are often used with the aim of increasing the solvent/enzyme accessibility of cellulose. These pre-treatments can be as simple as swelling the polymer, though more complex treatments are used when attempting to remove any unwanted components of plant biomass, such as hemicelluloses. These simple polysaccharides create a physical hindrance to dissolution due to their sprawling, amorphous nature within the crystal lattice. In order to remove hemicelluloses; they are often hydrolysed by dilute acids or destroyed via steam explosion treatment [58]. The latter method involves the exposure of cellulosic biomass to high-pressure steam, followed by a rapid reduction in pressure- resulting in an explosive decompression of the material and a breakdown of the lignocellulosic matrix [59].

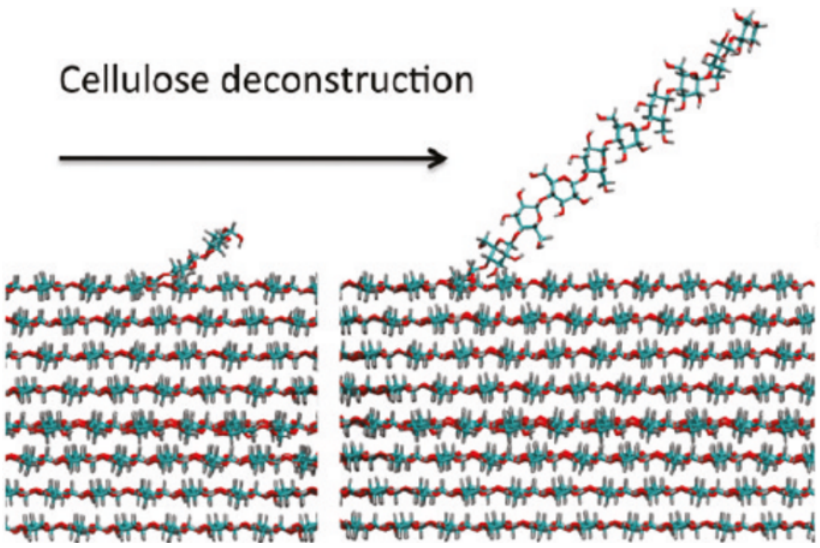

Figure 1.7: Snapshots of the peeling away of a glucan chain during the dissolution process. Credit: Cho et al. [37]

When cellulose (like many polymeric systems) is placed in contact with a suitable solvent, dissolution occurs in three main steps. The first of these steps involves the swelling of the polymer network at the polymer-solvent interface.

Next, the swollen fraction allows for chains to begin to disentangle themselves and finally, chains are able to migrate out into the solvent [60, 61]. These steps can be seen diagrammatically in Figure 1.8. Moigne et al. report that the escaping of these chains occurs at an early stage of the dissolution process [62]. Dissolution occurs from the outside inwards and mechanisms are similar for crystalline and amorphous zones, differing only in terms of kinetics [63].

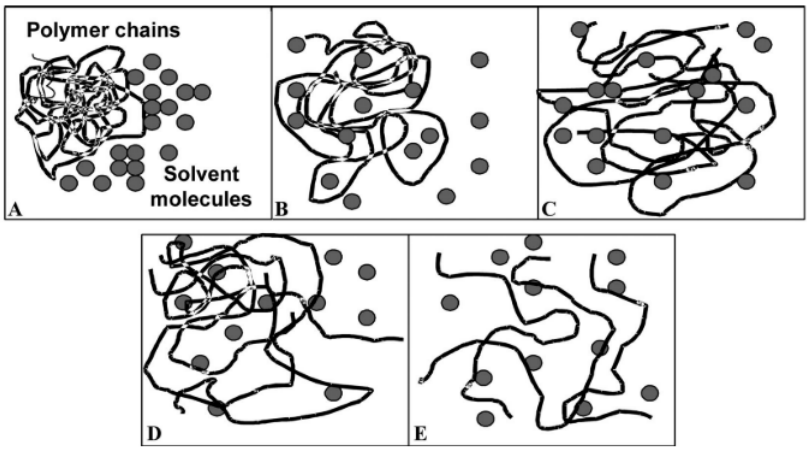

Figure 1.8: Dissolution of a solid polymer system in a solvent as a function of time. A) Two separate phases, consisting of the polymer chains and the solvent molecules B) Gradual movement of the solvent molecules into the polymer network as the solute begins to swell C) Swelling increases up to the point of chain disentanglement D) Chains continue to untangle themselves and move out into the solvent E) Solubilization is completed, resulting in a homogeneous solution comprised of cellulose chains dispersed throughout the solvent. Credit: LeMoigne et al. [62]

A process commonly reported during the dissolution of cellulose fibres is that of 'ballooning'. This results from the way in which select zones along the fibre tend to swell more than others- giving the appearance of balloons along the fibre axis. See figure 1.9. [64, 65]

Multiple authors have identified at least three distinct dissolution modes in nat-

ural polymeric systems:

(i) Fast dissolution by fragmentation.
(ii) Swelling by ballooning and full dissolution.
(iii) Swelling by ballooning and no complete dissolution.

The observed mode appears to be heavily dependent on the concentration of water within the solvent, as well as the solvents ability to disrupt the long range order of cellulose chains [66, 67].

Figure 1.9: The swelling and ballooning of wood fibers in the solvent N-Methylmorpoline N-oxide. Credit: Singh et al. [68]

Though the consensus within literature is that dissolution relies on a solvent's ability to "effectively destroy inter-chain hydrogen bonding within cellulose", [69] this idea has not gone uncontested. The 'Lindman Hypothesis' for example, forwarded by Björn Lindman 2010 argues that hydrophobic interactions play as large, if not a larger role in dissolution than the breaking of hydrogen bonds [70].

Lindman's postulations relate to the insolubility of cellulose in water. If, as is commonly agreed upon in the literature, the ability of a solvent to form/supplant h-bonds is the only pertinent factor- then the strong tendency of water molecules to create such bonds should result in a high level of cellulose solubility, not the opposite. It is pointed out that other polysaccharides, such as dextrins, *are*

soluble in water.

Björn also documents how the strength of water-water, water-carbohydrate and carbohydrate-carbohydrate interactions are all very similar in magnitude, implying that water should be able to compete for h-bonds with the carbohydrate. He also points out that 'number of hydroxyl groups with protons capable of forming hydrogen bonds is actually less than the number of oxygen atoms that would like to form such bonds' and thus 'in the presence of excess water, cellulose should be highly soluble if hydrogen bonding is the sole interaction.'

Cellulose, like many polymers, is amplillic. Amphiphilic self-assembly is well documented for surfactants, lipids and block co-polymers, [71, 72] but seems neglected for homopolymers such as cellulose, claim Lindman et al. The authors postulate that the amphilicity and tendency to self organise in the presence of water may play an important role in the solubility of a polymer system. Within cellulose, for example, hydrophobic sides of the structure would have a tendency to sick to each other in an aqueous environment, thus lowering the solubility. Björn concludes by saying that there is 'strong evidence for cellulose being significantly amphiphilic and that the low aqueous solubility must have a marked contribution from hydrophobic interactions.'

There are of course, many critics of Lindman's hypothesis. Burchard et al. for example- argues that it is rather the interplay between hydrogen bonds, Van der Waals forces and hydrophobic interactions that should be considered during dissolution, claiming that hydrophobic interactions may only become an important factor after h-bonds are broken [73]. Others have claimed that Lindman et al. have neglected the entropic effect and that the differing degrees of polymerisation may account for the aqueous solubility of other, smaller carbohydrates [73].

This summary describing the dissolution of cellulose should hopefully elucidate the striking amount of complexity involved. It is clear that we are still far from a fully comprehensive understanding of cellulosic dissolution.

1.5 Conventional Solvents

Solvents for cellulose can be broadly split into two classes; 'Derivatizing' and 'Non-derivatizing' [74, 75]. The former class of solvents are used to convert cellulose into a product of similar chemical structure- known as the reaction 'derivative'. Examples of such derivatives may be methylcellulose, hydroxypropyl cellulose or carboxymethyl cellulose. Derivatising solvents aim to functionalise the cellulose hydroxyl groups, with functionalisation reactions including nitration, xanthation or estrification. By modifying the polymer in this way, intra- and inter-molecular h-bonds are disrupted with minimal chain degradation [76]. These modified variants of the polymer are soluble in common polar solvents, such as dimethylformamide or dioxane [77].

Non-derivatising solvents however, leave the polymer chemically unaltered. Examples include trifluoroacetic and formic acid [78], organic solvents in the presence of an inorganic salt [79], aqueous alkali solutions [80] and amine oxides [81]. Figure 1.10 elaborates on the multitude of solvents within each of these categories.

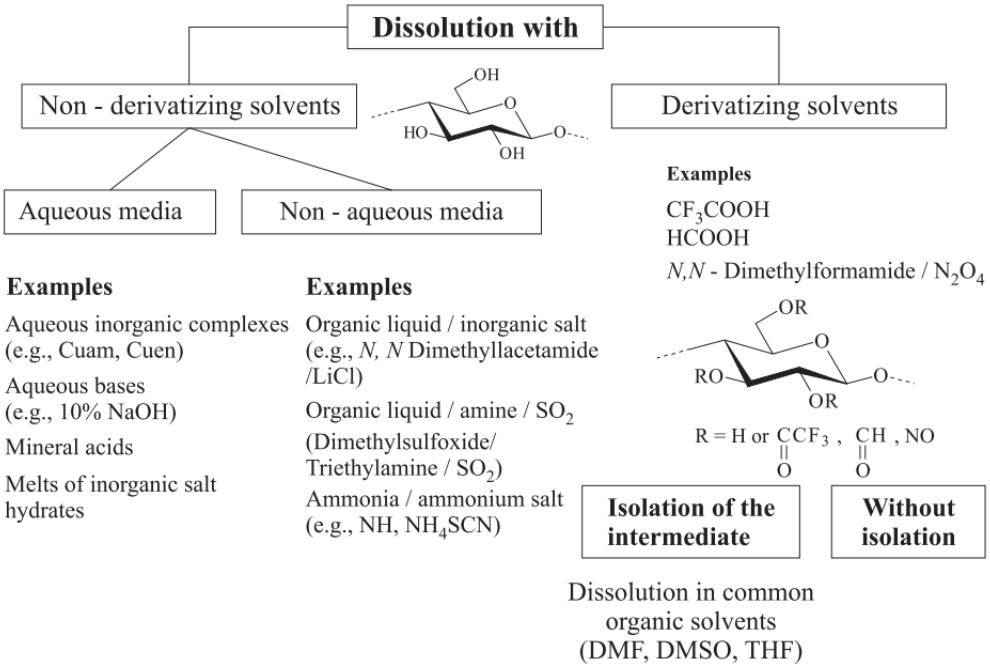

Figure 1.10: Classification of some common cellulose solvents. Credit: Heinze et al. [82]

1.6 Ionic Liquids

With the advent of ionic liquids, a new, 'environmentally friendly' method of cellulose dissolution has emerged [83, 84]. These liquids, used for everything from a liquid mirror in a space telescope [85] to a catalyst in CO_2 electro-reduction reactions [86] are salts in the liquid state below 100 °C and many have shown the ability to dissolve cellulose without the need for pre-treatments, such as swelling [40]. These viscous liquids consist of a large, organic cation in conjunction with a smaller anion and were first synthesised by Paul Walden in 1914, [87] though their huge potential to be used in industrial applications has only recently been realised [87, 88]. Ionic liquids feature many attractive properties as solvents; including low melting points, negligible vapour pressures, excellent solubility, high thermal stability, a wide liquid range, low melting points and potential recyclability [89, 90]. There are a huge number of potential IL's in theory, due to the vast number of possible anion/cations pairings, with the possible number of combinations postulated to be around a million [91, 92, 93]. Computational studies have suggested that ionic liquids featuring cations with short alky chains make for superior solvents [94]. It is widely accepted however, that the basicity of the cation must be greater than 0.8 in order for the dissolution of cellulose to occur [95, 86]. The ionic liquid used within this work is 1-ethyl-3-imidazolium acetate ([C2mim][OAc]), the molecular structure of which can be seen in Figure 1.11.

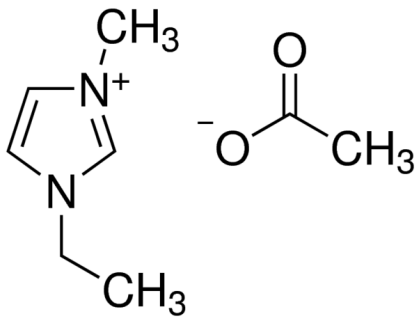

Figure 1.11: Molecular structure of the ionic liquid [C2mim][OAc], used as a solvent for cellulose during this study. The larger, positively charged cation is seen on the left and the smaller, negatively charged anion on the right.

IL's are typically categorised into four main groups based on their cation: 1) alkylammonium, 2) alkylphosphonium, 3) N,N'-dialkylimidazolium and 4) N-alkylpyridinium. Of these groups, the imidazolium-based are among the most studied [96, 97, 90]. The discovery of 1-ethyl-3-methylimidazolium [EMIM]-based chloroaluminate ionic liquids in 1982 resulted in an acceleration of activity surrounding room temperature ionic liquids (RTIL's) [90].

The viscosities of ionic liquids can be drastically changed with minor alterations such as variation in anion size or the addition of small amounts of carbohydrates and/or water [98, 99]. Among the most common IL's studied in conjunction with cellulose are 1-ethyl-3-methylimidazolium acetate (EMIMAc) and in 1-butyl-3-methylimidazolium chloride (BMIMCl), whereby the ion diffusivity and relaxation times have been measured as a function of carbohydrate concentration [100, 101]. The earliest mention of cellulosic dissolution using a molten salt (N-alkylpyridinium chloride) occurred in 1934, [102] though this does not qualify as an IL based on Walden's definition due to its high melting point. It is only recently (2002) that Swatloski et al. first published results describing the dissolution of cellulose in several ionic liquids, including 1-butyl-3-methylimidazolium hexafluorophosphate and 1-butyl-3-methylimidazolium chloride [103]. This seminal work has since influenced many publications and review papers [104, 46, 61].

Ionic liquids can, however, have undesirable side reactions when in contact with cellulose [105]. These interactions result in the production of liquid-sugar adduct species, making the prospect of recycling difficult. The reactive culprit of such side reactions is often one of the cationic carbons. This component could be exchanged for something less reactive, such as a methyl group- though this would alter the viscosity, increase the melting point and decrease thermal stability of the IL; making the modification of the cation a non-trivial problem [105].

1.7 Co-Solvents

Co-solvents are often used when processing cellulose as a means of lowering the cost of dissolution, but are also frequently used to modify the viscosity of the primary solvent [106, 107, 108]. In some cases, the addition of a co-solvent is not only preferable, but vital. The viscose process for example uses the addition of carbon disulphide in order to form cellulose xanthate, which only then can be dissolved in aqueous sodium hydroxide [82].

It is known that the dissolution of cellulose in ionic liquid/co-solvent systems is mainly mediated by the hydrogen bond interactions between the anions and cellulose hydroxyl protons, with co-solvents such as dimethyl sulfoxide, dimethylacetamide and pyridine indirectly influencing such interactions [109, 110]. Of the wide array of potential co-solvents; aprotic liquids with a high degree of polarity have been found to perform most optimally [111]. The solvation of ionic liquids by aprotic co-solvents is reported to produce more "free" anions from anion-cation pairs. Such anions will readily interact with cellulose, resulting in an increase in dissolution [112].

Protic co-solvents such as water and methanol however, *can* compete with the cellulose-anion interactions and hinder the dissolution process as a result [112]. Protic co-solvents are often used prior to dissolution with the aim of swelling the solute; as swelling allows for a greater level of penetration by the active solvent [113]. Common swelling agents include trifluoroacetic acid and phosphoric acid [114].

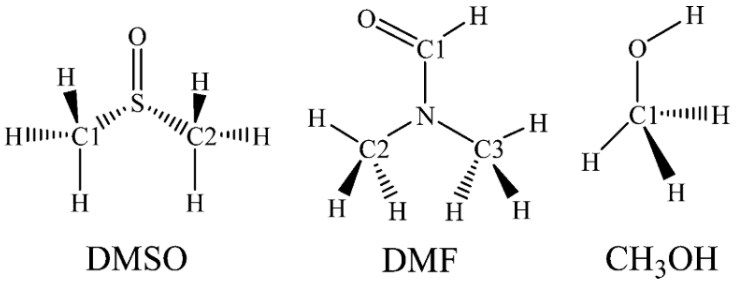

Figure 1.12: Chemical structures of three different co-solvents. From left to right; Dimethyl sulfoxide, dimethylformamide and methanol. Credit: Zhao et al. [115]

The Kamlet-Taft (KT) parameters, given by the variables 'α' (denoting the ability to donate h-bonds), 'β' (denoting the ability to accept h-bonds) and 'π' (the polarizability) are often used to quantify the properties of a solvent or co-solvent [116, 117]. Dimethyl sulfoxide for example, has moderate h-bond accepting abilities but displays a poor tendency to donate h-bonds, with α and β values of 0.15 and 0.78 at 30 °C respectively [118]. In contrast, [C4mim][OAc] at 30 °C has α and β values of 0.49 and 1.09 respectively [119]. The marked difference in the KT parameters between solvent and co-solvent in this case mean that the DMSO does not compete with the the anion for interactions with the cellulose hydroxyl groups.

1.8 Anti-Solvents and Coagulation

As dissolution progresses, cellulose chains will become free from their positions in the crystal lattice and move outwards into the solvent. During dissolution, a cellulose rich gel is often seen to form between solvent and solute [120]. Post-dissolution, the removal of the active solvent may take place in an *anti*-solvent such as water, ethanol or acetone. Such an substance is introduced as a means of breaking the solvent-cellulose bonds formed during the dissolution process, with water especially showing a remarkable tenancy to cleave these bonds [121].

Upon sufficient removal of the solvent, new h-bonds are formed between cellulose chains- resulting in the formation of a new crystal structure commonly known as 'Cellulose II' [27, 20, 122], this process is termed 'coagulation' [123]. A diagrammatic representation of this procedure is shown in Figure 1.13, whereby solvent molecules are seen to detach from the cellulose hydroxyl groups in favour of binding to the anti-solvent water. Following from this, figure 1.14 depicts the coagulation process in an aqueous environment on a much larger scale, where cellulose chains can be seen to assemble into an ordered structure via hydrogen bonds and hydrophobic forces. Coagulated cellulose is known to be one of the most hydrophilic polymers [27] and features a two-chain unit cell [6]. Cellulose II does not readily exist naturally and can only be created via coagulation or mercerization (a swelling treatment involving sodium hydroxide). However, there are reports of a structure similar to cellulose II existing naturally within the cell walls of some specific algae [124, 125].

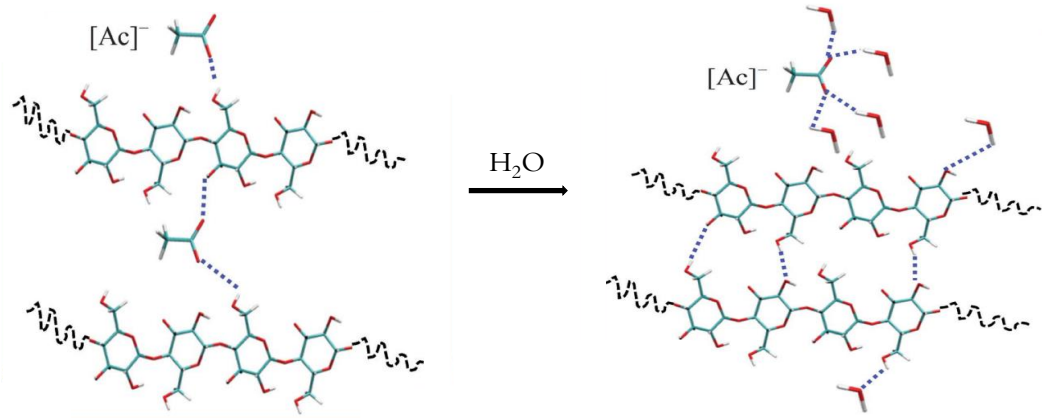

Figure 1.13: Proposed coagulation mechanism when adding water to a cellulose/ionic liquid mixture, with h-bonds shown as dashed lines. Image adapted from the work of Gupta et al. [123]

Different anti-solvents have been found to have a measurable effect on the resultant cellulose structure, with cellulose coagulated in water displaying a far

greater degree of crystallinity (43 %) to that coagulated in ethanol (21 %) [126]. It has also been reported that anti-solvents are not always able to completely remove all solvent molecules, with some residual anions (in the case of ionic liquids) found to reside within the polymer matrix for multiple years [127].

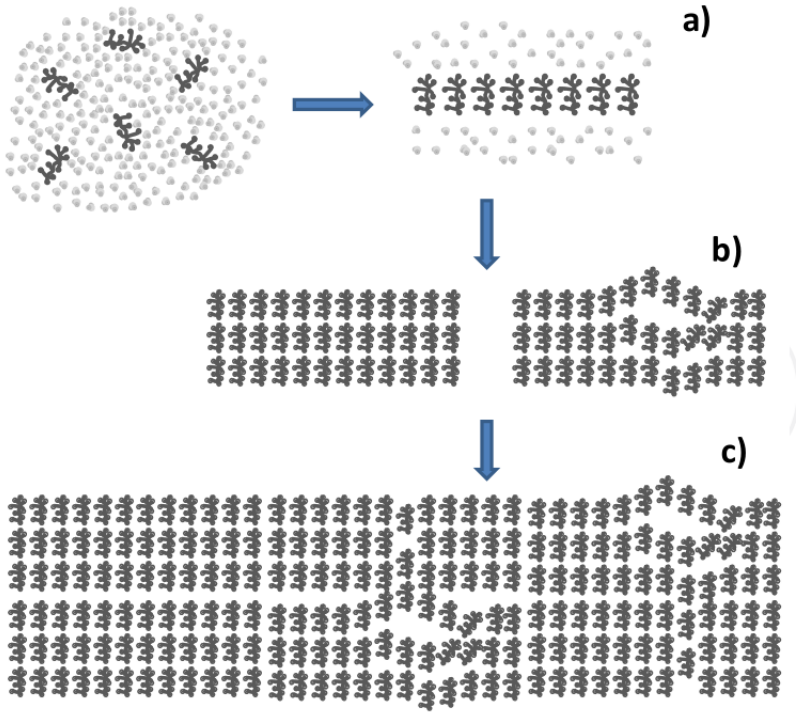

Figure 1.14: Schematic showing the process of coagulation in an aqueous environment. Black symbols represent cellulose molecules and grey dots represent water. a) Glucose molecules join together due to hydrophobic interactions into a sheet like structure. b) Sheets stack via hydrogen bonds, with some domains being less ordered than others. c) Resulting coagulated material featuring a mixture of crystalline and amorphous cellulose. Credit: Yamane et al. [128]

1.9 Composites

It would be remiss to conclude this introduction without first contextualising the work presented in this thesis within the field of composite science. A composite material is comprised of two (or more) components, each exhibiting different properties- be those mechanical, textural, thermal, electrical etc. A good composite will combine it's base materials in such a way that it will outperform the sum of it's parts, as often seen in the mechanical capabilities of the product [129, 130]. Examples of composite materials range from ancient clay mud bricks infused with straw, to modern day reinforced concrete and carbon fibre. Composite materials also exist naturally- wood, for example, is comprised of strong and rigid cellulose fibres embedded within a network of lignin.

Two key structural phases are identified in composite science, the 'reinforcing' phase and the 'matrix' phase. The reinforcement is often comprised of a material exhibiting a high level of resistance to deformation and (often unilateral) strength. Some common examples of reinforcing phases are nanofibers, glass particles and carbon nanotubes [131, 132, 133]. The reinforcement, however, is often poorly held together and can be weak and brittle along any axis not aligned with the molecular orientation of its constituent molecules/fibres. To counter this issue, a 'matrix' phase is introduced. This component is far more mailable than the reinforcing phase, trading strength for ductility. The reinforcing phase is embedded within the matrix such that the resulting material is strong and rigid, yet also able to absorb stress. The matrix phase can be composed of a wide range of materials- with polymer, ceramic and metal complexes being among the most frequently used [134, 135]. The vast combination of possible reinforcements, matrix phases and production methods results in a very high level of tailorability for a given composite.

Within classical composite materials such as reinforced concrete, the individual components remain distinct and separate in the final structure. Contemporary composites however, are seen to assemble the two phases into a far more intricate structure- whereby the reinforcement can take the form of mono-filaments, short fibres or even particles- as shown in figure 1.15.

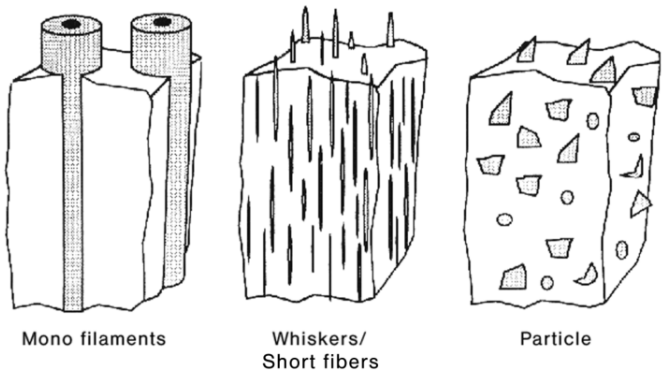

Figure 1.15: Schematics of three typical composite architectures, featuring mono filaments, whiskers/short fibres and particles as the reinforcing phase. Credit: Kainer et al. [136]

Some of the most commonly used composite materials today (such as carbon fibre) feature a synthetic polymeric matrix. Though boasting impressive strength to weight ratios, these composites are often non-biodegradable. For this reason, a fraction of the composite industry is moving towards the use of more 'eco-friendly' materials. This trend began as early as the 1970's, with natural fibres such as jute, flax, sisal and hemp being among the most frequently used [137, 138, 139]. Broadly speaking, a 'green' composite is a material manufactured entirely by renewables, or by a mixture of natural and synthetic products [140].

Recently, a new class of composites, termed 'mono'-composites has emerged- in which the reinforcement and matrix phases are comprised of a chemically identical substance. In the case of the cellulose mono-composite, the reinforcing phase is comprised primarily of the cellulose I crystal, with amorphous cellulose and cellulose II making up the matrix [141]. The formation of such a material requires the raw cellulose fibres be partially dissolved, with the dissolved fraction forming the matrix upon coagulation, see Figure 1.16. A similar technique has been utilised in the creation of traditional, oil based composites since 1992 and is known as 'hot compaction' [142]. Benefits of using cellulose include its natural abundance (with an estimated annual biosphere production of 90 x 10^9 metric

tonnes [102]), impressive mechanical properties and high level of biodegradability [143].

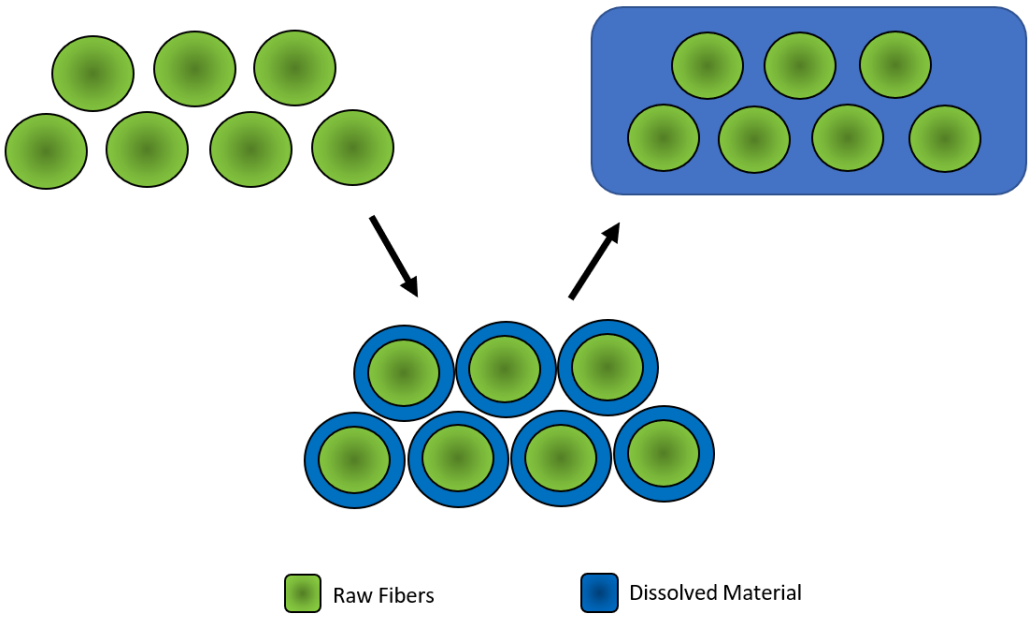

Figure 1.16: Depiction of the 'partial dissolution' process used when creating mono-composites from natural fibres.

These new 'green mono-composites' have already seen impressive early results [137, 30]. With ease of fabrication, wide spread availability, low cost and structural control- natural polymeric composites are already beginning to replace some traditional metals and plastics [144].

Despite this promising area of research however, the dissolution mechanics of cellulose are still not fully understood. The dissolution time and temperature are clearly important variables in the composite preparation procedure, though only a handful of papers have been published on their effects [145, 146, 147, 148]. The work presented in this thesis aims to provide a better understanding of the role of such variables when dissolving cellulose yarn in an ionic liquid.

1.10 Motivation

Estimates suggest that a minimum of 250,000 tonnes of of plastic waste is currently adrift in our oceans [149, 150, 151]. Barnes et al. estimate that the longevity of plastic is on the order of hundreds to thousands of years, but is likely to be much longer in deep sea and non-surface polar environments [152]. Plastic debris can cause a number of issues; it acts as a choking hazard for wildlife, introduces non-native chemicals into a system an degrades into micro-plastics which may be subsequently ingested. For this reason, it is vital to engineer new materials to replace conventional plastics. One such class of new materials mentioned previously are the 'green composites', which have gained much attention in recent years [46, 153, 154, 155]. Such composites could replace many plastics whilst maintaining a high level of biodegradability [156, 157, 158]. Such plastic-substitutes may become commonplace if the dissolution process used during manufacturing is sufficiently understood.

Another waste stream currently causing environmental and financial problems across the globe is that of the textile industry. Globally, 92 million tonnes of textile waste were disposed of during 2015 alone, with an estimated increase of 62 % by the year 2030 [159]. As most of this waste is cellulose based (i.e flax, cotton etc.), it stands to reason that these fabrics could be instead utilized as base materials for recyclable, green composites.

Taking dissolution as the method of processing has many advantages. As the remainder of the thesis will show; the dissolution of cellulose-based yarn in an ionic liquid proves to be a reliable and highly tailorable process- with variables such as temperature/co-solvent concentration/water content all acting to modify the dissolution rate in predictable and controllable manner. Dissolution using non-derivatizing solvents also ensures the molecular integrity of the solute and many solvents are potentially recyclable [160]. A greater level of understanding with regards to the dissolution mechanisms will undoubtedly lead to the usage of cheaper/more effective solvents in the future.

1.11 Thesis Overview

The structure for the remainder of this thesis is as follows:

Chapter 2 lays out the core experimental methods used- focusing on the preparation of the yarn and the dissolution procedure itself. Here, the frequently used 'optical' method of analysis is also explained, as is the Arrhenius equation and the details surrounding the creation of a cellulose film.

Chapter 3 then looks in detail at the dissolution of flax yarns via the use of three key experimental techniques: optical microscopy, X-ray diffraction and mechanical testing- with each technique allowing for a distinct means of studying the dissolution behaviour. Time-temperature superposition is observed in the system and Arrhenius plots are generated. The activation energy of dissolution resulting from each experimental technique is subsequently documented.

Chapter 4 builds on the insights from the previous chapter, only now with the inclusion the co-solvent dimethyl sulfoxide at various concentrations. The effects of the co-solvent are quantified in terms of its ability to a) modify the dissolution rate of yarns and b) effect the activation energy of dissolution.

Next, Chapter 5 documents the influence of small amounts of H_2O when added to the solvent bath. The interactions between water, cellulose and ionic liquid are discussed, before optical micrographs reveal the effects of water on the dissolution mechanics. Again, the rate of dissolution is compared to that of 'dry' ionic liquid and activation energies are documented for each water concentration used.

Finally, chapter 6 summaries the core findings and discusses possible future directions for the research.

Chapter 2

Experimental Methods

2.1 Dissolution Procedure

The solvent used was 1-ethyl-3-Methylimidazolium acetate ([C2mim][OAc]) purchased from Sigma-Aldrich with a purity of >95%, as its ability to dissolve cellulose is well documented [161, 162, 163]. A continuous yarn of flax with a diameter of 0.5 mm was purchased from Airedale Yarns and used as the source of cellulose. Prior to dissolution, the yarn was wound around a polytetrafluoroethylene (PTFE) picture frame of dimensions 5 cm × 5 cm. The frame was then submerged in a bath of ionic liquid (IL) which was in turn placed in a Leybold Sogevac vacuum oven capable of pumping down to 0.5 mbar - see Figure 2.1. The [C2mim][OAc] was preheated to the desired temperature prior to dissolution. A vacuum was maintained during the dissolution process in order to prevent the absorption of atmospheric moisture by the IL, as multiple studies have shown substantial interactions between water and [C2mim][OAc] [164]. Upon exiting the oven, the yarns, still wound around the frame, were placed in a running water bath for 24 hours at room temperature. Finally, once removed from the water bath, yarns were left to dry at room temperature for a further 24 hours before being cut free from the frame.

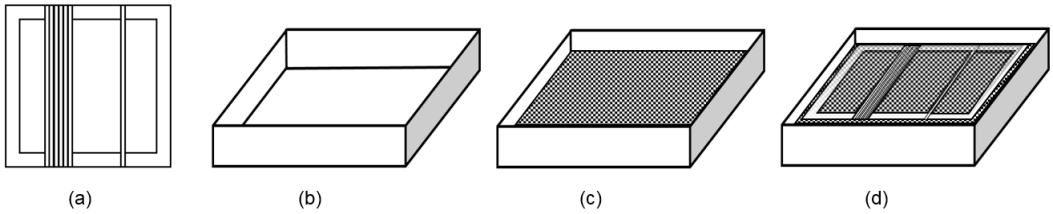

Figure 2.1: Dissolution procedure. (a) Depiction of the frame used to wind individual pieces of yarn around (b) Dish used to hold the IL/frame/cellulose (c) Dish full of IL (d) Dish full of IL with frame and cellulose submerged.

2.2 Cellulose Film Creation

In order to study amorphous cellulose, a cellulose film was prepared via the following method: A 50 cm length of raw flax yarn was cut into pieces, each measuring approximately 3 mm. These pieces were then added to a beaker of ionic liquid at a weight ratio of 95 % IL to 5 % flax. The IL/flax solution was then heated on a hot plate at 90 °C for 72 hours while being stirred with a magnetic bead. Upon removal from the beaker, the dissolved cellulose/IL solution was transferred to a flat, circular dish and spread out evenly across the surface. Next, the dish was placed in a humid atmosphere such that atmospheric water may act to slowly regenerate the cellulose. (The conventional water bath method of coagulation would result in the destruction of the fragile film at this stage.) After 3 days, the cellulose solution, now semi-congealed into a thin, malleable film, was placed into a running water bath for a further 24 hours to remove any excess IL. Once washed, the resultant film was then dried in a hot press for 1 hour at 80 °C with contact pressure applied - resulting in a film consisting of only amorphous cellulose and the cellulose II crystal.

2.3 Dealing With Uncertainties

Throughout this thesis, the following equation is commonly used as a method of determining the standard error of the mean of a given set of measurements;

$$SE = \frac{\sigma}{\sqrt{N}} \tag{2.1}$$

Where SE is the standard error, sigma is the standard deviation of the population and N is the size of the set (number of measurements taken).

Unless otherwise stated, the error bars appearing within subsequent plots are determined via equation 2.1 where N = 3.

2.4 Optical Microscopy

In order to image the cross sections of yarns, an Olympus BH2 microscope was used in conjunction with a CCD (charge-coupled device) camera. Yarns were embedded vertically within an epoxy resin mould prior to photographing, which was subsequently ground down and polished - allowing for a clear cross sectional image to be captured.

Two distinct regions are seen in the optical micrographs of processed yarns, as shown in Figure 2.2. The inner core can be seen to be surrounded by a notably different outer layer. Detailed analysis into the origin and composition of these two layers is presented in section 3. However, it may be assumed at this point that the outer layer is comprised of cellulose that has undergone the dissolution and coagulation process.

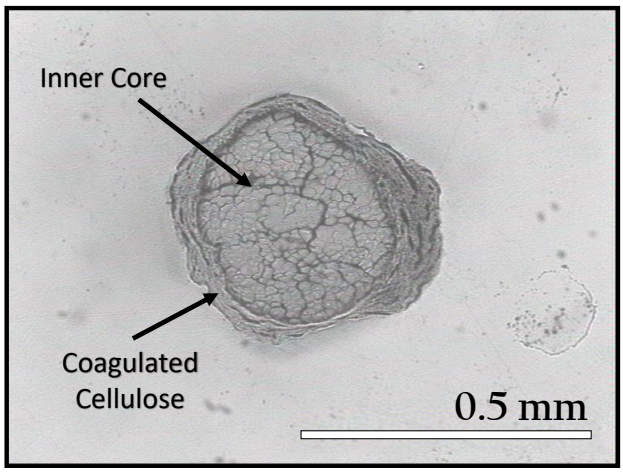

Figure 2.2: A typical optical micrograph

The area of the coagulated outer layer relative to the total cross-sectional area is referred to as the 'Coagulation Fraction' (CF) and is calculated using equation 2.2:

$$CF = \left(\frac{A_C}{A_T}\right) \tag{2.2}$$

where CF: Coagulation Fraction, A_c: Cross sectional area comprised of coagulated cellulose and A_T: Total area of the cross section.

The clear boundaries between core and coagulated material, as well as coagulated material and exterior can be established and measured. This procedure is shown in Figure 2.3, where these boundaries (shown by red lines) are traced out by eye using software (ImageJ). The error associated with the ratio between inner and outer boundaries was determined using equation 2.1, where N = 3. i.e., this ratio was measured for three distinct yarns processed under identical conditions before calculating the standard error associated with all three measurements.

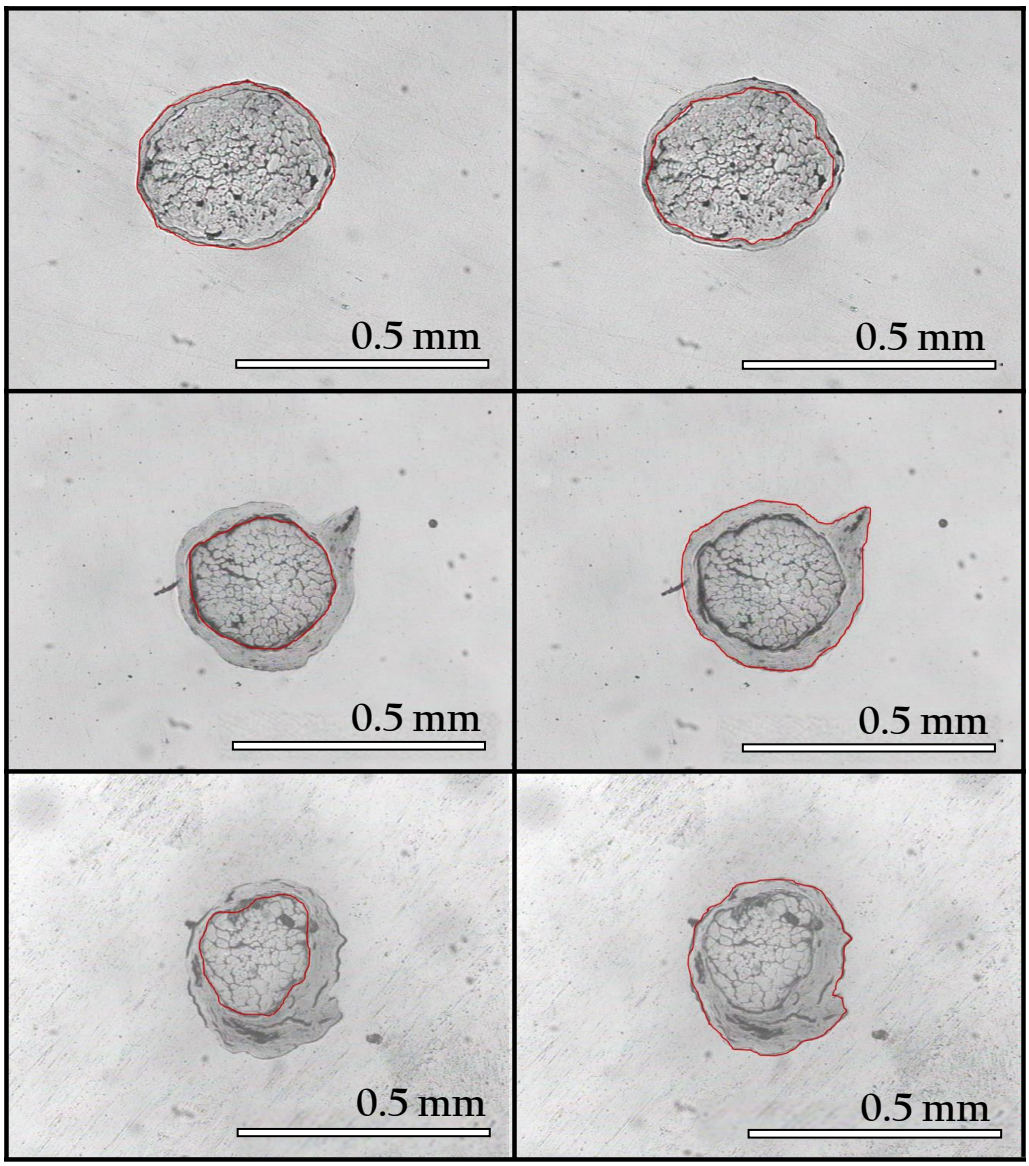

Figure 2.3: Determination of the boundaries around the coagulated layer of cellulose. The inner boundary is shown on the left and the outer on the right. Yarns shown were dissolved at 60 °C for 0.5 hours (top) 2 hours (middle) and 6 hours (bottom).

2.5 Arrhenius Analysis

Throughout this work, the Arrhenius equation is frequently used- see equation 2.3. This expression relates the rate of a reaction to the temperature at which the reaction is occurring.

$$k = Ae^{\left(\frac{-E_a}{RT}\right)} \tag{2.3}$$

Where k is the rate constant, E_a the activation energy, R the gas constant, A the pre-exponential factor (a reaction based constant) and T the temperature in kelvin.

If the rate constant (k) obeys the Arrhenius equation, then a plot of ln(k) Vs. T^{-1} will reveal a straight line with a gradient -E_a/R and intercept ln(A), as evident in equation 2.4.

$$lnk = \left(\frac{-E_a}{R}\right)\left(\frac{1}{T}\right) + lnA \tag{2.4}$$

Within the above expressions, E_a describes the minimum energy required in order for a reaction to proceed. Figure 2.4 shows how the enthalpy of a system, H, is ultimately lowered by the overcoming of an energy barrier. Since absolute values of H cannot be determined, changes in H as a system moves from one state to another become an important indicator of the feasibility of a reaction. The larger ΔH, the less likely a system is to revert back to it's original state (if physically possible). The physical nature of the activation energy in our system is not obvious, though it is thought to relate to the energy required to break apart the fundamental bonds which hold together the cellulose crystal lattice.

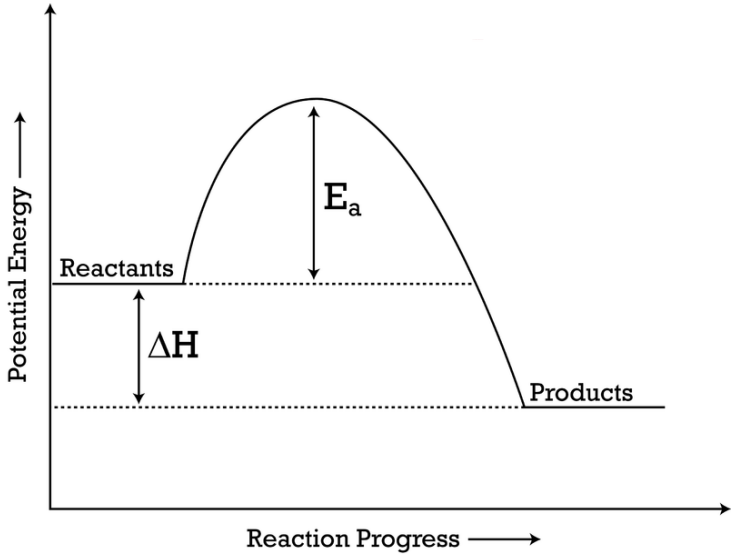

Figure 2.4: Depiction of the energy landscape for a system obeying the Arrhenius law.

The physics underlying the Arrhenius law relates to *collision theory*, which states that reaction rates depend on the number and energy of collisions between solvent and reactant, as well as the collision angle. The Boltzmann distribution is invoked as a means of determining how many molecules exist at a given temperature with kinetic energy sufficient to overcome an energetic barrier. This concept is expressed graphically in Figure 2.5.

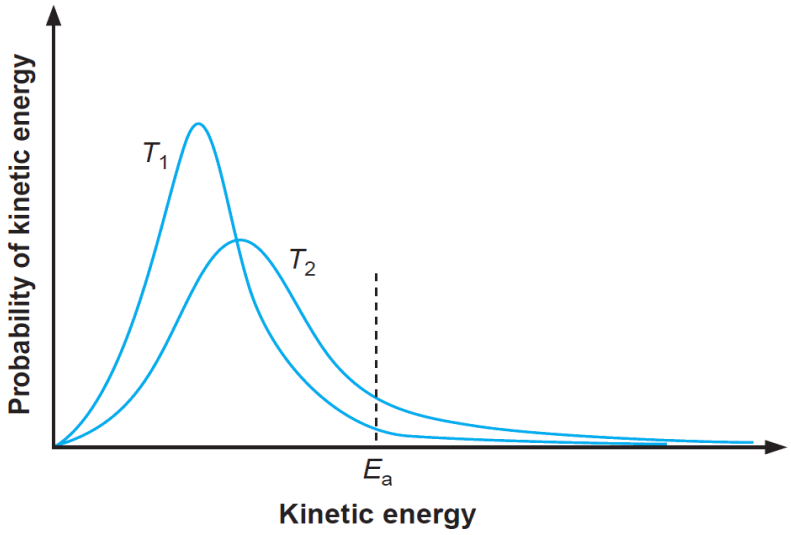

Figure 2.5: Boltzmann distribution describing the kinetic energy of molecules within a solution. As the temperature is increased ($T_1 < \mathrm{T} < T_2$), a corresponding increase in the number of molecules with energy $>\mathrm{E}_a$ is evident.

Chapter 3

Dissolution Of Flax Yarn In [C2mim][OAc]

3.1 Introduction

Of the range of potential variables within a solvating system, temperature is undoubtedly one of the most important [165, 166]. Changes in temperature can modify the time scales of a reaction and act to provide molecules with sufficient energy to overcome thermodynamic barriers. Arrhenius analysis (mentioned in section 2.5) allows for the temperature of a system to be related to reaction rates in order to reveal associated activation energies. Cellulose does not exhibit any 1^{st} order thermodynamic phase transitions within the temperature window used in this chapter (30 °C to 70 °C). Therefore, temperature variance predominantly effects the solvent. Much work has been reported on the use of temperature as a means of modifying certain properties of ionic liquids- such as their densities, viscosities and diffusion rates [167, 164].

Within many areas of industry, the temperature needed to ensure the occurrence of a reaction can contribute enormously to the total cost of the process. [168] In Germany, as much as three quarters of the industrial energy demand is needed in the form of heat [169]. The cement industry, for example, requires a kiln operating temperature of 1500 °C [170] and the oil industry requires over 350 °C in order to hydro-crack heavy fuels [171]. Within the composite industry,

temperatures in excess of 2000 °C are required for production of carbon fibre [172, 173] and the paper industry requires around 170 °C in order to convert wood shavings to pulp. [174].

This heavy reliance on processing temperature in many reactions has prompted much study into the use of catalysts and energy saving mechanisms [175, 176, 177]. Such measures, however, can only be implemented once a systems underlying relation to temperature is understood. The following chapter aims to explore this underlying relation by analysing the effect of temperature on the dissolution of flax yarns when submerged in [C2mim][OAc]. Three key methods of analysis are utilised; optical microscopy, X-ray diffraction (XRD) and mechanical testing. Each technique, as outlined below, allows for a distinct means of tracking the amount of dissolution.

Method 1: Optical Microscopy

Optical microscopy provides a quick and easy method of determining the amount of dissolved yarn due to the noticeable difference between raw and coagulated material when viewed under a microscope. Others have utilised a similar technique when quantifying cellulose dissolution and found similarly accurate and reproducible results [178].

Method 2: X-ray Diffraction

The cellulose XRD pattern (as to be explored in depth in later sections) is very well documented for both the cellulose I (CI) and cellulose II (CII) polymorphs [179, 180]. Such a pattern allows for the determination of crystal species within samples and more importantly, the ratio between them. This information is pertinent to our studies, as the various types of crystals can be used to determine the degree of dissolution. As mentioned in section 1.1, it is known that the cellulose I lattice will not reform post dissolution, as it is more favourable from an energetic perspective to re-form as cellulose II [181]. This information allows for a direct measure of dissolution by looking at the relative rising and falling of various crystal peaks on an '2θ' scan.

Method 3: Mechanical Testing

The partially dissolved yarns used within this work can be viewed as all-cellulose composites- as they consist of a strong, fibrous 'reinforcing phase' (central core) in conjunction with a more malleable, weaker 'matrix phase' (consisting of coagulated cellulose). Within the domain of composite science, the ratio of matrix to reinforcing material plays a crucial role in the determination of a composites resulting mechanical properties. A composite with too low a matrix fraction will lack resistance to deformation, whereas a composite with too much matrix material be overly-ductile and weak. The strong and complex network of bonds within cellulose results in outstanding mechanical properties. Bamboo fibres, for example, exhibit a tensile strength and modulus of 1600 Mpa and 26 GPa respectively [182]. This strength to weight ratio rivals even steel and makes cellulose a great candidate for use in modern 'green-composite' materials [183].

The mechanical strength and modulus play an important role in our analysis, as they can be used to determine how much of the central core of the yarn has been dissolved. The tensile modulus of a composite is related to the ratio between its constituent components and thus the modulus of yarns can be used as a measure of how much raw material has been converted into coagulated cellulose. Likewise, the mechanical strength is directly proportional to the amount of strength-providing raw material. By tracking how the strength varies, a corresponding trend in dissolved fraction is revealed.

3.2 Methods

3.2.1 Dissolution Procedure

The dissolution procedure outlined in section 2.1 is used throughout this chapter.

3.2.2 Optical Microscopy

Optical micrographs were attained and analysed using the techniques described in section 2.4.

3.2.3 X-Ray Diffraction (Digital)

Wide Angle XRD was used in order to determine the crystalline structure of both raw and processed flax yarns. The apparatus used was a 'DRONEK 4-AXES, Huber Diffractionstechnik GmbH & Co. KG, Germany', able to count the number of X-rays per unit time at a range of 2θ angles. Scans were conducted in transmission mode from 5 ° to 30 ° in 2θ, with a resolution of 0.2 °. An operating voltage and current of 40 kV and 30 mA were used respectively. Extra crystallographic information can be attained at two theta values above 30 °, however, studies have shown that scanning from 5 ° to 30 ° in 2θ is ample in the determination of crystal species within cellulose [184].

When scanning yarns (both raw and processed) multiple strands of yarn were placed parallel to each other in order to form an array. This was necessary as the diameter of each individual yarn measured roughly only a quarter the diameter of the X-ray beam. With multiple strands of yarn forming an array, the beam was able to pass through more material and thus result in a stronger signal. An optical micrograph of such a processed array can be seen in Figure 3.1.

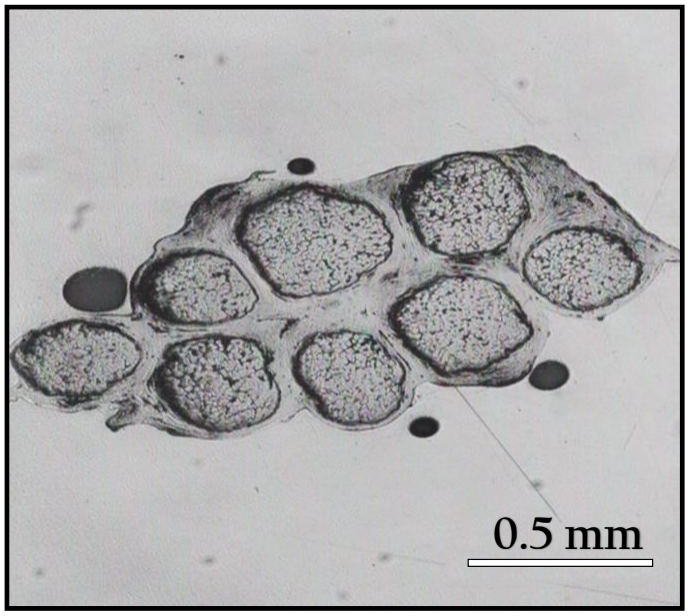

Figure 3.1: Optical micrograph of an array used for XRD studies. Eight individual yarn cross sections can be seen embedded in a coagulated matrix.

To begin analysis, the amorphous peak (well documented to exist around 18 ° in 2θ ([185, 186]) was fit using a single peak to the data from an unprocessed yarn. This peak was allowed to move ± 2 ° either side of 18 °, whereas the width and amplitude were left unconstrained as to allow for optimum fitting. This broad peak can be seen overlaid on the raw data in Figure 3.2 and in isolation in Figure 3.3.

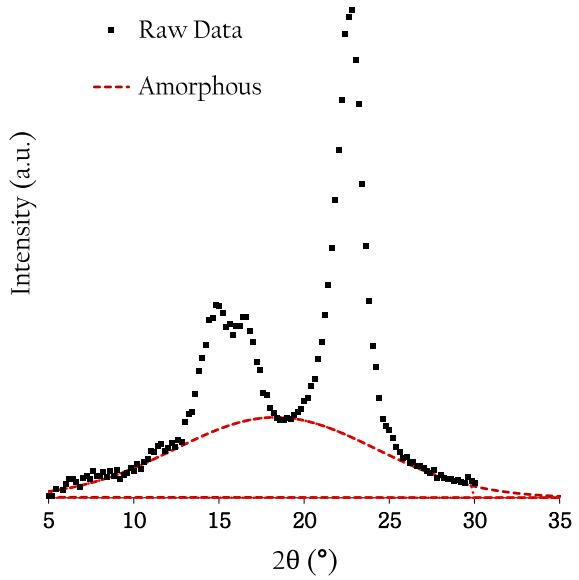

Figure 3.2: The broad amorphous peak shown in red, with data points corresponding to a scan of the raw yarn.

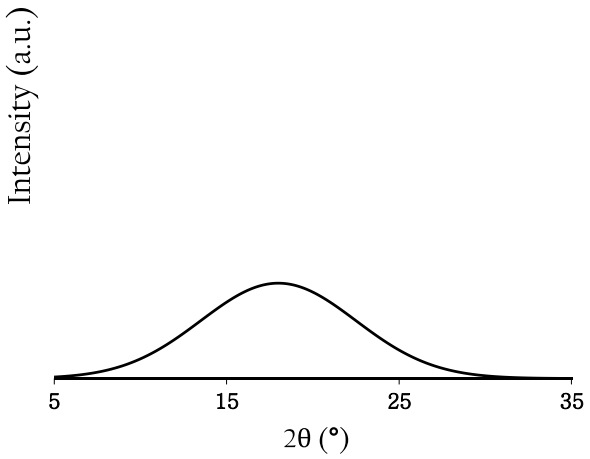

Figure 3.3: The broad amorphous peak in isolation.

In order to next identify the cellulose I peaks, the well documented Bragg locations in 2θ were used as a rough guide. Figure 3.4 shows the cellulose I peaks being placed onto raw yarn data, alongside the aforementioned amorphous peak. These cellulose I peaks, shown in green, were allowed to move $\pm$ 2 $^\circ$ either side of their commonly stated values in the literature [187, 188, 189, 190], while the peak heights were left unconstrained. The peak widths were forced to be equal to each other, as the broadening of peaks is due to instrumental effects such as diffraction around the slit/air scattering etc.- all of which are assumed to be independent of 2θ angle. This width common to all CI peaks however, was also left unconstrained.

With these constraints in place, a sum of least squares approach was used to mathematically determine the optimum fitting of CI peaks. The resultant fitting information (location of peaks in 2θ, peak width, relative amplitudes) was then averaged upon repeating the process three times for three distinct raw yarn scans. The resultant cellulose I 'theory peaks' can be seen in figure 3.5. These peaks were found to exist at 14.8 $^\circ$, 16.7 $^\circ$ and 22.7 $^\circ$ in 2θ and correspond to Bragg reflections of the (1,1,0), (1,$\overline{1}$,0) and (2,0,0) planes respectively [191].

Table 3.1 summarises the crystallographic information pertaining to the cellulose I peaks. The 'relative height' column of this table describes the hight of each cellulose I peak relative to the height of the peak with the smallest 2θ value.

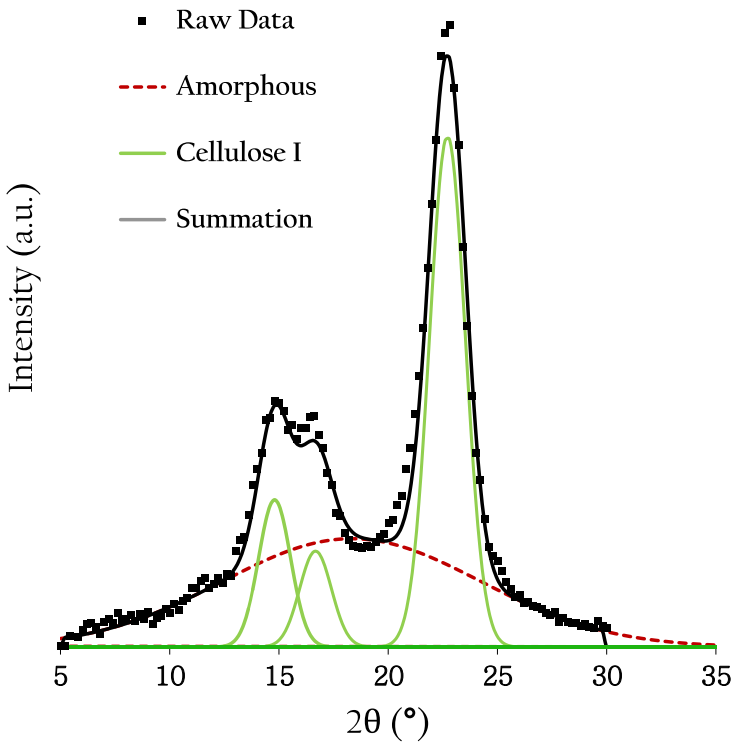

Figure 3.4: The optimum fitting of CI peaks (green) in conjunction with the amorphous peak (red). The solid black line represents the summation of all peaks (including the amorphous peak).

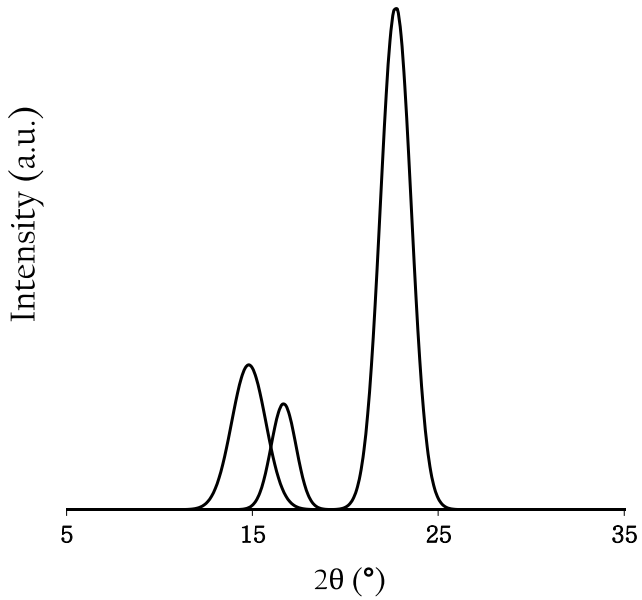

Figure 3.5: Theoretical cellulose I peaks.

Table 3.1: Cellulose I Bragg Peak Information.

Peak Location (°)	Relative Height	Miller Index
14.8	1	1,1,0
16.7	0.7	1,$\bar{1}$,0
22.7	3.5	2,0,0

The cellulose II peak locations, heights and widths were determined in a similar manner: data from a partially dissolved yarn (featuring amorphous cellulose, cellulose I and cellulose II) was fit using the aforementioned amorphous and cellulose I peaks. Alongside these peaks however, the software was now also given

three extra peaks- corresponding to the cellulose II reflections. As with the cellulose I peak fitting method mentioned previously, the cellulose II peaks were also allowed to move ± 2 ° either side of their documented values found in the literature, while the peak heights were left unconstrained. Again, the widths of peaks were constrained to be equal to each other. The fitting software was then tasked with fitting the data using a combination of amorphous, cellulose I and cellulose II peaks in superposition. Upon fitting (see Figure 3.6), the cellulose II peak information could be extracted and isolated. The isolated cellulose II theory peaks, shown in Figure 3.7 are again determined from the average location/height/width of these peaks across three distinct scans. In this case, the peak locations determined at positions 12.4 °, 20.2 ° and 21.8 ° in 2θ correspond to Bragg reflections of the $(1,\bar{1},0)$, (1,1,0) and (0,2,0) planes respectively [192]. Table 3.2 summarises the crystallographic information pertaining to the cellulose II peaks.

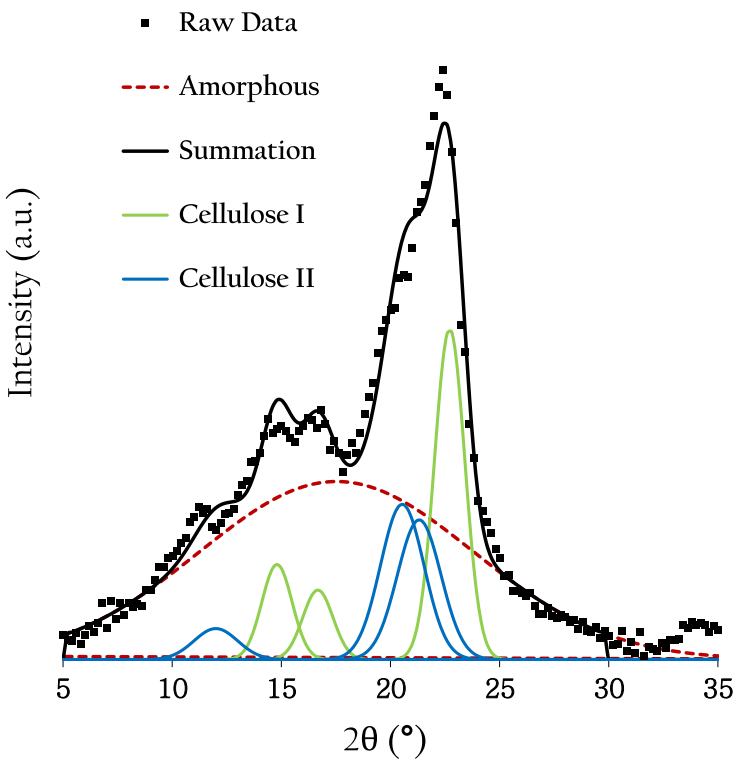

Figure 3.6: The optimum fitting of CII peaks (blue) in conjunction with the cellulose I peaks (green) and amorphous peak (dashed red) The solid black line represents the summation of all peaks (including the amorphous peak).

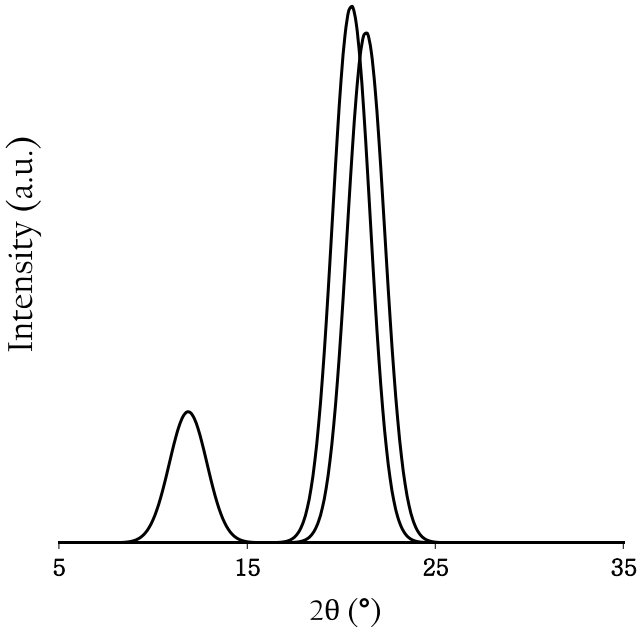

Figure 3.7: Experimentally derived cellulose II peaks.

Table 3.2: Cellulose II Bragg Peak Information.

Peak Location (°)	Relative Height	Miller Index
11.9	1	1,$\bar{1}$,0
20.5	4.1	1,1,0
21.3	3.9	0,2,0

The cellulose I and II peak locations as determined by experimentation were found to be in close agreement with the published work of others: see image 3.8 for comparison.

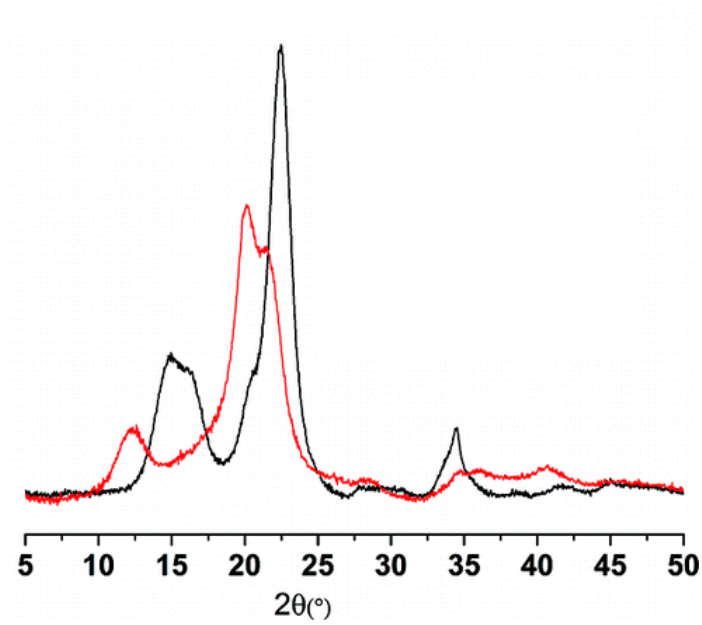

Figure 3.8: Documented X-ray diffractograms for cellulose I (black) and cellulose II (red), both include amorphous cellulose. Credit: Liu et al. [193]

In order to analyse the XRD data, scans were de-convoluted into their constituent amorphous, cellulose I and cellulose II peaks (seen prior in figures 3.3, 3.5 and 3.7 respectively). Using these sets of peaks in superposition, the sum of squares between theory and data was computationally minimised. Figure 3.9 displays all experimentally derived peaks together, as well as their collective summation.

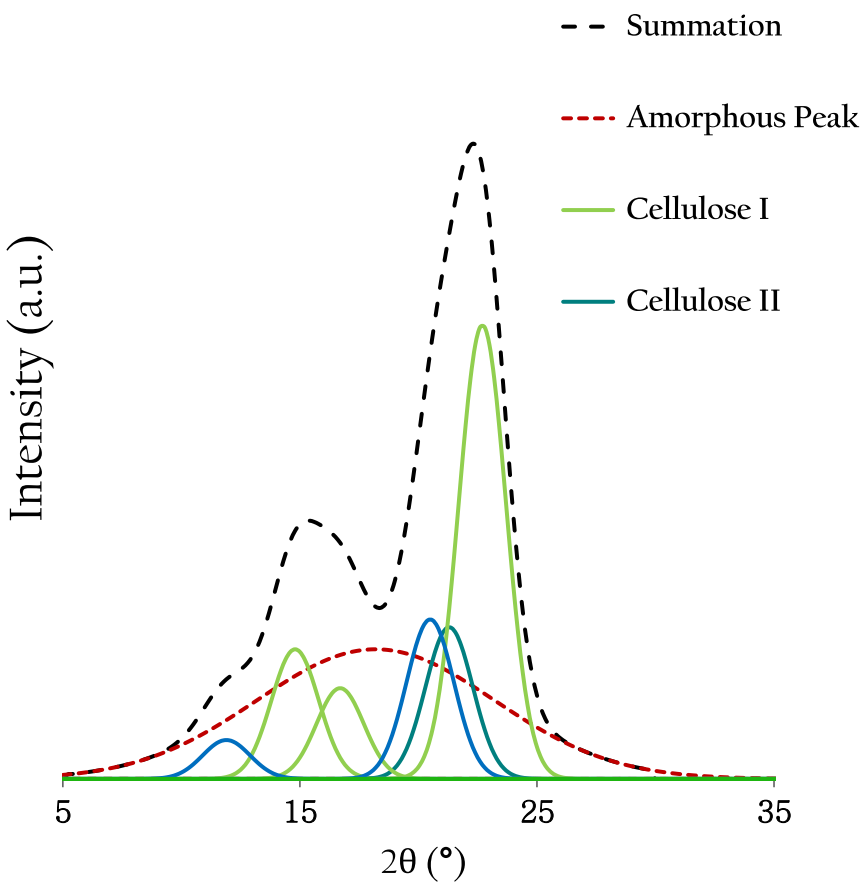

Figure 3.9: The summation (black dashed line) of the amorphous (red dashed line), cellulose I (solid green line) and cellulose II (solid blue line) contributions.

Equation 3.1 is used to determine the fraction of cellulose crystal species X from a 2θ scan;

$$C_X = \left(\frac{A_X}{A_T}\right) \tag{3.1}$$

Where C_X is the fraction of Cellulose species X (either cellulose I or II), A_X is the area of the peaks corresponding to species X and A_T is the total area of all peaks, including the amorphous peak. Only the relative areas of crystal peaks are considered, as these give the fractions of amorphous material/cellulose I/cellulose II. When a value of C_X is stated, this refers to the average C_X as taken from three distinct scans- each attained using a different array processed under identical conditions.

The above expression describes how the amount of Cellulose I (CI) may be calculated from a digital XRD scan. If we assume the CI is homogeneously dispersed throughout the raw yarn, then the CI reduction also describes the total amount of yarn dissolved (as CI does not reform post-dissolution). As the coagulated material is created from this dissolved fraction of the yarn, a simple relationship between CF and dissolved CI is presented in equation 3.2. Using this equation, the digital XRD data may be expressed in terms of the CF- making it easily comparable to the other methods of analysis used in this chapter.

$$CF \ = 1 - \frac{Remaining\ CI}{Initial\ CI} \tag{3.2}$$

Though the results attained via XRD are shown to be in close agreement with other published studies on the makeup of flax [194, 195], some data may exhibit discrepancies caused by the following:

Firstly, it should be noted that the XRD data presented in this chapter may be affected by the yarn-based architecture, which ensures preferential alignment of the polymer crystals along the vertical axis of the yarn. As a result, any

diffraction peaks not appearing on an equatorial diffraction scan will be ignored. In the case of Cellulose I, the (0, 1, 2) Bragg peak does not appear equatorially, thus is absent on a 2θ scan. This peak is small when compared to all other Cellulose I peaks however, so its absence has little effect on the results. In order to negate this issue in future studies, a powdered sample may be used instead.

There will also be discrepancies due to the helical nature of the yarn. Due to the twist about the vertical axis, the 'front' of the yarn will feature sub-fibres at a small angle from the vertical (the twist angle 'θ') and the 'back' of the yarn will display sub-fibres with a similar deviation in the opposite direction. See figure 3.10 for clarification. This twisting will result in two similar XRD signals, mirroring each other at plus and minus the twist angle. As the twist angle (on the order of 7 °) is small compared to the circumferential width of the diffraction peaks ($\sim$ 40 °), this is not a major issue for our analysis. As any peak modification due to the twist angle will be common to all scans, this does not affect the results (which merely use the area under the equatorial peaks as a marker of dissolution).

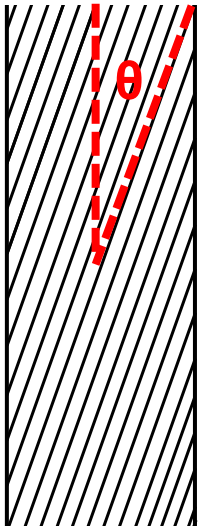

Figure 3.10: Basic schematic of the flax-based yarn, displaying sub-fibres at a twist angle 'θ' from the vertical.

3.2.4 X-Ray Diffraction (Analogue)

X-ray sensitive photographic films were used to capture two-dimensional diffraction patterns. The films were placed 5 cm from samples and were left exposed for a period of two hours at an operating voltage of 40 kV and a current of 30 mA. See figure 3.11 for a basic schematic of apparatus.

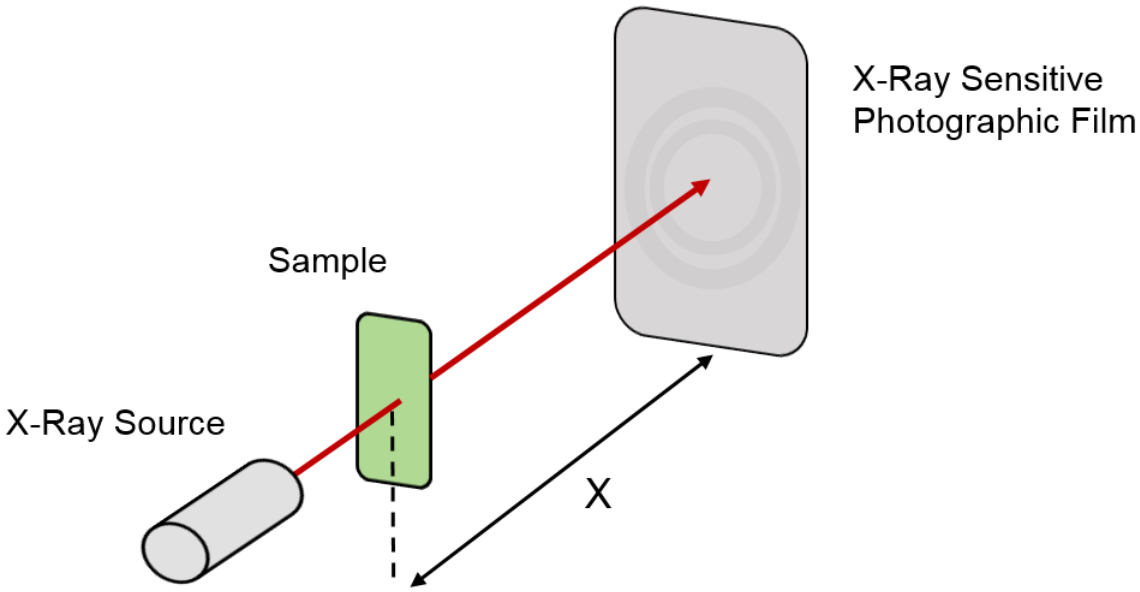

Figure 3.11: Schematic of the XRD set up used when capturing a two-dimensional diffraction pattern, with X = 5 cm.

3.2.5 Mechanical Testing

An Instron 5565 Universal Test Machine was used to determine the mechanical properties of flax yarn. Samples were securely fixed at both ends and pulled apart at a rate of 10 mm/min. A Messphysik Video Extensometer was used to accurately track the strain rate via the use of two identifiable stickers, as shown in Figure 3.12. Data is presented in the form of 'Stress-Strain' plots, from which the tensile strength (maximum amount of stress), modulus (the gradient of the the initial linear section of the curve) and the relative extension at breaking point are determined.

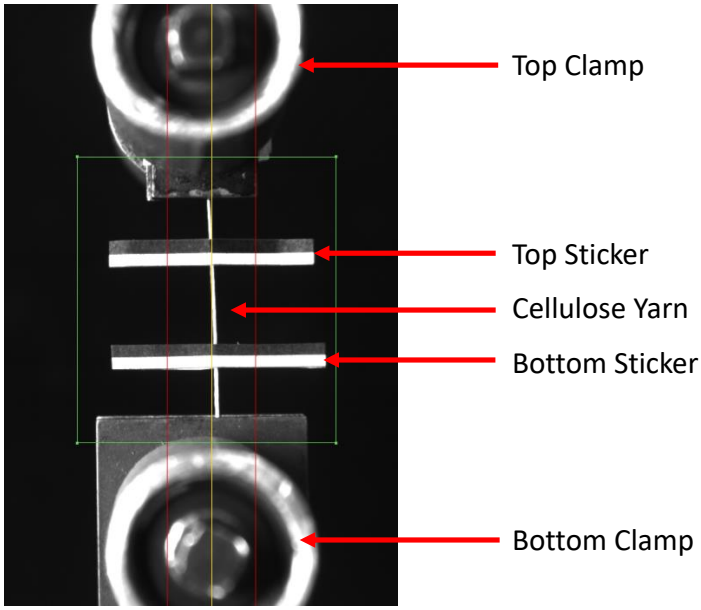

Figure 3.12: Photograph showing a sample ready to test. The horizontal stickers are automatically tracked by the camera and allow for precise measurements of the strain rate.

In order to transform the measured force into a stress, the cross-sectional area of yarn was needed. Three distinct methods were used to calculate this area- the 'density method', the use of a micrometer and optical microscopy.

The first method involves the density of cellulose, which has been extensively recorded [196, 197, 198]. Measurements of the yarn mass were used in conjunction with this known density in order to calculate the cross-sectional area.

The use of a micrometer made for quick and simple cross sectional measurements. However, care had to be taken as to not compress the fibre during the measuring process.

The optical microscope method involved the embedding of yarns vertically within an epoxy resin mould before polishing down and photographing. Using the known scale of the image, an area was calculated by sketching around the perimeter of the fibre by eye. An example of this sketching procedure has been shown prior- refer to Figure 2.3. Others have independently verified the efficacy of this measurement technique [199].

Table 3.3 summarises the results from each technique when measuring the cross-sectional area of the raw yarn. A good level of agreement is seen between the different approaches, with the smallest area resulting from the optical approach and the largest from the micrometer. As the density method was quick and simple to preform, giving rise to a cross-sectional area closest to the average of all three methods - this method was chosen to be the default measurement technique.

Table 3.3: Cross sectional area of the raw yarn as a function of measurement technique.

Measurement Method	Cross Sectional Area (mm^2)	Error in Area (mm^2)
Density Method	0.118	0.009
Micrometer	0.125	0.004
Optical Microscope	0.100	0.005

3.3 Results and Discussion

3.3.1 Optical Microscopy

Optical microscopy, previously elaborated on in section 2.4 is used to attain images of both the raw and partially dissolved yarns. The average raw yarn diameter, calculated using the area determined via optical microscopic measurements in conjunction with software, (ImageJ) was found to be 0.43 mm. Figures 3.14 and 3.15 reveal how the raw yarns are comprised of many smaller individual fibrous

bundles, packed tightly together. As can be seen from the cross sections of partially dissolved yarns in Figures 3.16, 3.17 and 3.18, this tight packing does not allow the IL to penetrate all the way through to the core of the yarn. Rather, the boundary between the dissolved and undissolved fractions moves inwards with time. It is seen that the structure of the centrally undissolved portion of yarns is visually identical to that of the raw yarn.

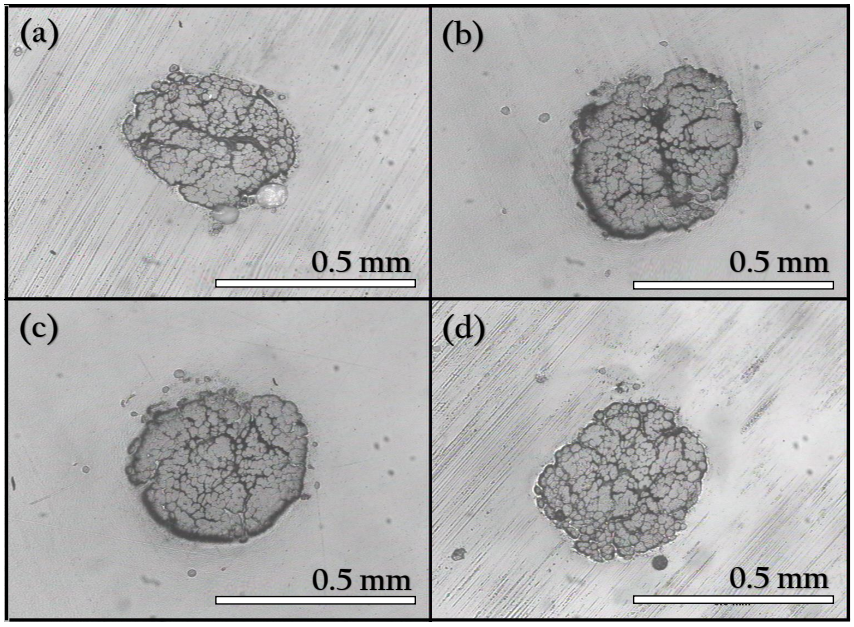

Figure 3.13: Cross sectional images of multiple raw yarns.

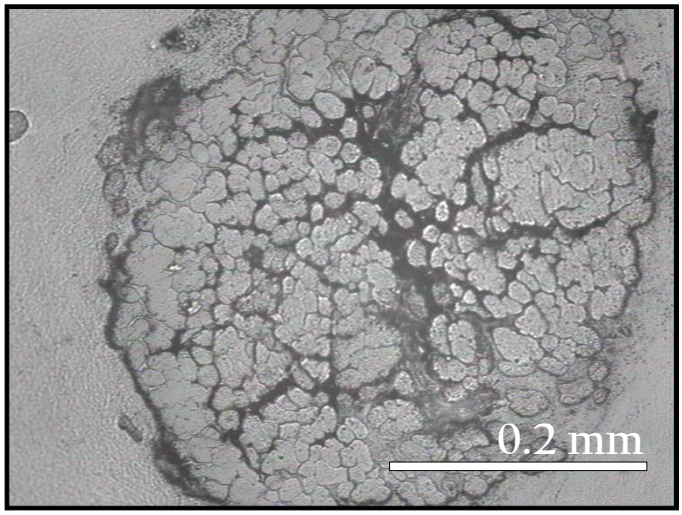

Figure 3.14: A raw yarn viewed at 20 times magnification.

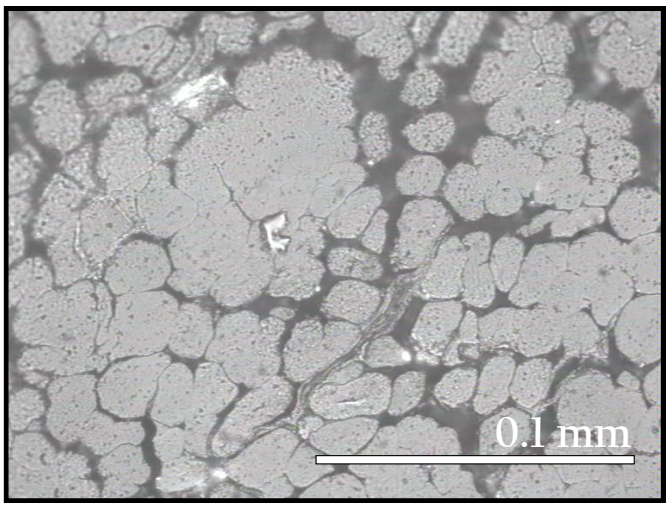

Figure 3.15: A raw yarn viewed at 50 times magnification.

The coagulated fraction (CF) is seen to increase in size as a function of both time and dissolution temperature in Figures 3.16 and 3.17. First, the coagulated material forms quickly and roughly symmetrically around the inner core, before slowing at longer times. This slowing is thought to be partially due to the outer coagulated layer acting as a protective barrier between the raw cellulose and ionic liquid, decelerating the dissolution process. The appearance of the inner core remains largely unchanged, suggesting that the ionic liquid is acting predominantly at the surface of the yarn. Figure 3.18 provides further evidence of this by showing how the coagulated material forms a boundary which encloses the yarn. Though the majority of the coagulated material is seen to exist within this outer layer, a small amount is present inside the perimeter- as evident by the bonded sub-fibres close to the edge. The inner-most sub-fibres however, remain un-bonded; revealing how the ionic liquid has not been able to reach the inner most core.

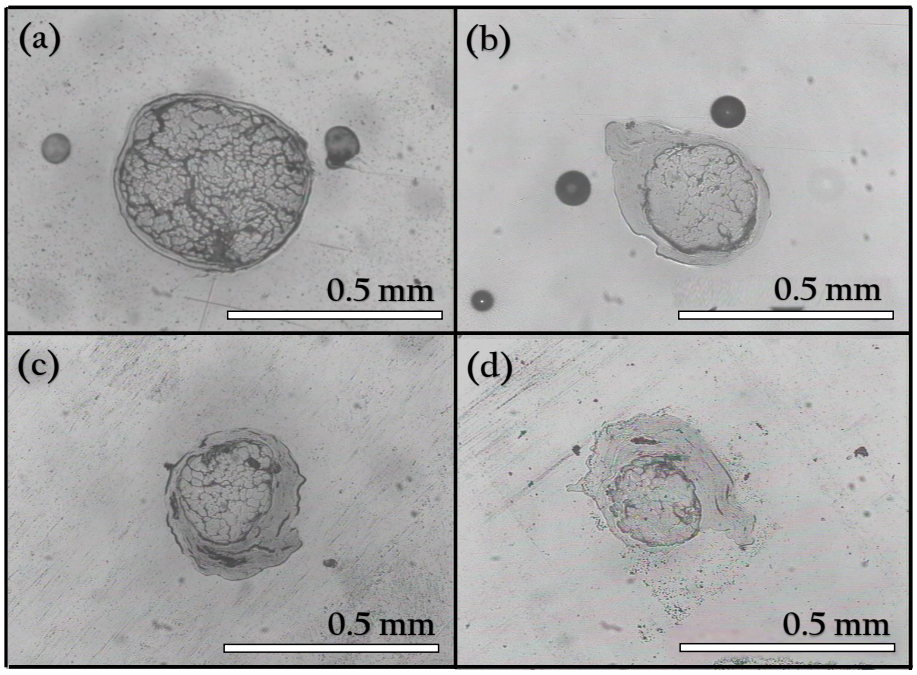

Figure 3.16: Cross sections of yarns processed at 50 °C for 2 hours (a), 4 hours (b), 6 hours (c) and 8 hours (d). The coagulated fraction can be seen to grow as a function of time.

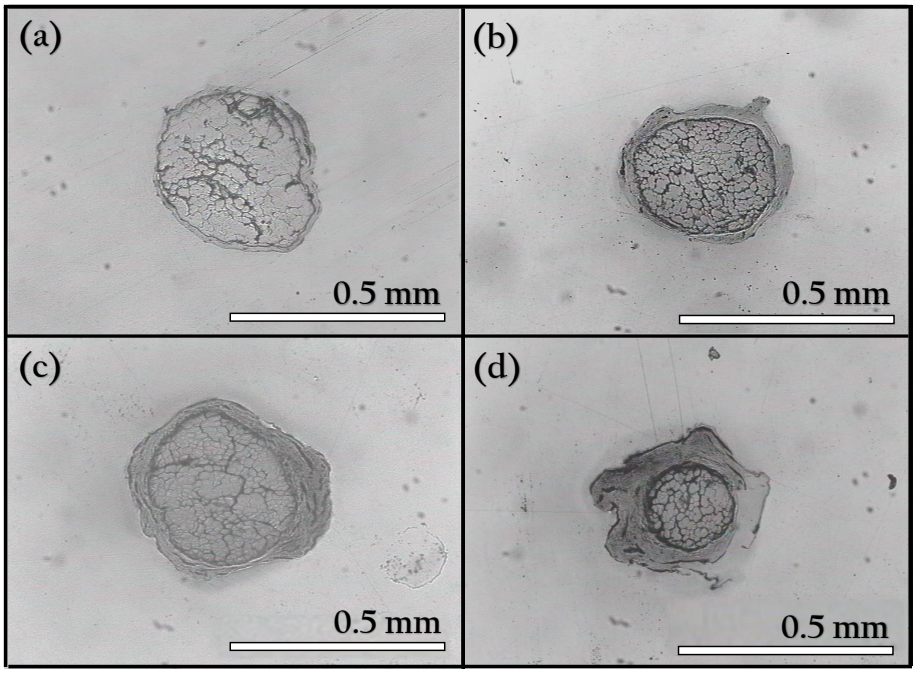

Figure 3.17: Cross sections of yarns after 2 hours at various temperatures; 30 °C (a), 40 °C (b), 50 °C (c) and 60 °C (d). The coagulated fraction can be seen to grow as a function of temperature.

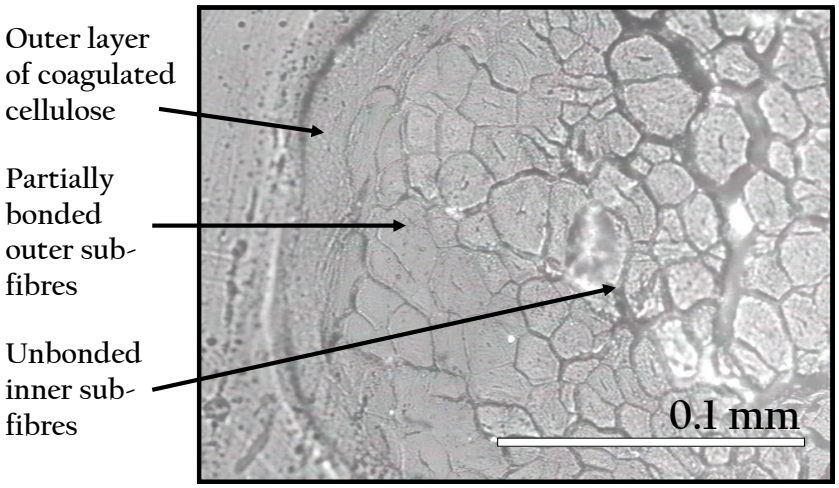

Figure 3.18: High magnification image showing the distribution of coagulated material within a yarn processed at 30 °C for 6 hours.

Shown below, Figure 3.19 presents a typical CF curve for a single dissolution temperature. On this graph, each data point represents the average CF value taken from four individual yarn cross sections (processed under identical conditions). Next, Figure 3.20 shows how the coagulation fraction (CF) grows with time at all five temperature regimes: 30 °C, 40 °C, 50 °C, 60 °C and 70 °C. The CF is never seen to rise above 0.8 due to the limitations of the measurement technique- yarns dissolved by more than 80 % do not contain enough raw material to stay attached to the dissolution frame- hence, no resultant yarn remains to embed into resin and photograph. Measurements of yarns processed at temperatures above 70 °C proved difficult to attain due to the rapid rate of dissolution at elevated temperatures. For this reason, the temperature range explored was limited to an upper value of 70 °C.

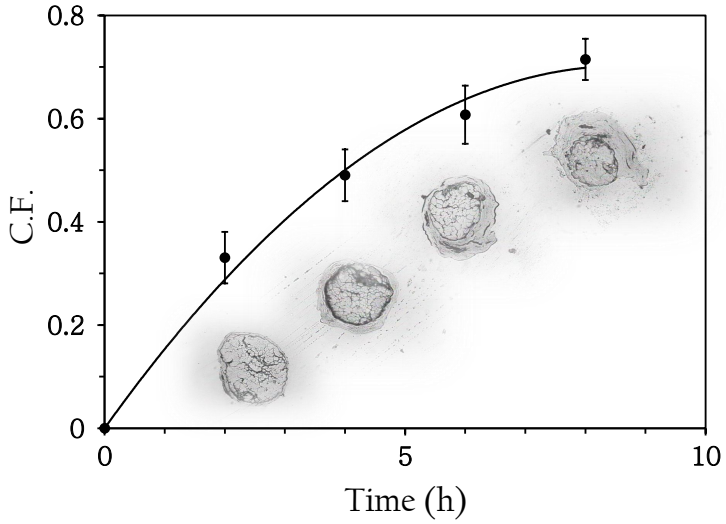

Figure 3.19: The coagulation fraction as a function of dissolution time for yarns processed at 50 °C. Images of some of the yarns photographed are shown by their corresponding data points for clarity. Polynomial fit used to guide the eye.

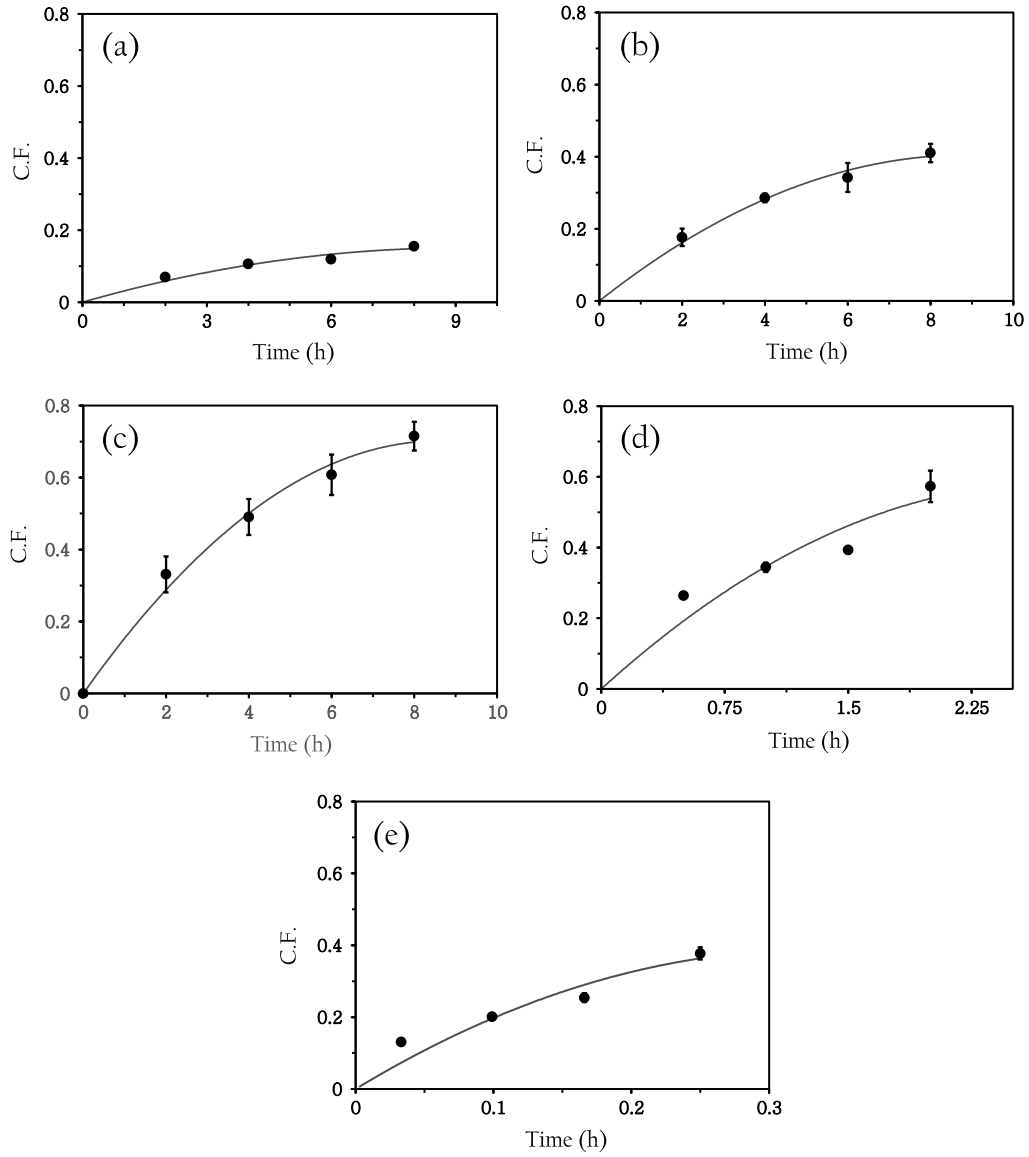

Figure 3.20: The fraction of coagulated cellulose as a function of time at various dissolution temperatures. (a): 30 °C, (b): 40 °C, (c): 50 °C, (d): 60 °C, (e): 70 °C. Polynomial fits used to guide the eye. Error bars included, though may be smaller than data points.

Figure 3.21 collects all results together to show simultaneously the effect of time and temperature on the coagulation fraction. Seeing these various data sets on the same graph suggested that the individual curves may be combined to form a single master curve- an idea which implied time/temperature equivalence in the system. Such an equivalence is often found and analysed in the study of rheology [200, 201]. To further explore this notion, the data presented in Figure 3.21 was expressed in logarithmic space. This step was performed in order to make any shifting of data sets (a subsequent step to be explained shortly) more direct. The data is seen in natural logarithmic space in Figure 3.22.

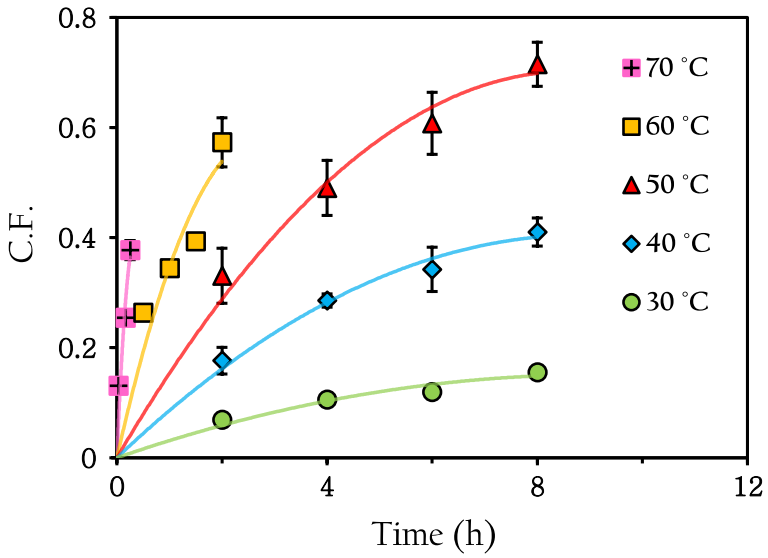

Figure 3.21: CF as a function of temperature for yarns dissolved in [C2MIM][OAc] at all dissolution temperatures. Polynomial fits used to guide the eye. Some error bars may be smaller than data points.

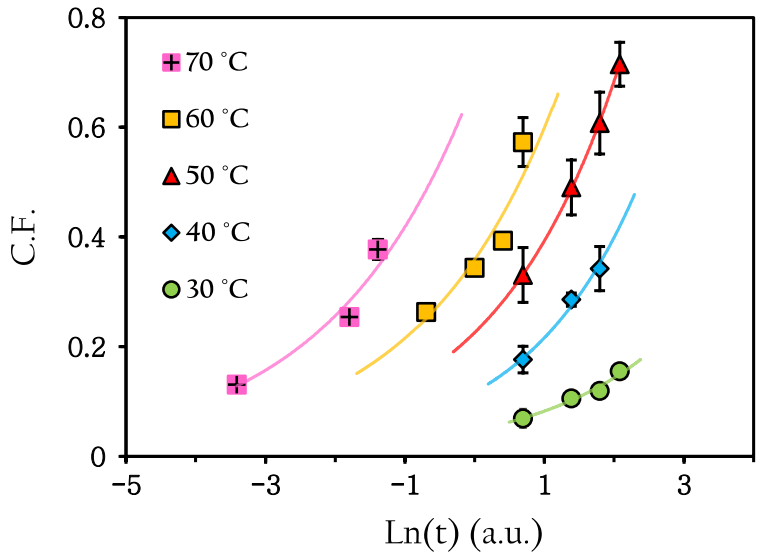

Figure 3.22: CF as a function of dissolution time for all temperature regimes as expressed in natural logarithmic space. Exponential fits used to guide the eye. Some error bars may be smaller than data points.

With the data now presented in natural logarithmic (ln) time, each data set (30 °C, 40 °C, 50 °C etc.) was independently scaled by a factor:

$$\alpha(T)$$

Where T corresponds to the temperature of dissolution. This procedure is commonplace in rheological studies when employing time-temperature-superposition (TTS). The reference temperature was chosen to be 50 °C, in the middle of our temperature range. Thus, all other data sets were scaled towards this set. The amount by which each data set was shifted in ln time is then given by:

$$ln\alpha(T)$$

The shifting of data was first performed by eye. Once a smooth and continuous curve was formed, the R^2 value between the 50 °C data and each subsequent data set was computationally minimised – ensuring the optimum shift factors were determined. Figure 3.23 documents how the data appears as the shift factors are applied in turn. Upon the shifting of all data sets, the master curve, seen in Figure 3.24 is formed.

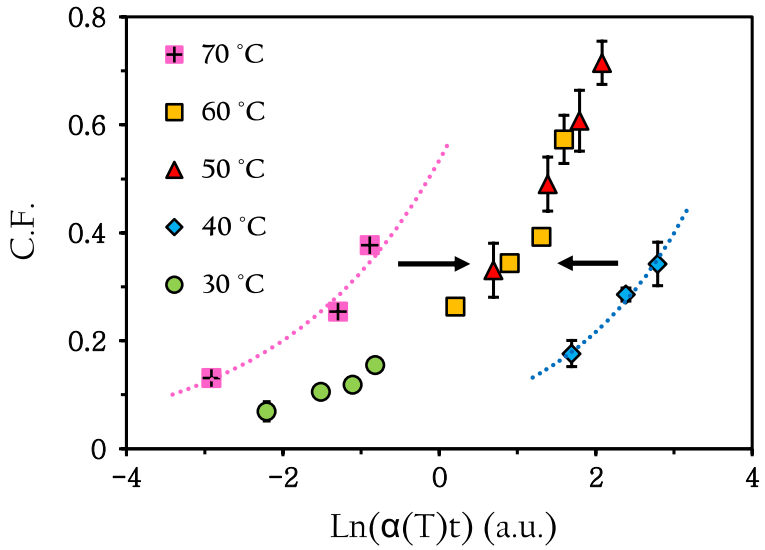

Figure 3.23: Shifting process- moving the 40 °C data (blue) and the 70 °C data (pink) towards the 50 °C data (red). Exponential fits used to guide the eye. Some error bars may be smaller than data points.

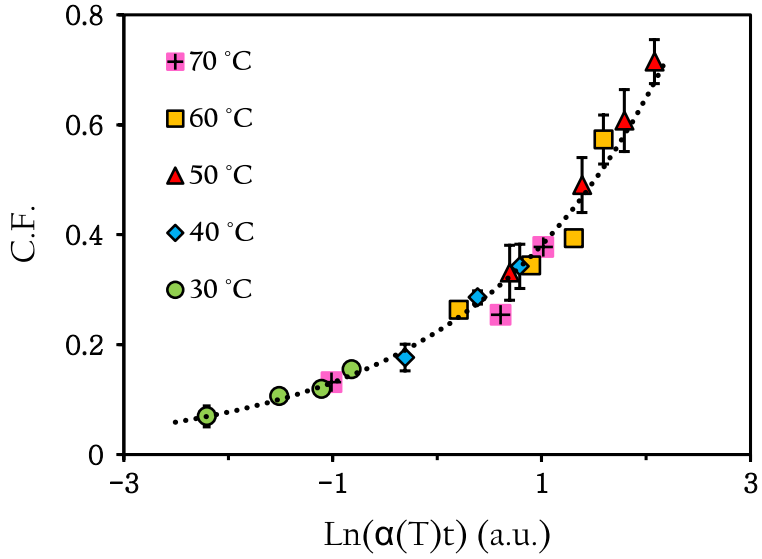

Figure 3.24: Coagulation fraction master curve including all dissolution temperatures. Exponential fit used to guide the eye. Some error bars may be smaller than data points.

The temperature dependent shift factors used to arrive at Figure 3.24 are documented in Table 3.4. A value of $ln(\alpha(T)) > 0$ implies that the dissolution rate is faster than the reference temperature (50 °C), and therefore data needs to be shifted to the right in ln time in order to overlap. Alternatively, a negative value of $ln(\alpha(T))$ represents a slower rate of dissolution. $ln(\alpha(T))$ in this case will act to pull the data to the left in the ln time domain in order for overlap with the reference to occur.

Table 3.4: Shift factors as a function of temperature

Temperature (°C)	ln(α(T))	Error in ln(α(T))
30	-2.9	0.4
40	-1	0.2
50	0	0.2
60	0.9	0.2
70	2.4	0.3

The master curve shown above provides evidence of time-temperature superposition within the system. In order to better understand the relation between time and temperature, the shift factors are plotted against the inverse of their respective temperatures in figure 3.25. The linear nature of the data seen in this figure is indicative of a system obeying the Arrhenius law, thus a corresponding activation energy (E_a) can be determined. The activation energy, calculated using the gradient of the trend line, was found to be **100 ± 10 kJ/mol**. This energy is thought to relate to the energy needed to break apart the cellulose crystal lattice at a molecular level, though the exact energy required to do this is still under discussion in the literature [202, 203, 204]. One may, however, postulate the following interpretation: As each cellulose monomer features 3 hydroxyl groups, each capable of forming an interchain h-bond with energy $\sim$ 15 kJ/mol [15, 70, 205], then this results in a total h-bond strength of $\sim$ 45 kJ/mol per monomer. If E_a corresponds to the breaking of such h-bonds, then an E_a of 100 kJ/mol may correspond to the extraction of approximately two cellulose monomers from the crystal lattice."

In relation to this activation energy; Wang et al. report a similar value for the Gibbs free energy of cellulosic dissolution (80.5 kJ/mol) when using sodium hydroxide as a solvent [145] and others have shown Arrhenius behaviour in relation to cellulosic dissolution when analysing the de-crystallisation of micro-crystalline cellulose in phosphoric acid [148]. Similarily, the enthalpy of cellulose solvation in [C2mim][OAc] has been documented by Brehm et al- whereby computer simulations have revealed an energy of 96.4 kJ/mol [206]. In other work, Brehm et

al. also quote a range of cellulose solvation enthalpies existing between 75.5 and 93.4 kJ/mol when using other ionic liquids [207].

Time temperature superposition in a similar system has also recently been documented by Chen et al, whereby they state: "The rising of temperature was found to amplify both the dissolution and swelling phenomena but did not change the observed behaviour (of cellulose fibres in [C2mim][OAc])" [178]. Within their work, they also independently document the clear boundary seen between the undissolved core and swollen exterior.

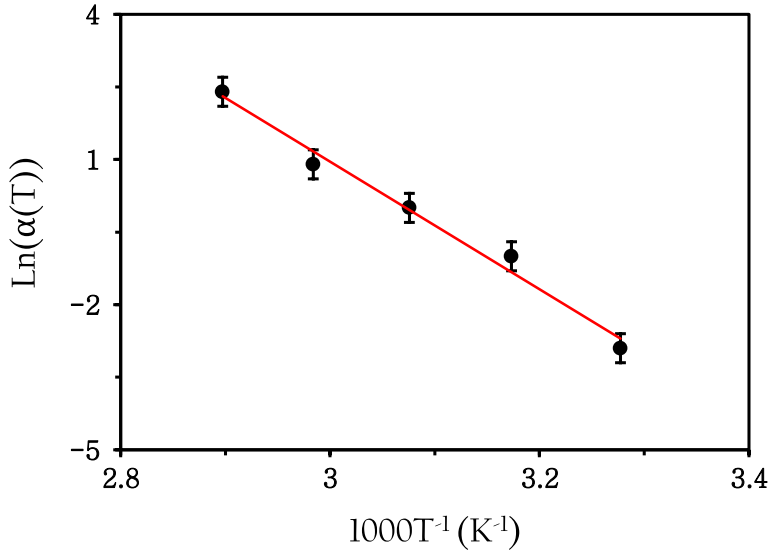

Figure 3.25: Arrhenius plot showing the relation between shift factors and temperature. The red line is a linear fit to the data.

The physical notion of an activation energy in a non-solid system is notably more complex than that of a solid system. For a rigid solid, the nature of E_a is clear- it describes the energy barrier that must be overcome for a given molecule to move from its current lattice position to a neighbouring lattice vacancy. When dealing with liquid or polymer systems however, the picture is not as clear. Molecules in such systems are constantly undergoing translational and rotational motion, resulting in ill-defined molecular positions with a lack of dis-

cernible lattice sites. Lingwood Et al. report on an appropriate evaluation of E_a in non-solid systems: claiming that E_a is related to *all* molecular interactions undergone by a molecule as it moves from its initial non-equilibrium state to its final equilibrium state. They denote the time scale on which this happens as 'τ_c' and claim that E_a is correlated with all collisions occurring during this time. This process is expressed diagrammatically in Figure 3.26. Interestingly, they claim that E_a in this case does not have a direct relationship with the diffusion coefficient, D, of the system. Rather, E_a is more closely related to the fluctuation force- which describes the average energetics of all local interactions that occur on the pre-diffusional time scale ($\approx$ 1 ps). [146]

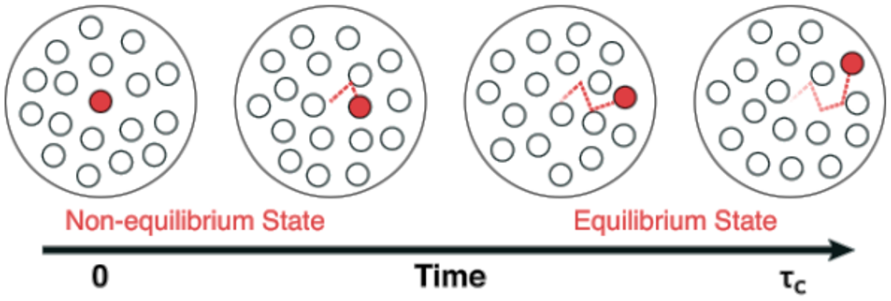

Figure 3.26: A diagrammatic representation of the path a molecule may take through a liquid/polymer system, showing events taking place during the period $0 < t < \tau_c$. At time = τ_c, the highlighted molecule no longer has a memory of its initial position and velocity. Lingwood et al. postulate that all molecular interactions during this time period contribute to E_a.

3.3.2 X-Ray Diffraction (Digital)

X-ray diffraction is used to determine the crystal species present in flax based samples. Figure 3.27 presents the XRD spectra for three distinct raw yarn arrays, scanned separately. It can be seen that the Bragg peaks appear in almost identical positions from scan to scan- showing a high degree of reproducibility and a consistent crystalline profile along our flax based yarn.

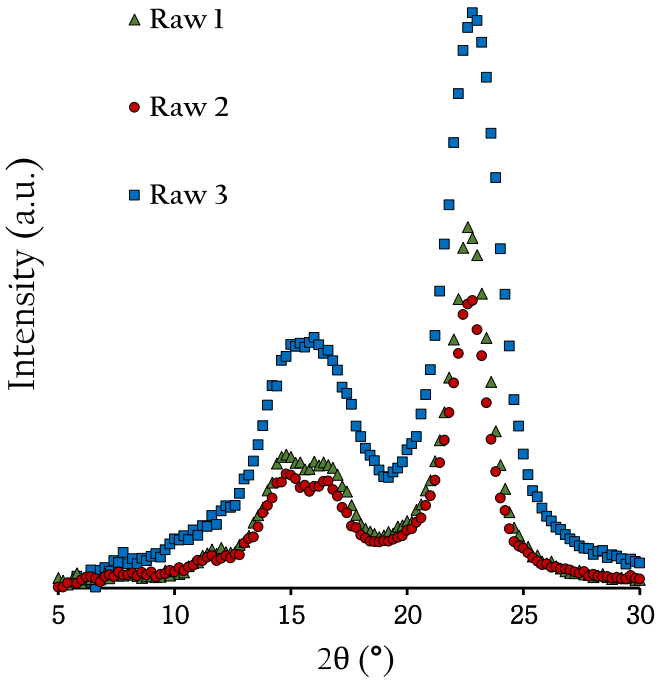

Figure 3.27: X-ray diffraction spectra for three distinct arrays comprised of raw yarn.

Figure 3.28 documents the deconvolution of a typical raw yarn scan into its constituent Bragg peaks; the peaks shown in green correspond to the cellulose I crystal lattice and were found to constitute 53.3 ± 0.5 % of the raw flax. No cellulose II is identified in the scans of raw yarns, thus- the remaining 46.7 ± 0.5 % is composed of amorphous material. Table 3.5 summarises the crystalline make-up the raw arrays.

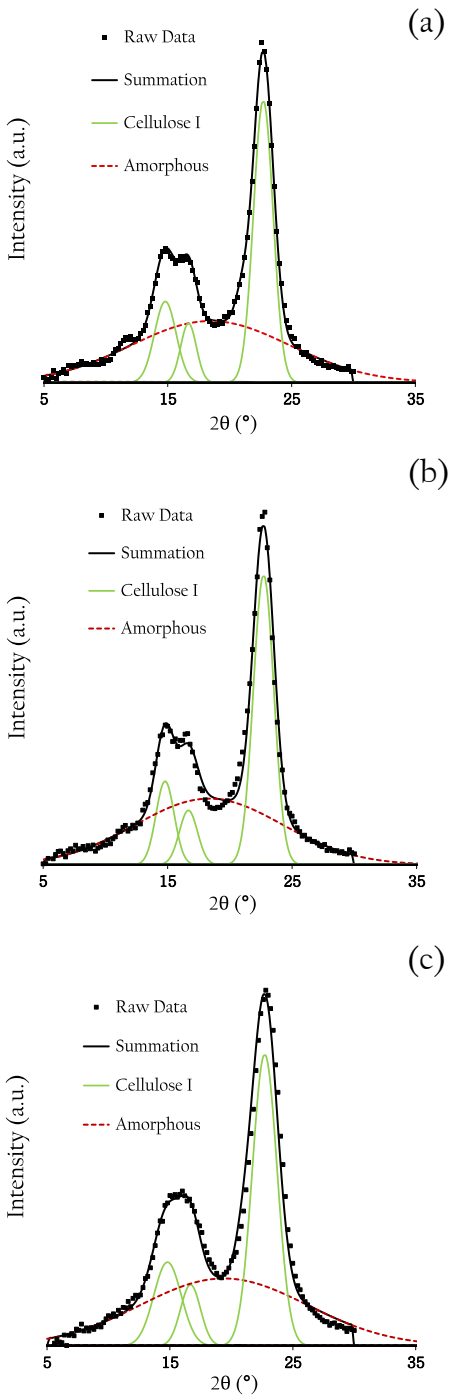

Figure 3.28: Fitting of three raw yarn scans using the deconvolution method.

Table 3.5: Structural make-up of raw yarns as analysed by digital XRD.

Array Number	CI Fraction (%)	CII Fraction (%)	Amorphous Fraction (%)
1	52	0	48
2	55	0	45
3	53	0	47

Based on the data expressed in Table 3.5, it can be concluded that the raw material used throughout this work consists predominantly of the cellulose I allomorph, with the remaining material being classified as amorphous. The ratio of cellulose I to amorphous material is in close agreement with other studies documenting the crystalline structure of flax [194, 195].

Figure 3.29 shows the XRD results for yarns dissolved at 60 °C for varying lengths of time. As dissolution progresses, the CI peaks (shown in green) are seen to decrease in size. At the same time, CII peaks (shown in blue) emerge in the data and the amorphous peak (shown in red) is also seen to increase in magnitude.

The diminishing trend in CI continues until full dissolution is achieved, at which point there is no longer any CI present. Figure 3.30 documents the XRD spectrum of such a sample. This scan confirms that the CI within the raw yarns does not transform back into CI upon coagulation, which validates our assumption that the reduction in CI can be used as a reliable marker of the total amount of dissolution.

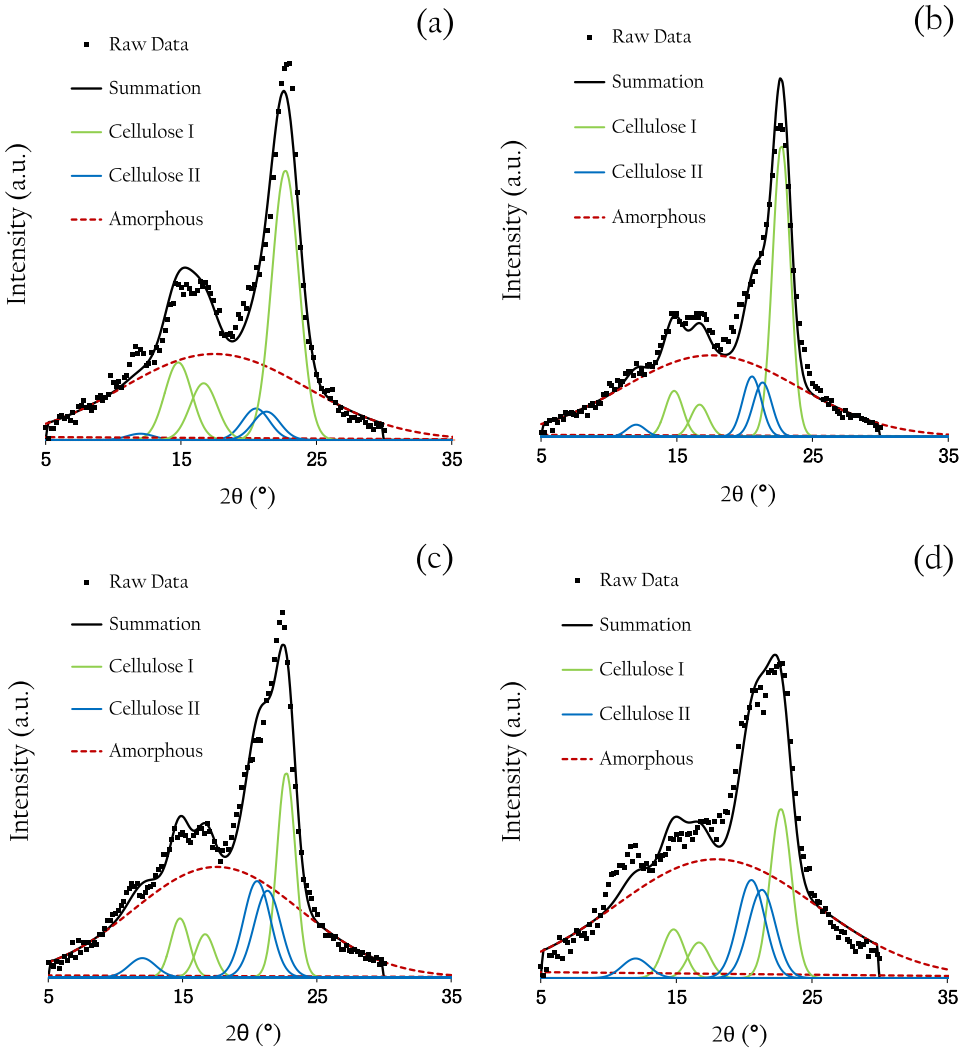

Figure 3.29: XRD data for flax arrays dissolved at 60 °C for various lengths of time: (a): 2 h, (b): 4 h, (c): 6 h, (d): 8 h.

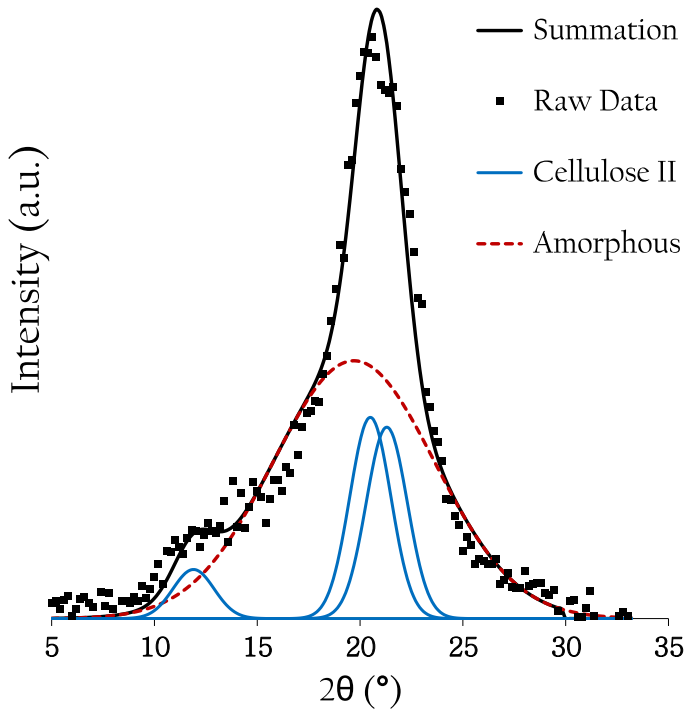

Figure 3.30: The XRD spectrum resulting from a totally dissolved and coagulated sample, showing an absence of CI.

Using equation 3.2, the XRD data may be expressed as a measure of the CF. Figure 3.31 documents the CF growth as a function of time when using a range of dissolution temperatures. As expected, the CF increases in accordance with both dissolution time and temperature.

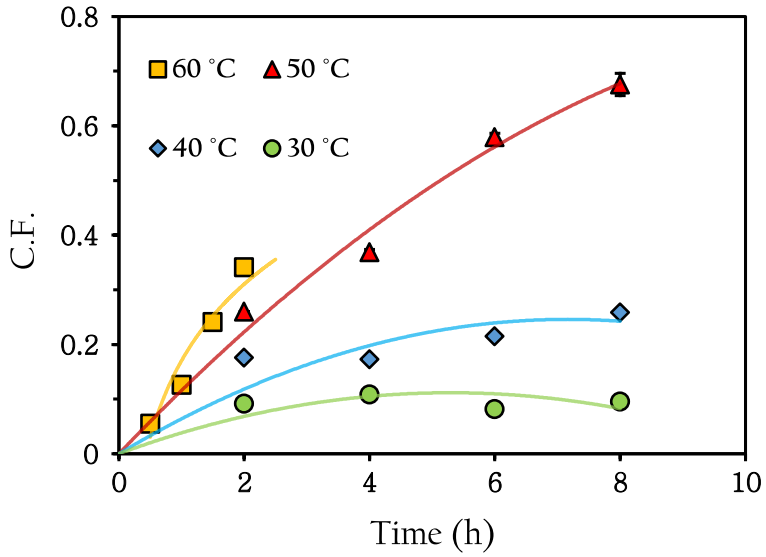

Figure 3.31: CF as a function of both dissolution time and temperature. Polynomial fits used to guide the eye. Some error bars may be smaller than data points.

From this point, the methodology outlined previously (see section 3.3.1) was used to shift the data in ln time to form a master curve. Figures 3.32, 3.33 and 3.34 document the steps taken to arrive at an Arrhenius plot. The shift factors used to generate the master curve are documented in Table 3.6.

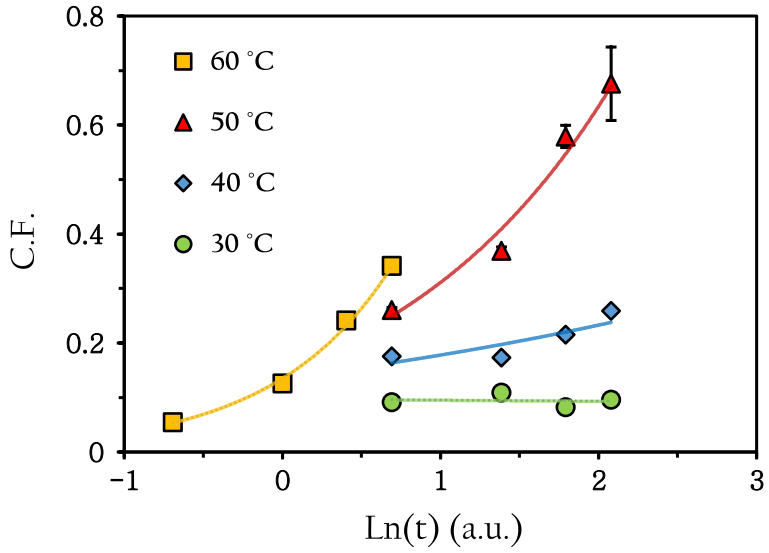

Figure 3.32: CF as a function of both dissolution time and temperature expressed in natural logarithmic space. Exponential fits used to guide the eye. Some error bars may be smaller than data points.

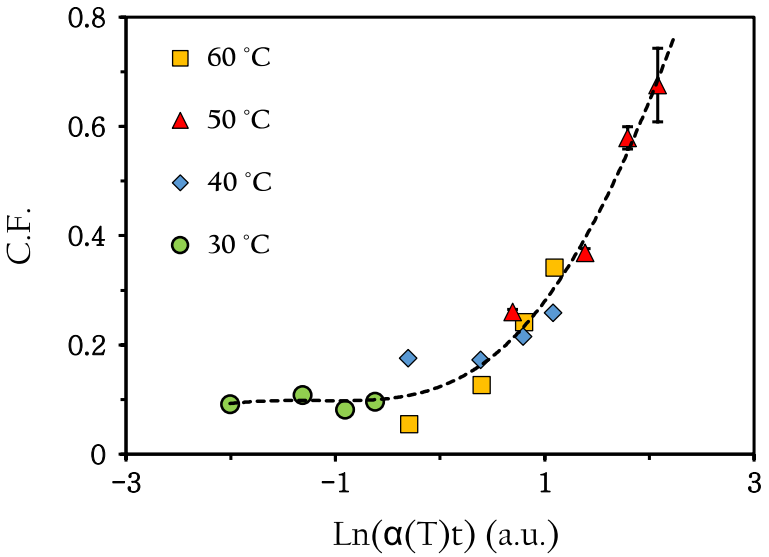

Figure 3.33: CF master curve including all dissolution temperatures. Polynomial fit used to guide the eye. Some error bars may be smaller than data points.

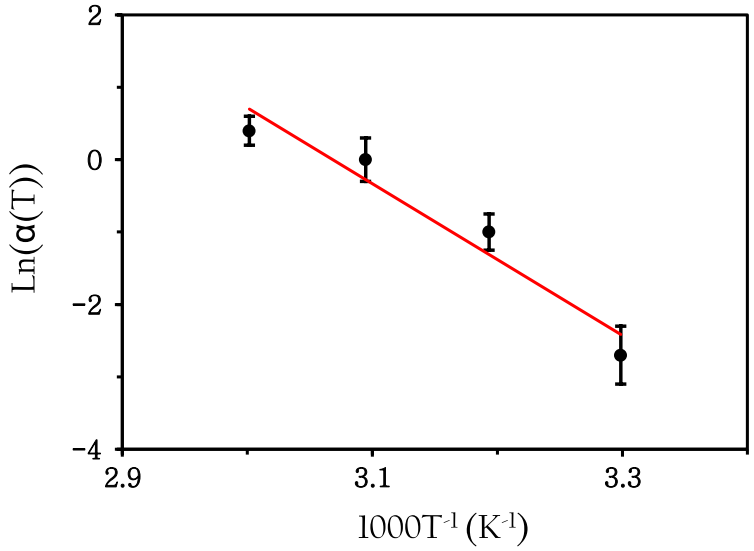

Figure 3.34: Arrhenius plot showing the relation between shift factors and temperature when using XRD to track the CF. The red line is a linear fit to the data.

Table 3.6: Shift factors as a function of temperature (XRD)

Temperature (°C)	ln(α(T))	Error in ln(α(T))
30	-2.7	0.4
40	-1	0.3
50	0	0.3
60	0.4	0.2

The linear nature of the data shown in figure 3.34 reveals an activation energy of **87 ± 16 kJ/mol**. This value is similar to that attained in the previous section when using optical microscopy, where E_a was found to be **100 ± 10 kJ/mol**. These two activation energies are believed to be describing to the same process.

The similarity between these activation energies promoted further investigation. Below, Figure **??** compares the CF as measured by optical microscopy with the CF as measured by XRD. A close agreement is seen between the two meth-

ods, though it is clear that the optical approach measures slightly more CF. The reason for identifying less CF when using XRD may be due to an assumption mentioned earlier in section 3.2.3, namely- that the cellulose I is homogeneously dispersed throughout the cross section of the yarn. If in reality the CI is more concentrated towards the centre of the yarn, then the XRD analysis (which measures the reduction in CI as a marker of the total amount of dissolution) would register only a fraction of the total dissolution. Thus, equation 3.2 would reveal a CF value lower than that of the actual CF.

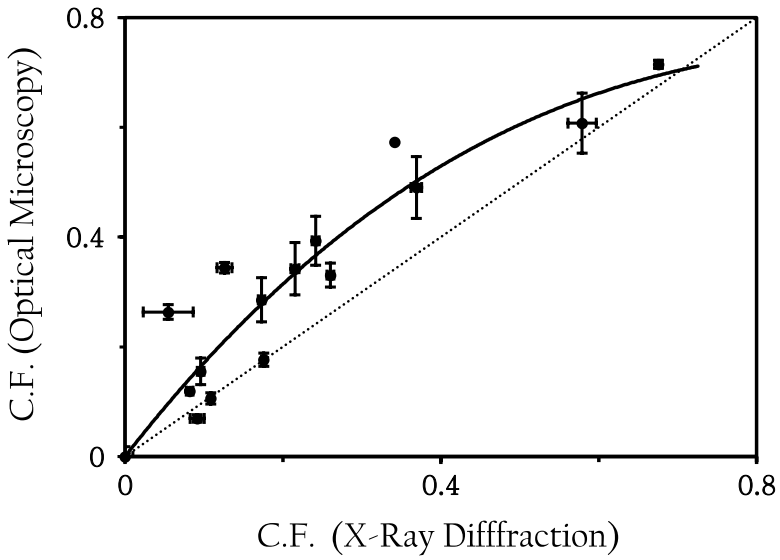

Figure 3.35: A comparison between the CF values as measured by optical microscopy and XRD. Solid black line is a polynomial fit to the data, whereas the dashed line represents a theoretical agreement between techniques. Some error bars may be smaller than data points

Another potential explanation as to why the CF value is lower when measured using XRD may be due to the differing amounts of exposed surface area between single yarns (used for optical analysis) and the array of yarns (used for XRD). These differences, highlighted in Figure 3.36 show how an individual yarn exposes more of its surface area to the solvent, hence- will undergo more dissolution per

unit time.

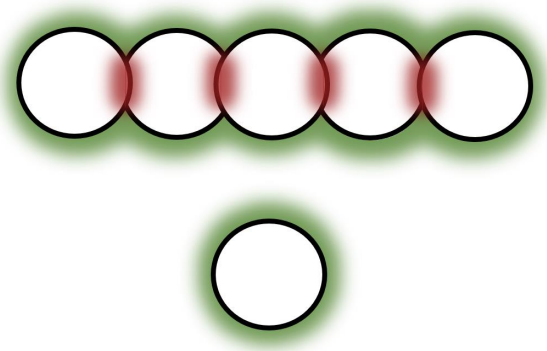

Figure 3.36: Top down depiction of an array of yarns (top) and a single yarn (bottom). The green areas represent the fraction of exposed surface area upon which the IL can act, while the red areas highlight any surface area potentially shielded from IL.

3.3.3 X-Ray Diffraction (Analogue)

The following section presents data attained using X-ray sensitive films. Figures 3.37, 3.38 and 3.39 show the diffraction patterns resulting from a raw yarn, a partially dissolved yarn and a totally dissolved yarn (a cellulose film- refer to section 2.2 for details on cellulose film preparation) respectively. The bright areas seen in these images correspond to regions of high X-ray intensity, hence-Bragg diffraction. The patterns have both horizontal and vertical symmetry, with the bright spot in the centre caused by overexposure of X-rays.

Unlike a conventional '2θ' scan, a two-dimensional scan reveals the full diffraction pattern, rather than a single line through the equator of the full pattern. A two-dimensional scan will therefore reveal other diffraction spots not necessarily visible on this line. For each X-ray film attained, two copies of the image are presented side by side. The image on the left remains unaltered for the purposes of objective viewing whereas the image on the right is overlaid with pertinent crystallographic information.

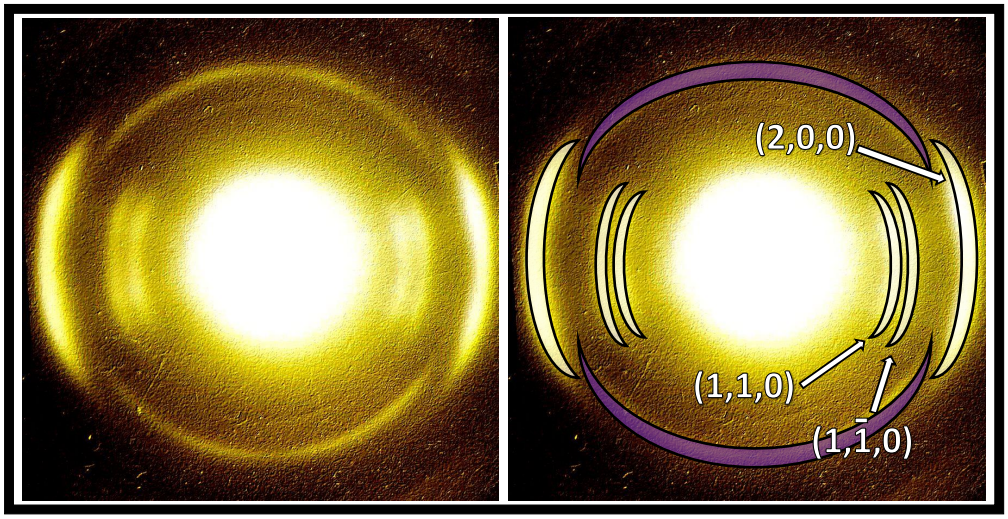

Figure 3.37: Two dimensional diffraction pattern of a raw flax yarn.

The bright arcs seen at either side of the centre in Figure 3.37 correspond to the peaks seen previously in 2θ scans of the raw yarn. (Refer to Section 3.3.2, specifically Figure 3.27). Moving horizontally outwards from the centre, the bright arcs correspond to the cellulose I peaks situated at 14.8 °, 16.7 ° and 22.7 ° in 2θ. As previously stated, there appears to be no discernible cellulose II in the raw yarn. This fact is again verified here by the absence of Bragg peaks corresponding to the cellulose II lattice. The large, dimmer ring shown in purple is thought to be caused by amorphous cellulose. This ring has a large degree of radial uniformity due to the highly randomised direction of cellulose chains in this phase.

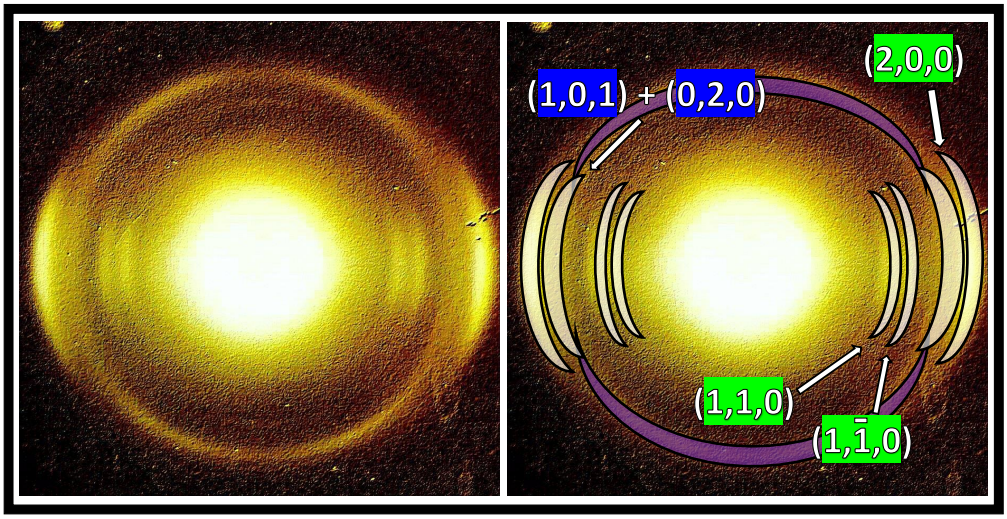

Figure 3.38: Two dimensional diffraction pattern of a yarn processed at 60 °C for 2 hours, with cellulose I peaks shown in green and cellulose II peaks in blue.

Figure 3.38 documents the two-dimensional diffraction pattern resulting from a partially dissolved yarn. The bright arcs corresponding to the cellulose I crystal lattice (seen previously in Figure 3.37) are again labelled, though are now seen to be smaller and less bright- indicating a reduction in cellulose I. In contrast, the dominant cellulose II peaks are now visible and are labelled by their Miller indices (1, 0, 1) and (0, 2, 0) - the similarity of their peak locations however (20.5 ° and 21.3 ° in 2θ) make it difficult to distinguish the two. For this reason, the dominant cellulose II peaks are highlighted together as one single peak. The smaller cellulose II peak situated at 11.9 ° in 2θ is difficult to perceive here- due to its close proximity to the cellulose I peaks (situated at 14.8 ° and 16.7 ° in 2θ) and its relatively small amplitude. The amorphous ring (again shown in purple) remains clear.

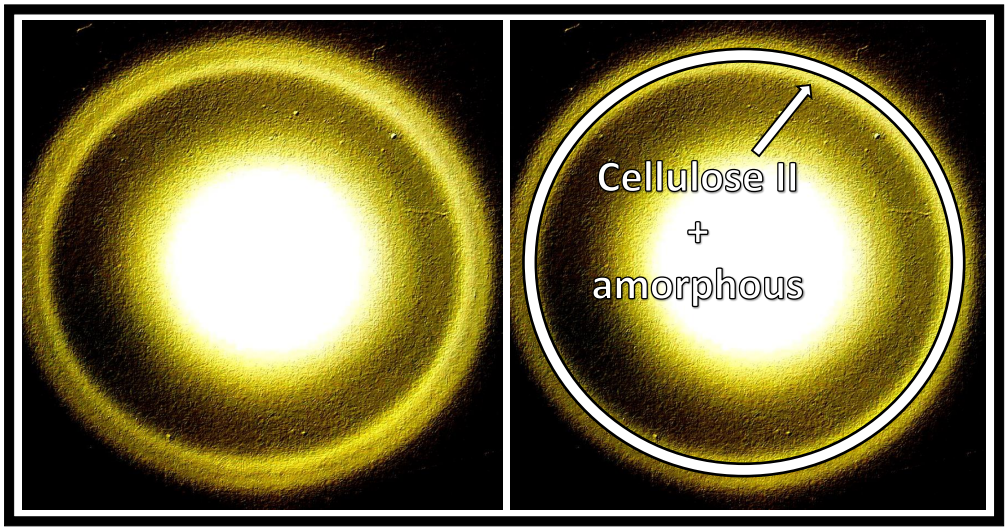

Figure 3.39: Two dimensional diffraction pattern of a cellulose film.

Figure 3.39 displays the diffraction pattern resulting from a cellulose film. The large outer ring is thought to represent a combination of the two main cellulose II peaks (situated at 20.5 ° and 21.3 ° in 2θ) and the amorphous peak (situated around 18 ° in 2θ). The smaller cellulose II peak located at 11.9 ° in 2θ can also be identified, though is seen to be much more faint than the dominant peaks. This diffraction pattern is in agreement with the corresponding digital XRD scan (of a totally dissolved yarn) seen in Figure 3.30 in the previous section- both scans show a large amount of cellulose II and amorphous material, with an absence of cellulose I.

Lastly, Figure 3.40 highlights the differences between diffraction patterns. From the left (raw yarn) to the right (complete dissolution), the trend from cellulose I to cellulose II and amorphous material is clear.

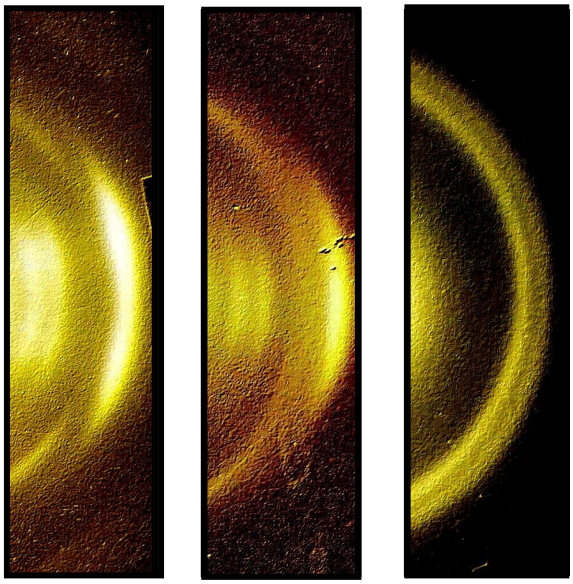

Figure 3.40: Slices of all thee diffraction patterns. Left: raw yarn, middle: partially dissolved yarn and right: fully dissolved yarn.

3.3.4 Mechanical Testing

To begin the mechanical testing of yarns, six individual raw yarns were separately placed under tension and taken to breaking point. Figure 3.41 shows the point at which breakage occurred for one such sample. Figure 3.42 then documents the stress-strain curve for each raw yarn tested.

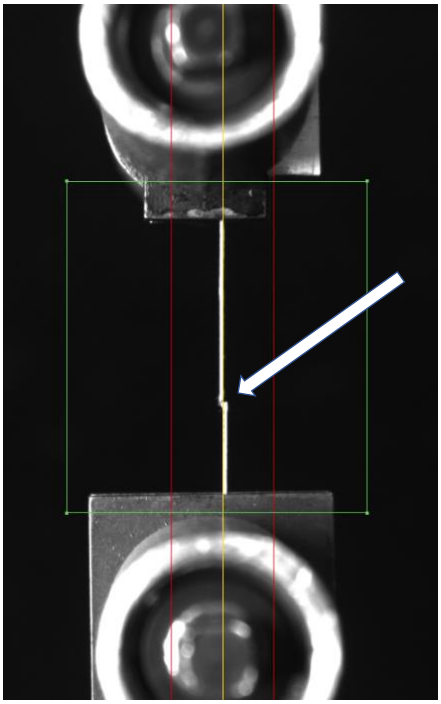

Figure 3.41: Image showing a yarn post-testing. The white arrow highlights the point at which breakage occurred.

Many of the stress-strain curves of raw yarns seen in Figure 3.42 do not display an initial linear trend, instead, a steadily increasing gradient is seen up until the point of linearity. This non-linear fraction of the curve may be due to the untwisting of the yarn as strain is applied. As the modulus is taken from the linear fraction of the curve only, this untwisting effect is not thought to affect the recorded modulus or strength values. This non-linear fraction of the curve is less pronounced for the stress-strain curves of processed yarns (seen in Figure 3.43) owing to the fact the coagulated material is able to bind together sub-fibres and thus prevent untwisting.

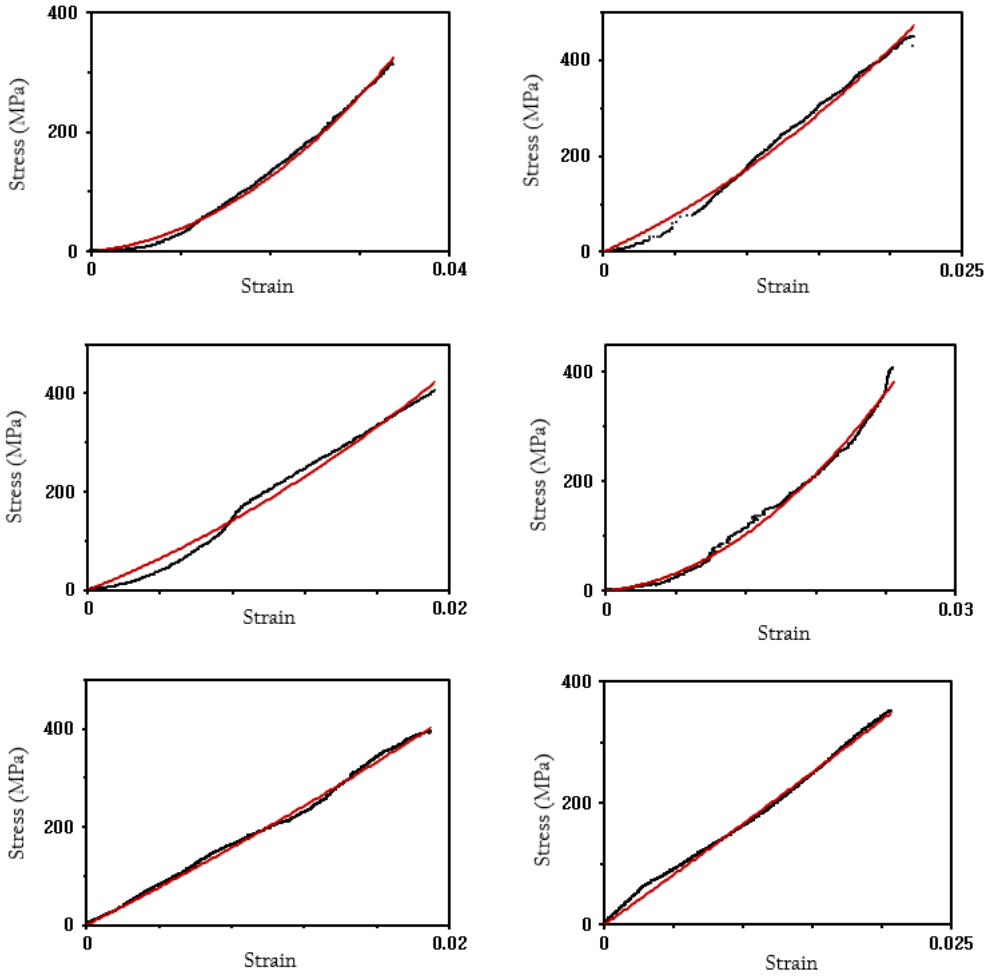

Figure 3.42: Stress-strain curves of six distinct raw flax yarns. Red lines are polynomial fits to the data with intercepts set to Y = 0.

All raw yarns display a good level of agreement with respect to their mechanical properties, with an average tensile strength, modulus and extension to failure (ETF) value of 398 ± 22 MPa, 18.7 ± 1.7 GPa and 2.6 ± 0.3 % respectively. These values are in good agreement with other published works documenting the mechanical properties of flax. [208, 199]

Table 3.7 summarises the average Strength, Modulus and ETF values of raw flax yarns.

Table 3.7: Mechanical characteristics of raw flax yarns

	Strength (MPa)	Modulus (GPa)	ETF (%)
Average	397.7	18.7	2.6
Error	22.4	1.9	0.3

As well as raw yarns, Figure 3.43 shows typical stress-strain curves of processed yarns. These yarns exhibit various CF values, ranging from 0.3 to 0.5. As the CF raises, the strength and tensile modulus are seen to decline.

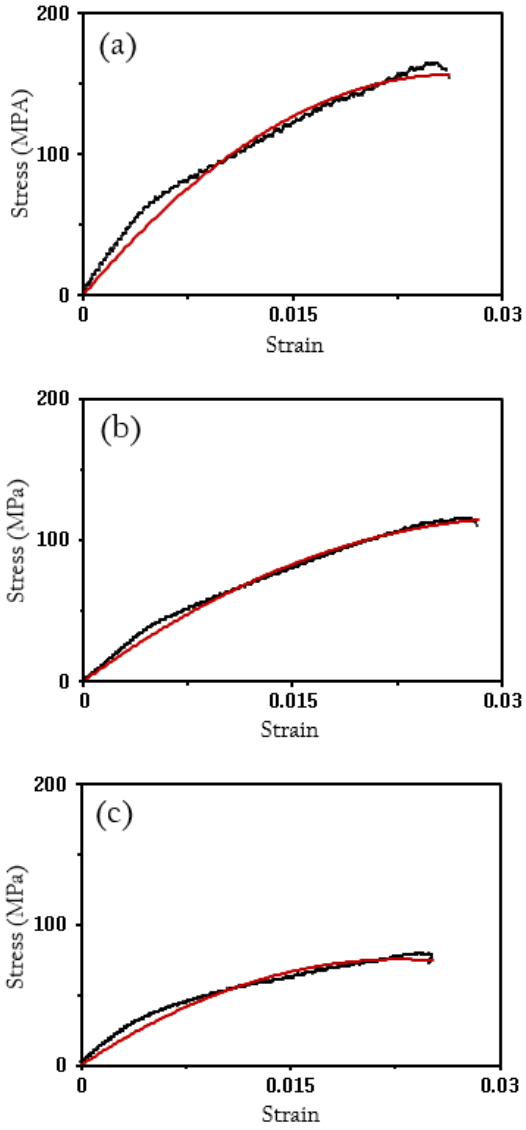

Figure 3.43: Stress-strain curves of yarns with a CF of 0.3 (a), 0.4 (b) and 0.5 (c). Red lines are polynomial fits to the data with intercepts set to Y = 0.

Figure 3.44 shows how the modulus of yarns varies in accordance with the CF. It is interesting to note that the modulus initially increases. This may appear counter-intuitive, as the modulus may be expected to drop as the central (strength-providing) yarn is dissolved away. To explain this behaviour, it is postulated that at low CF values there is a lack of coagulated material available to bond together individual sub-fibres. This results in a minority of sub-fibres baring the entire mechanical load, resulting in a relatively low modulus. As the CF increases however, a network forms between the sub-fibres through which the load may be distributed more evenly; a phenomenon commonly observed in the literature [209, 210, 211]. The modulus is seen to increase as this network of coagulated cellulose spans across more of the fibrous cross section. This initial stage is labelled the 'pre-forming phase'.

The positive correlation between CF and increasing modului is seen to continue until the CF is approximately 0.2, which marks the optimum amount of coagulated material. Past this point however, the favourable balance between coagulated cellulose and the raw fibrous cores is lost- resulting in a near linear decrease in the modulus. A simple schematic of the hypothesised stress response mechanism is shown for both a raw and processed yarn in Figure 3.45.

The data point corresponding to a CF value of 1 in Figure 3.44 was attained using a cellulose film. Refer to section 2.2 for details on film creation. A linear trend is fit to data points outside of the pre-forming phase. By extrapolating this fit backward to the point at which the CF is 0, the 'true' modulus of the raw yarn can be deduced.

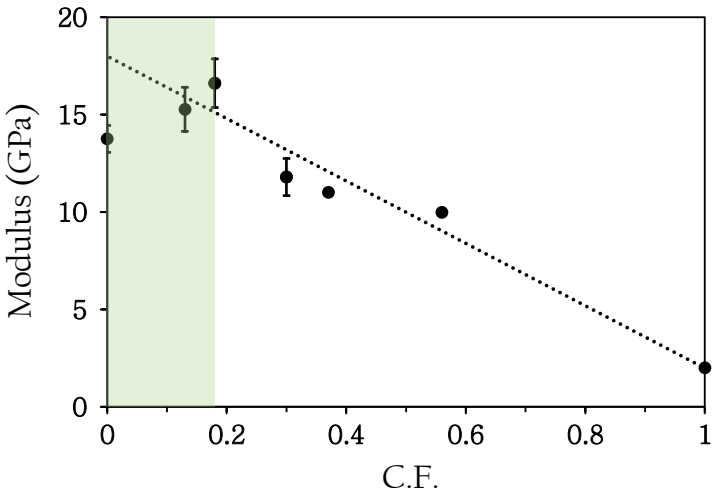

Figure 3.44: The tensile modulus as a function of CF for flax fires, with the shaded area representing the 'pre-forming' phase. Dashed line is a linear fit of the data outside of this phase. Some error bars may be smaller than data points.

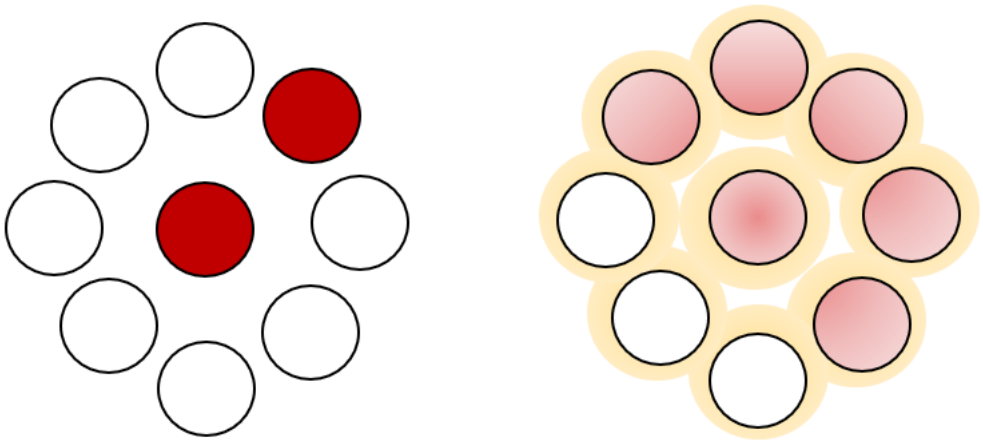

Figure 3.45: Schematic of the hypothetical stress response mechanisms in a raw yarn (left) and a processed yarn (right). Circles represent sub-fibres, with areas experiencing stress shown in red. The coagulated material, through which stress can be distributed is shown in yellow. On the left, the raw fibre is shown to experience the majority of the mechanical load via a few select sub-fibres, whereas the processed sample on the right is able to share the load more evenly via the coagulated network between sub-fibres.

Figure 3.46 documents the tensile modulus of yarns as a function of both processing time and temperature. Within this plot, the data corresponding to the aforementioned 'pre-forming phase' have been removed, leaving only the pertinent section of the modulus curves. As the modulus is directly related to the ratio of dissolved to undissolved cellulose, it was postulated that this data could be used to track the dissolution rate as a function of temperature. As with the data analysis in previous sections, TTS was implemented. The data presented in Figure 3.46 can be seen expressed in *ln time* in Figure 3.47. From here, the data is shifted in the ln time domain using the shift factors documented in Table 3.8, resulting in a master curve revealing TTS in relation to the modulus data (see Figure 3.48).

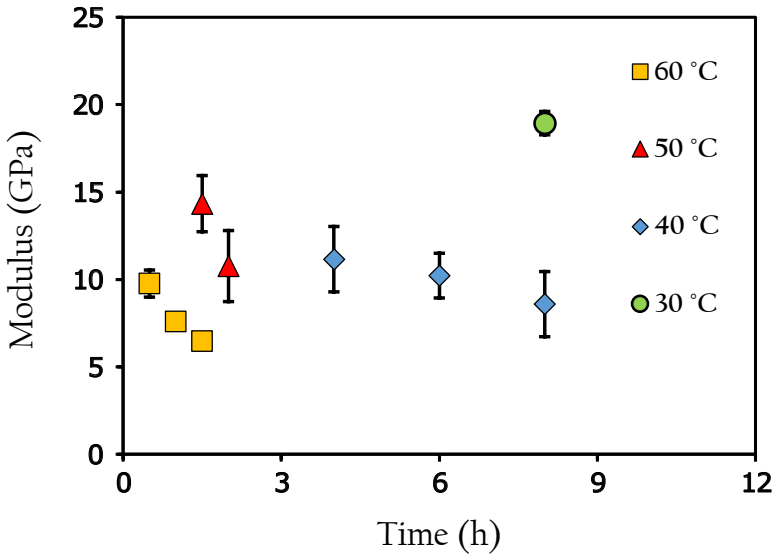

Figure 3.46: Modulus expressed as a function of processing time and temperature. Some error bars may be smaller than data points.

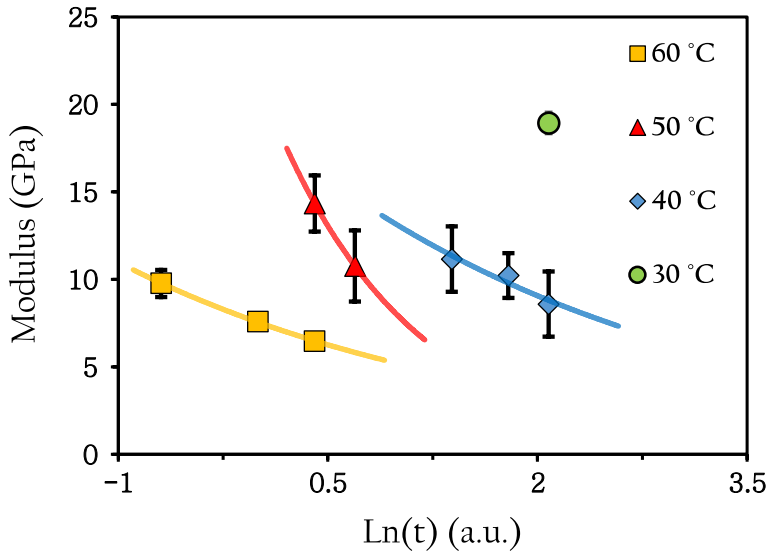

Figure 3.47: Modulus expressed in ln time as a function of processing time and temperature. Polynomial fits used to guide the eye. Some error bars may be smaller than data points.

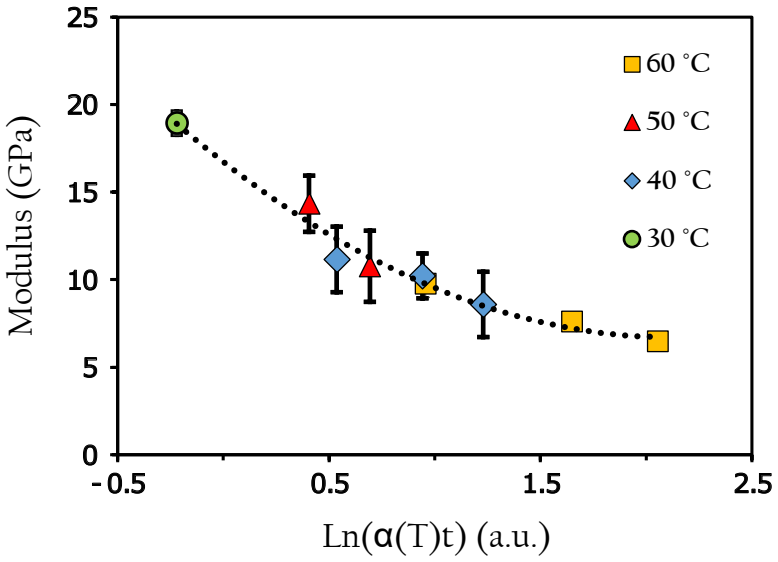

Figure 3.48: Master curve documenting the time-temperature superposability of the tensile modulus data. Polynomial fit used to guide the eye. Some error bars may be smaller than data points.

Table 3.8: Shift factors as a function of processing temperature (modulus data).

Temperature (°C)	ln(α(T))	Error in ln(α(T))
30	-2.3	0.3
40	-0.85	0.3
50	0	0.2
60	1.65	0.2

The shift factors are subsequently used to form an Arrhenius plot (see figure 3.49), where an E_a of **107 ± 10 kJ/mol** is determined. This value is similar to the E_a determined in section 3.3.1 when using optical microscopy (**100 ± 10 kJ/mol**) and close to the E_a determined in section 3.3.2 (**87 ± 16 kJ/mol**) when using digital XRD. The similarity of these values suggest that the various activation energies determined thus far are all related to the same phenomenon-namely, the transformation of raw material to coagulated cellulose.

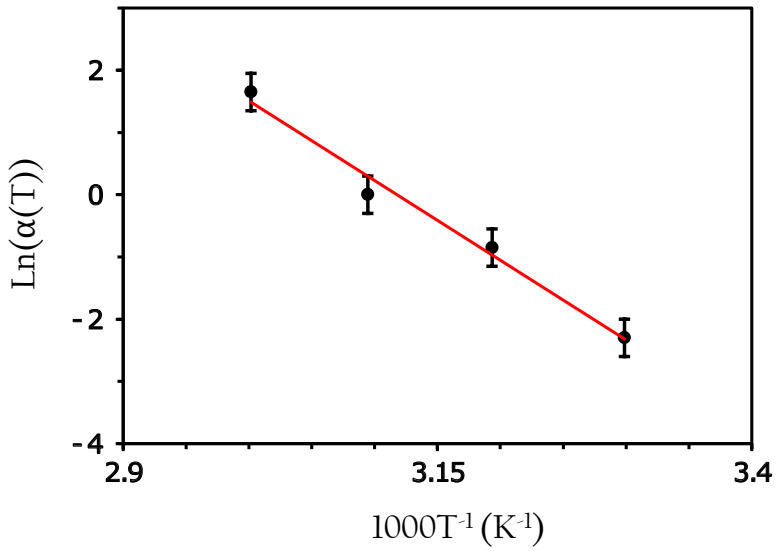

Figure 3.49: Arrhenius plot documenting how the shift factors attained from the modulus data vary with processing temperature. The red line is a linear fit to the data.

As with the modulus, the strength of processed yarns is also plot as a function of dissolution time and temperature. This relation can be seen in Figure 3.50. The strength is directly proportional to the amount of reinforcing phase (undissolved yarn) and as a result- the reduction in strength can be viewed as a marker for the amount of cellulose dissolved and time-temperature superposed accordingly. Figures 3.51, 3.52 and 3.53 document the now familiar steps taken to arrive at an Arrhenius plot, with the shift factors used to create the master curve documented in Table 3.9. The activation energy resulting from Figure 3.53 is found to be **102 ± 17 kJ/mol**. This value is also within error of the E_a attained via optical microscopic measurements in section 3.3.1 and the E_a found when using XRD in section 3.3.2.

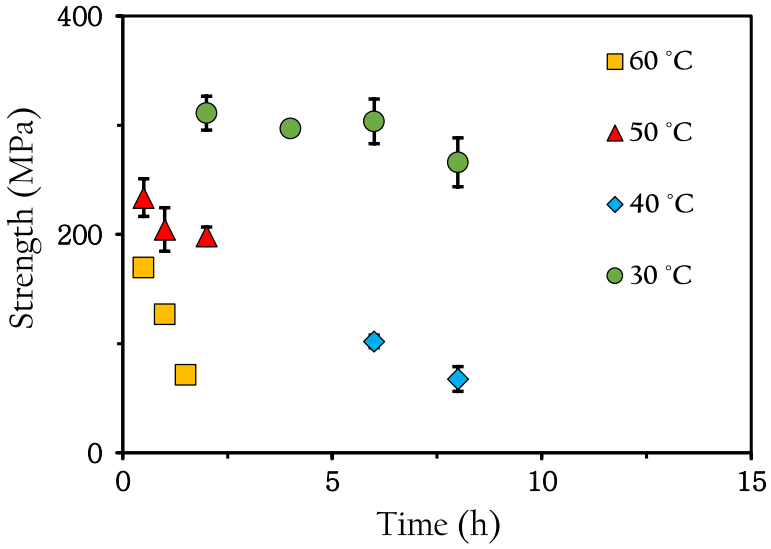

Figure 3.50: Strength expressed as a function of processing time and temperature. Some error bars may be smaller than data points.

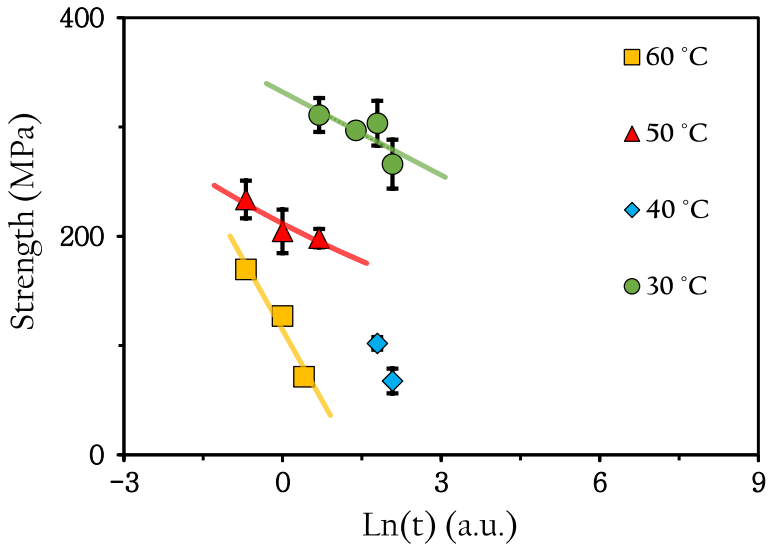

Figure 3.51: Strength expressed in ln time as a function of processing time and temperature. Linear fits used to guide the eye. Some error bars may be smaller than data points.

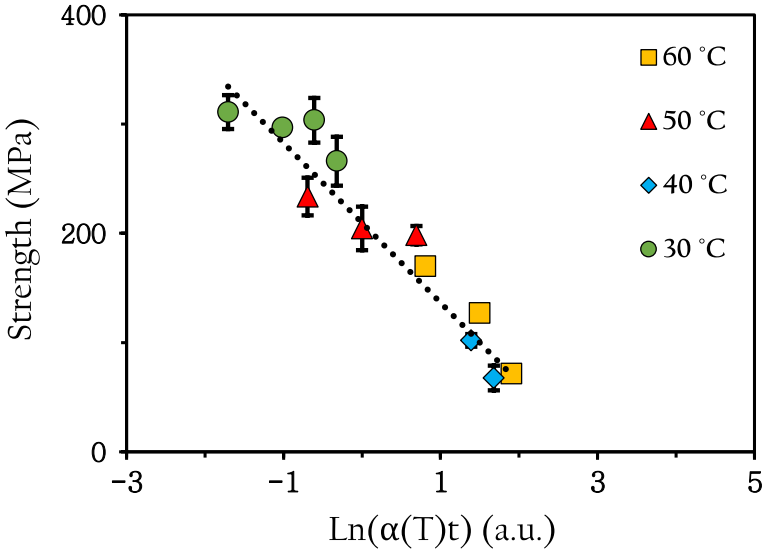

Figure 3.52: Master curve documenting the time-temperature superposability of the mechanical strength data. Linear fit used to guide the eye. Some error bars may be smaller than data points.

Table 3.9: Shift factors as a function of processing temperature (strength data)

Temperature (°C)	ln(α(T))	Error in ln(α(T))
30	-2.4	0.3
40	-0.4	0.2
50	0	0.3
60	1.5	0.2

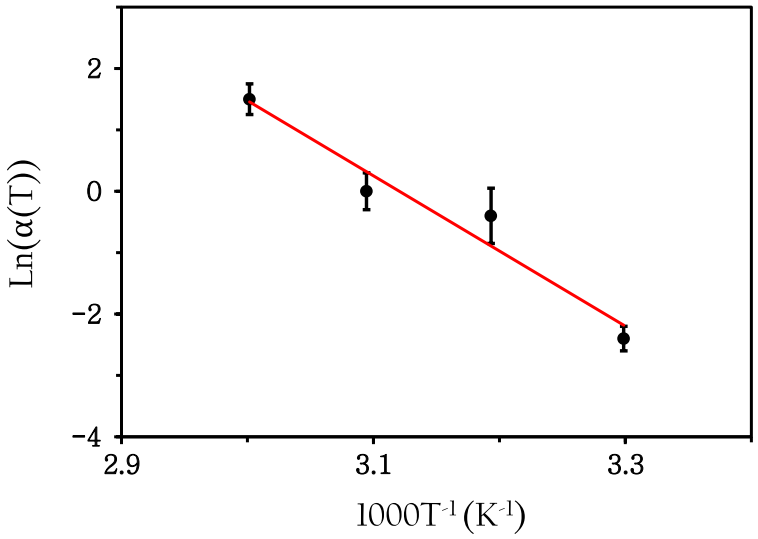

Figure 3.53: Arrhenius plot documenting how the shift factors attained from the strength data vary with processing temperature. The red line is a linear fit to the data.

3.4 Conclusions

This chapter has studied the the dissolution rate of flax yarns in the ionic liquid [C2mim][OAc] as a function of dissolution time and temperature. Analysis has been performed via three key methods: Optical microscopy, x-ray diffraction and mechanical testing.

Using optical microscopy, the raw yarn was photographed and found to be comprised of many smaller sub-fibres. A tight packing of these sub-fibres was evident and it was theorised that the high concentration of fibrous material may prevent the solvent from penetrating deep into the core of the yarn. Within the optical micrographs of processed yarns, a notably different outer layer was seen to enclose the undissolved fraction. The boundary between this outer layer and inner core was exceptionally clear and the outer layer was seen to increase in size as a function of both processing time and temperature. The outer layer was theorised to be composed of coagulated cellulose, which was later verified to be the case upon analysis of X-ray diffraction scans. The difference in appearance

between the two distinct regions allowed for the amount of coagulated cellulose to be mapped as a function of both dissolution time and temperature. The formation of coagulated material was seen to slow at longer times, which is thought to be due to the outer layer acting as a barrier between the solvent and undissolved yarn, hindering dissolution. Upon changing the dissolution temperature, the time-scales on which the coagulated material forms were altered, with higher temperatures resulting in a more rapid rate of growth. This finding suggested an equivalence between time and temperature, which was subsequently verified by the shifting of data in the natural logarithmic time domain. When shifted, each temperature dependant data set was found to overlap, forming a master curve. The shift factors used to generate this master curve were plot against the inverse of their respective dissolution temperatures and upon doing so, a linear relation revealed Arrhenius behaviour in the system. As a result, an activation energy was calculated- describing the energy required for the dissolution of flax based yarns in [C2mim][OAc]. This energy was found to be 100 ± 10 kJ/mol.

Following the optical analysis, digital XRD was next used to determine the crystalline profile of yarns by looking at the relative size of crystal peaks in 2θ scans. From this analysis, it was found that the raw yarn is composed primarily of cellulose I (53 %), with the remainder being amorphous cellulose. As expected, the cellulose I fraction was seen to decrease upon processing. At the same time, the cellulose II fraction and amorphous content were seen to grow, providing evidence of the transformation from CI to CII. Scans of fully dissolved samples were shown to include no cellulose I, validating our assumption that the reduction in CI is a reliable marker of the total dissolution. This finding also confirmed that the coagulated material is indeed comprised of cellulose II and amorphous material. The reduction in CI allowed for a measure of the CF to be calculated and graphed as a function of dissolution time and temperature. As with the optical data, XRD data was itself shifted in the ln time domain to form a master curve. The resulting Arrhenius plot revealed an activation energy of 87 ± 16 kJ/mol - within error of the E_a determined optically. The slight difference in these two values was theorised to be caused mainly by the differing geometry between single yarns (used in the optical method) and arrays of yarns (used in the XRD method), with the latter having less surface area available for the

solvent to act upon. Another potential reason for this difference may be due to the assumption that the CI is homogeneously dispersed throughout the raw yarn. This assumption allowed for the calculation of the CF from XRD data, but may in fact not be the case. Despite this, the CF growth resulting from these two methods of analysis showed a good level of agreement when plot against each other.

As well as digital XRD, an analogue approach was also used in order to view the full two-dimensional diffraction pattern. X-ray sensitive films encoding this pattern were acquired for the raw yarn, a processed yarn and a fully dissolved yarn. Within these images, bright spots corresponding to various Bragg peaks gave an indication as to the crystalline make-up of yarns. As with the digital XRD data, a clear trend is seen in the reduction of CI whilst a corresponding rise is seen in the CII and amorphous content as dissolution progresses. These films also verified the complete absence of CI in a fully dissolved sample.

Lastly, the mechanical properties of both raw and processed yarns were determined. The raw yarn was found to have a tensile strength and modulus of 398 $\pm$ 22 MPa and 18.7 $\pm$ 1.7 GPa respectively- in good agreement with other published works. As the processing time and temperature were increased, a corresponding decrease was observed in the modulus and strength of yarns. A 'pre-forming' stage was identified whereby the network of coagulated material between sub-fibres was yet to have reached an optimum amount. Upon removal of the data corresponding to this pre-forming stage, both the strength and modulus data sets were found to independently time-temperature superpose. This gave rise to a further two master curves and Arrhenius plots, with activation energies of 107 $\pm$ 10 kJ/mol (modulus data) and 102 $\pm$ 17 kJ/mol (strength data). These values were seen to be strikingly close to the activation energy determined via optical microscopy.

Table 3.10 summarises the various activation energies determined by each method.

Table 3.10: Activation energy as a function of method of analysis.

Method	Ea (kJ/mol)	Error in Ea (kJ/mol)
Optical Microscopy	100	10
XRD (Digital)	87	16
Mechanical (Modulus)	107	10
Mechanical (Strength)	102	17

It can therefore be concluded that the dissolution of flax yarns when dissolved in [C2mim][OAc] obeys an Arrhenius law. Time-temperature superposition is evident and an average activation energy of 99 $\pm$ 13 kJ/mol appears to be required in order for dissolution to occur. This value is thought to relate to the energy needed to break apart the fundamental bonds within the cellulose I crystal, though the exact meaning of E_a remains unknown.

Chapter 4

Addition Of The Co-solvent Dimethyl Sulfoxide

4.1 Introduction

As covered in section 1.7, co-solvents are often used in the processing of cellulosic biomass, though little is known about the influence mechanisms of co-solvents on the molecular level [115]. Some typical co-solvents often used in conjunction with ionic liquids (IL's) are dimethyl sulfoxide (DMSO), N,N-dimethylformamide and methanol [212]. Such compounds are often used alongside the primary solvent in order to speed up a reaction/lower the cost of processing/improve solubility [213].

The previous chapter presented a study into the effects of temperature on the dissolution of flax yarns submerged in [C2mim][OAc]. The following chapter now explores the effects of a co-solvent- dimethyl sulfoxide- on the system, the structure of which can be seen in Figure 4.1.

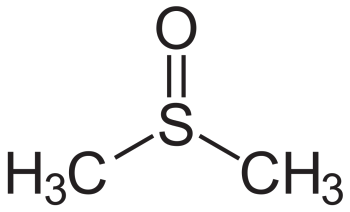

Figure 4.1: Molecular structure of Dimethyl Sulfoxide.

Dimethyl Sulfoxide (CH3)2SO, discovered in the latter half of the 19th century is a by-product from wood pulp created during the production of paper [214]. It is a polar, aprotic solvent, colourless and miscible in water, with a high level of thermal stability and high boiling/melting points (189 °C and 19 °C respectively). Widely used in biomedical fields for the cryopreservation of cells and as a penetration enhancer during topological treatments [215, 216], it has also been shown to be an excellent solvent for many organic and polymeric compounds due to its high polarity [217]. Though DMSO cannot dissolve cellulose, its low cost, low toxicity and low viscosity make it a good candidate for a co-solvent. DMSO is believed to improve the solvation capacities of ionic liquids by facilitating mass transport as a result of lowering the viscosity of the system [218]. Others have shown that DMSO is, however, also able to interfere with the interactions between the anions and cations of ionic liquids [111]. Radhi et al. reports that the addition of DMSO reduces the differences between diffusivities of the cation and anion in [C2min][OAc]. The ratio of the cation to anion diffusivities tends to unity around 0.6 mole fraction of DMSO, whereas higher DMSO concentrations result in the diffusivity of the anion being faster than that of the cation [219]. It is however unknown as to whether such phenomena play an appreciable role in the context of cellulose dissolution.

4.2 Methods

DMSO was added as a co-solvent at various concentrations. In order to understand its effects on dissolution, yarns were again partially dissolved and photographed under a microscope. DMSO was mixed into the IL with a magnetic stirrer for 10 minutes prior to use at three different concentrations: 20 %, 50 %

and 75 % by weight.

Dymethyl sulfoxide is hygroscopic and will readily form H-bonds with water molecules [220]. Simulations have shown how this can occur in two distinct ways: 1) Two water molecules can H-bond to the oxygen atom of a DMSO molecule, such that the angle between the two H-bonds is almost tetrahedral and 2) A central H_2O molecule is able to attach to two neighbouring DMSO hydrogen's- see Figure 4.2 [221]. The hygroscopic nature of the co-solvent therefore required the removal of all moisture from the dissolution environment. However, the vacuum used previously (throughout chapter 3) was not applicable for the IL + DMSO system due to the relatively high vapour pressure of the co-solvent at the temperatures used [222, 223]. Preliminary experiments were conducted to measure the rate of evaporation of DMSO when under vacuum and the results are shown in Figure 4.3. The data in this figure confirm the infeasibility of a vacuum environment during dissolution and for this reason, a different approach had to be implemented in order to keep the solvent bath dry. The solution was to use the same Leybold Sogevac oven (used throughout Chapter 3) during dissolution, but to replace the vacuum with nitrogen. All experiments presented within this chapter were conducted within this nitrogen atmosphere. All other experimental methods used are identical to those outlined in section 2.1.

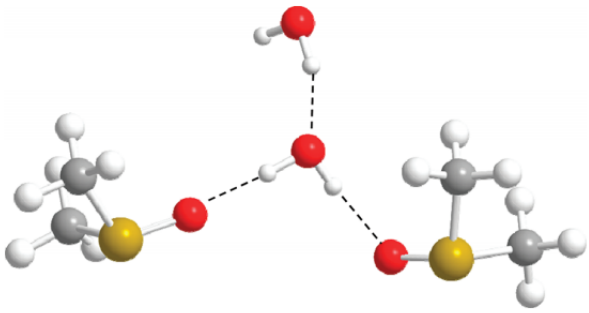

Figure 4.2: A water molecule bridging two DMSO molecules via h-bonds, with a second water molecule hydrogen bonded to the bridging water molecules oxygen. Figure adapted from a snapshot taken from an MD simulation by Borin et al. [220]

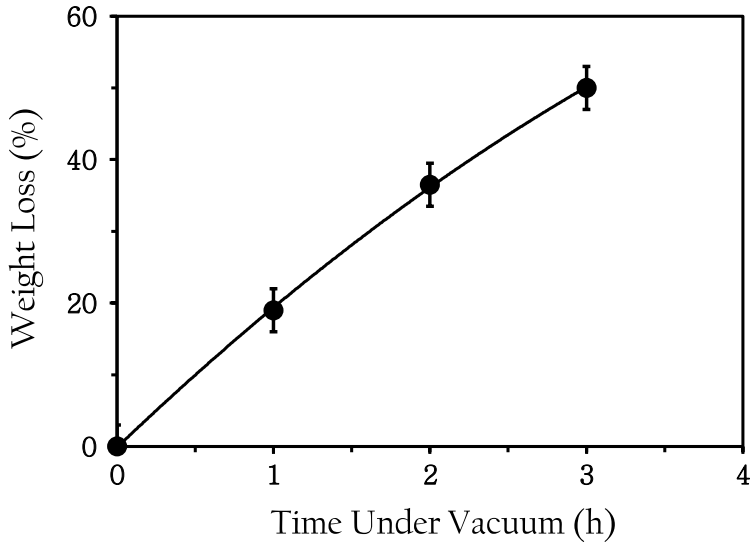

Figure 4.3: DMSO evaporation rate when under vacuum at 50 °C. Standard errors calculated using equation 2.1. Polynomial fit used to guide the eye.

4.3 Results and Discussion

The most obvious difference in the IL + co-solvent system was the marked change in viscosity, as DMSO has been shown to alter the viscosity of [C2mim][OAc] by up to two orders of magnitude [219]. In a similar system consisting of 1-ethyl-3-methylimidazolium chloride, DMSO and cellulose, Lu et al. found the viscosity activation energy to depend on cellulose concentration- ranging from 35 kJ/mol for the pure solvent to 75 kJ/mol at 10 wt % of cellulose [224].

The dissolution mechanism seen in the IL + co-solvent system was found to remain the same as that of the pure IL system; yarns continue to dissolve from the outside in, with the formation of a coagulated layer appearing around the core. Figure 4.4 documents the appearance of yarns after a dissolution time of 30 minutes for all co-solvent concentrations (including 0 %.) From this image, it can be seen that the co-solvent concentration is effecting the growth rate of the coagulated layer. It appears that after 30 minutes- the greatest amount of coagulated material is observed when using a co-solvent concentration of 50 %. The viscosity of many ionic liquids is exponentially decreased when mixed

with DMSO [225]. Therefore, the differing dissolution speeds suggest that the co-solvent is, in part, acting to alter the time-scales of dissolution by reducing solvent viscosity [218, 178].

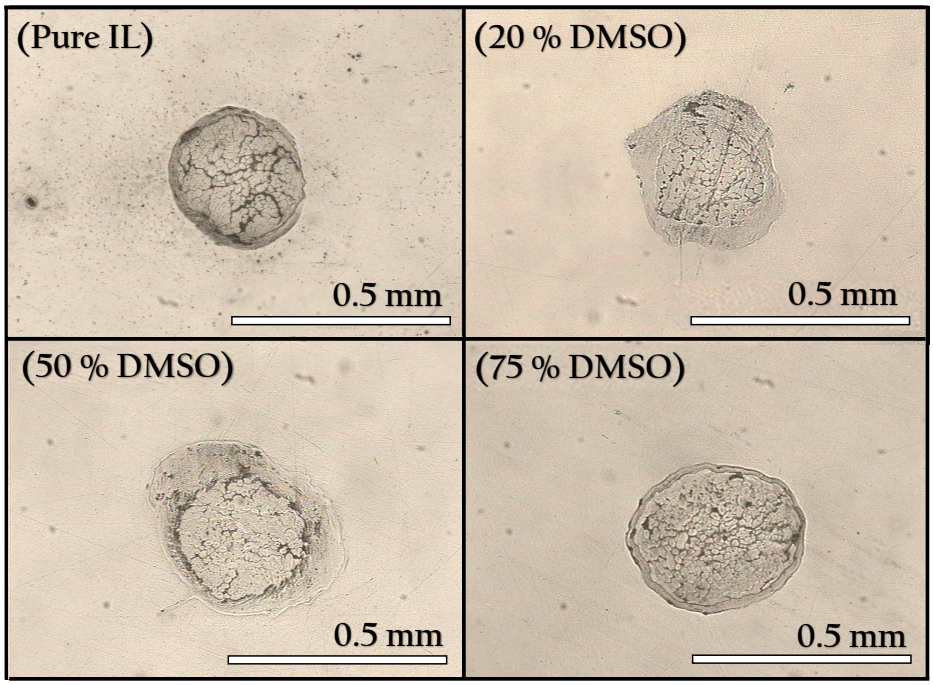

Figure 4.4: Images of yarns processed at 60 °C after a dissolution time of 30 minutes in each system.

As the dissolution process appeared similar to that observed in the previous chapter (other than the time-scales on which the coagulated material forms), it was postulated that once again, time-temperature superposition (TTS) master curves and Arrhenius plots may be generated. Figure 4.5 presents the CF growth as a function of processing temperature when using a co-solvent concentration of 20 %, alongside a corresponding master curve (created by the shifting of data in ln time) and resulting Arrhenius plot. (Refer to section 3.3.1 for a detailed summary of the shifting procedure.) Figures 4.6 and 4.7 follow on by documenting the same analytical process when using co-solvent ratio's of 50 % and 75 % respectively.

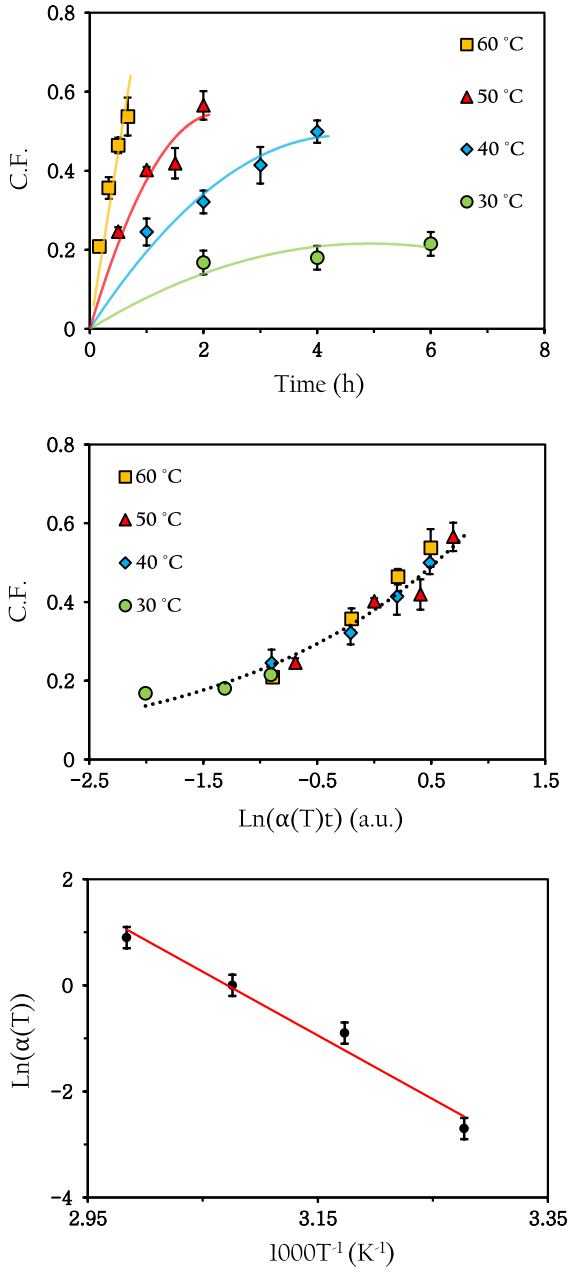

Figure 4.5: Data corresponding to the CF as a function of temperature (top), the shifted data expressed in ln time as a master curve (middle) and corresponding Arrhenius plot (bottom) when using 20 % co-solvent by weight. Polynomial fits used to guide the eye in top and middle plots, with a linear fit to the data in the bottom plot. Error bars used in all plots, though may be smaller than data points.

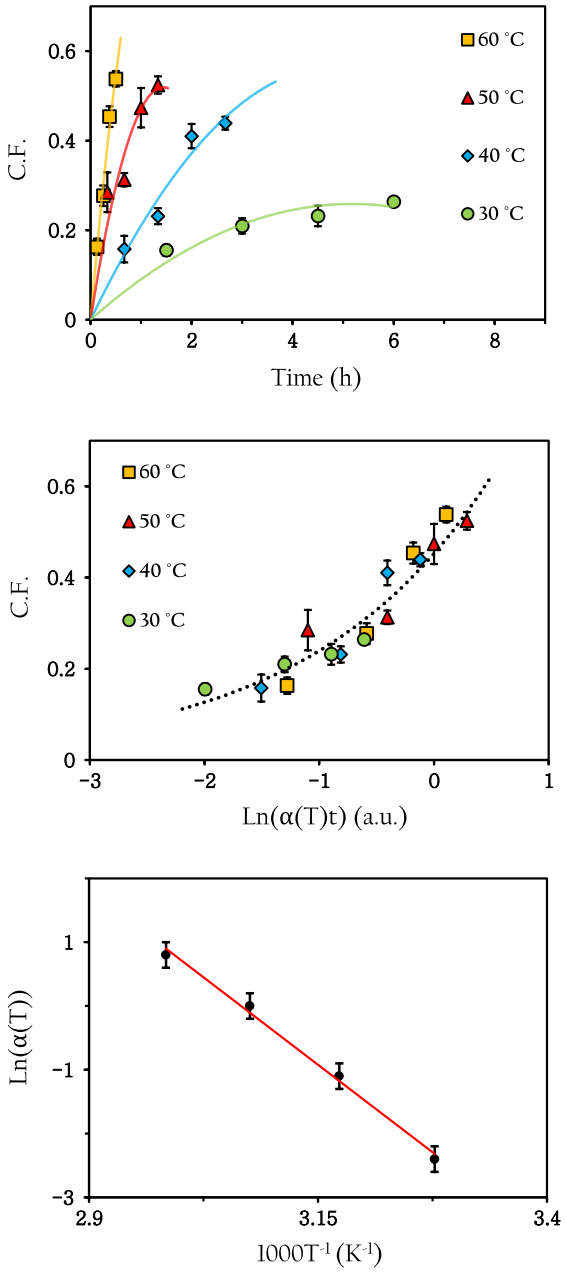

Figure 4.6: Data corresponding to the CF as a function of temperature (top), the shifted data expressed in ln time as a master curve (middle) and corresponding Arrhenius plot (bottom) when using 50 % co-solvent by weight. Polynomial fits used to guide the eye in top and middle plots, with a linear fit to the data in the bottom plot. Error bars used in all plots, though may be smaller than data points.

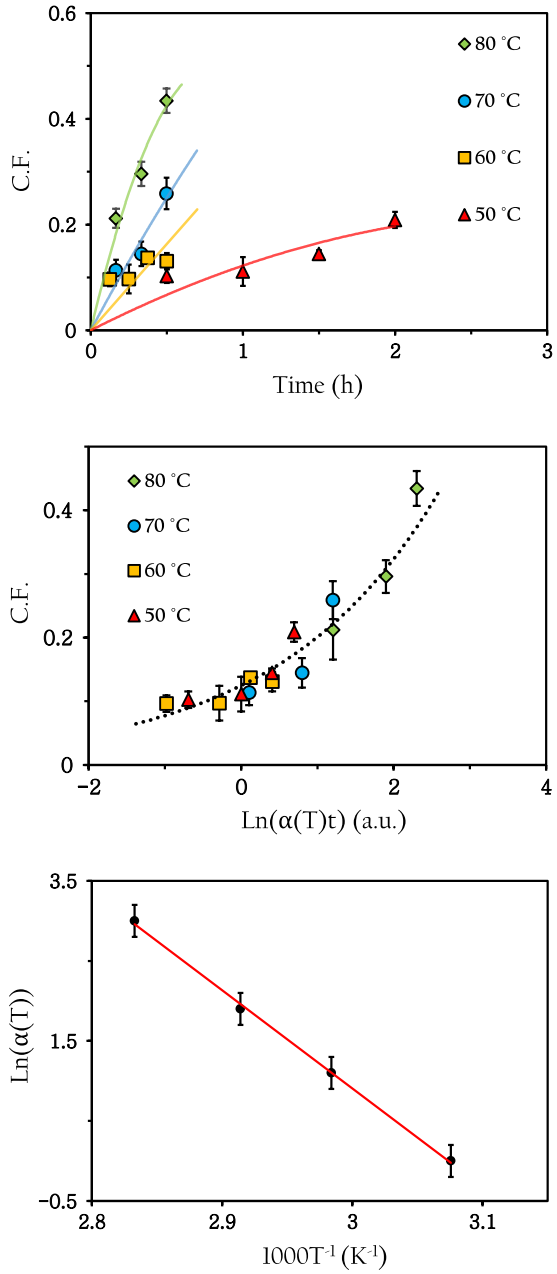

Figure 4.7: Data corresponding to the CF as a function of temperature (top), the shifted data expressed in ln time as a master curve (middle) and corresponding Arrhenius plot (bottom) when using 75 % co-solvent by weight. Polynomial fits used to guide the eye in top and middle plots, with a linear fit to the data in the bottom plot. Error bars used in all plots, though may be smaller than data points.

Figures 4.5, 4.6 and 4.7 show that time-temperature superposition occurs in the system when using DMSO as a co-solvent. From these figures, activation energies of **100 ± 11 kJ/mol**, **91 ± 5 kJ/mol** and **102 ± 3 kJ/mol** are revealed when using 20 %, 50 % and 75 % DMSO by weight respectively. The remarkable consistency of these values, highlighted in Figure 4.8, suggests that the activation energy of dissolution does not depend on the weight fraction of DMSO in the system. The similarities between activation energies suggest that the co-solvent is not acting to alter the energy barrier to dissolution. Rather, it is providing the ionic liquid with more frequent attempts to infiltrate the cellulose h-bond network and thus only altering the pre-factor 'A' in the Arrhenius equation. This result is echoed in the work conducted by Velioglu et.al, whereby they conclude that "DMSO has the role of an 'innocent' co-solvent, which does not interact strongly with cellulose and does not interfere with the interactions of cellulose with the IL, but lowers the viscosity of the medium, leading to faster mass transport and dissolution." [226]

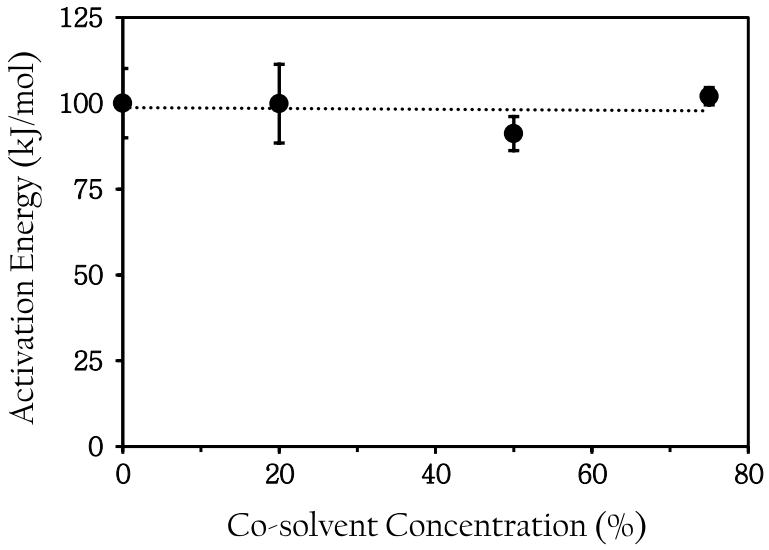

Figure 4.8: Activation energy required for cellulose dissolution as a function of co-solvent concentration. Dashed line shows the average value.

All shift factors used to create the individual co-solvent master curves are themselves plot against the inverse of their respective dissolution temperatures in Figure 4.9. This 'Master Arrhenius' plot documents how all shift factors fall on the same line. From this master fit, an activation energy of **100 ± 3 kJ/mol** is revealed.

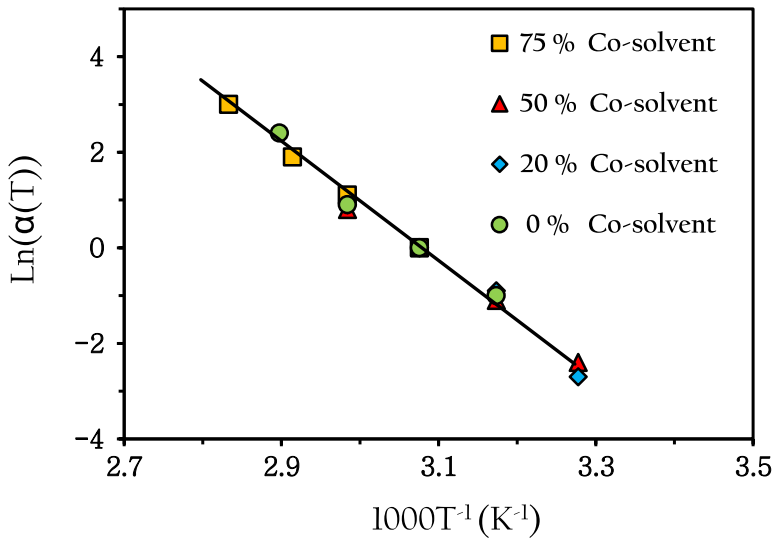

Figure 4.9: Arrhenius plot showing how ln(α(T)) varies for all co-solvent concentrations and dissolution temperatures. Black line is a linear fit to all data.

The co-solvent master curves seen previously in Figures 4.5, 4.6 and 4.7 are next individually shifted in ln time so as to fall onto the same curve for that of the pure ionic liquid results (shown previously in Figure 3.24). The resultant co-solvent master curve, shown in Figure 4.10 displays the CF variance as a function of time, temperature and co-solvent concentration.

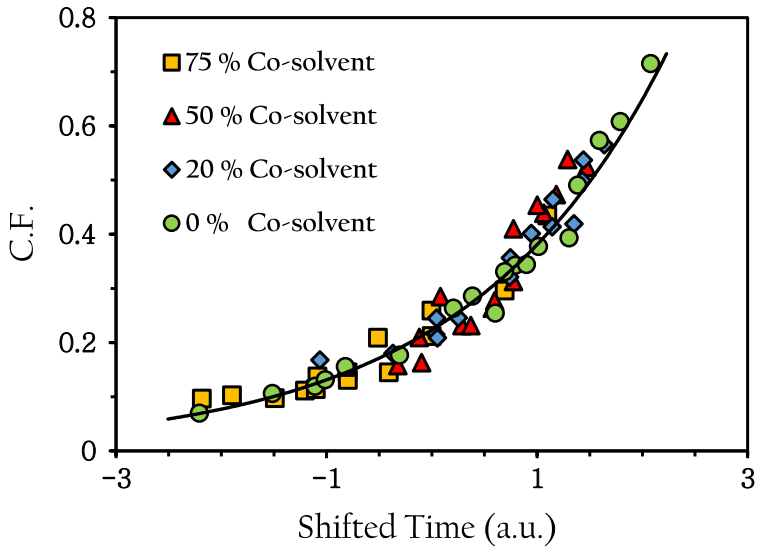

Figure 4.10: Master curve showing the coagulation fraction across all temperatures and all co-solvent concentrations. Each data set uses 50 °C as the reference temperature. The black line represents an exponential fit to all data.

The amounts by which each co-solvent master curve must be shifted in ln time to create Figure 4.10 act as a direct measure of the relative dissolution rates. For example, the data taken when using a co-solvent concentration of 50 % must be scaled by a factor α of 3.3 in order to overlap with the pure [C2mim][OAc] master curve, hence the dissolution rate is 3.3 times faster at this concentration. Figure 4.11 shows how the dissolution rate at each co-solvent concentration varies relative to the dissolution in pure [C2mim][OAc].

Interestingly, the dissolution rate is seen to drop when the concentration of co-solvent is taken above 50 %, this corresponds to a DMSO mole fraction of around 0.65. Radhi et al. report that below this concentration, the DMSO preferentially associates with the cation, which may leave many of the anions free to partake in dissolution by bonding with the hydrogen atoms of the cellulose hydroxly groups [227, 228]. Above this concentration however, it is reported that the DMSO couples more favourably with the anion. It is postulated therefore

that the drop in dissolving power of the IL at higher DMSO fractions is not only due to a shortage of the active solvent, but may also be related to the impediment of the anions by the DSMO.

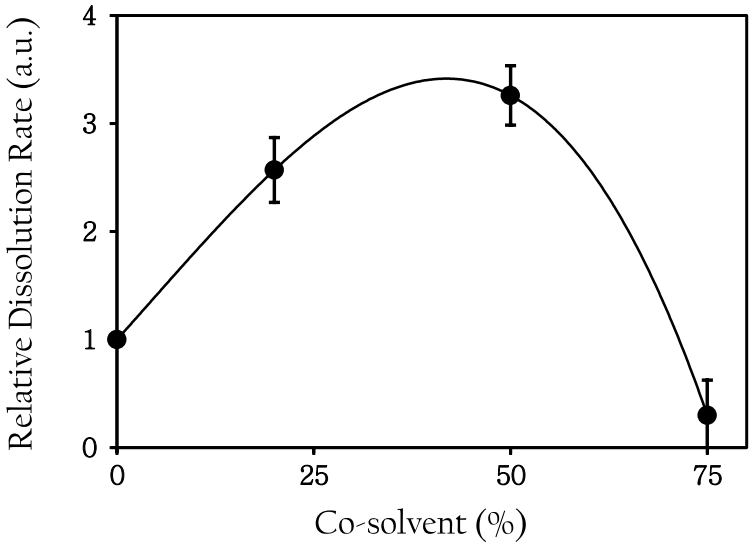

Figure 4.11: The relative dissolution rate of flax yarns as a function of co-solvent concentration. Error bars determined by the error in the shifting of each data set to form to master curve. Polynomial fit used to guide the eye.

4.4 Conclusions

The dissolution rate of flax yarns in the ionic liquid [C2mim][OAc] has been studied as a function of dissolution time, temperature and DMSO concentration. As with the previous chapter, the growth of a coagulated outer layer is seen as dissolution progresses and the growth of this layer has been tracked using optical microscopy. The major difference seen when using DMSO was the rate at which yarns dissolve, suggesting that the co-solvent is merely acting to alter the time-scales of dissolution by reducing the solvent viscosity [229, 147]. Time-temperature superposition was evident at all DMSO concentrations, which allowed for the formation of a CF master curve for each of the co-solvent ratios

used.

Though the co-solvent was found to modify the rate of dissolution, the temperature dependence of the time-scales of dissolution remained remarkably constant. The activation energy of dissolution for each DMSO concentration was shown to be very consistent, with all values falling within the range 100 ± 10 kJ/mol. This independence of E_a on co-solvent concentration implied that the barrier to be overcome in order for dissolution to occur is unaltered by the presence DMSO. The decrease in viscosity of the IL due to the co-solvent, however, may provide solvent molecules with more frequent attempts at overcoming this barrier. Despite the favourable decrease in viscosity, the solvent power is thought to be reduced at higher DMSO concentrations as more co-solvent molecules bind to the anions. This reduction in solvent quality is thought to critically hinder dissolution: an idea documented in the recent findings of Chen et al, whereby it is noted that the dissolution (of cellulose fibres) is not governed primarily by viscosity, but instead by solvent power [178].

The shifting of each master curve in ln time resulted in a co-solvent master curve, where all data was seen to exist on the same curve as that of the pure IL. The shift factors used to create this plot allowed for the determination of the relative dissolution rates between systems, which were subsequently graphed as a function of co-solvent concentration. From this plot- the dissolution rate was seen to be maximised when using an equal amount of [C2mim][OAc] to DMSO, whereby the dissolution process occurred 3.3 times faster than dissolution in [C2mim][OAc] alone.

The findings presented in this chapter can be closely tied to the series of papers published by Nevard et al. on the swelling and dissolution of cellulose fibres in a range of solvents [230, 231, 232, 233]. Solvent mixtures in this series include aqueous NMMO along with a host of additives such as urea and zinc oxide, as well as multiple ionic liquids. The quality of the NMMO as a solvent is shown to be a function of water content, with a high percentage of water resulting in poor solvating properties. Within the NMMO system, two main mechanisms of dissolution are reported- 'ballooning' and 'disintegrating', seen

with high- and low-quality solvents respectively. The 'ballooning' dissolution mechanics are reported to be entirely due to the structure of the cellulose fibres and not the type of solvent, as the same phenomenon is seen when using both aqueous NMMO and ionic liquids. It was found that both cotton and wood fibres, as well as nitrocellulose and xanthene all display similar dissolution mechanics in these systems.

The work undertaken here may also be of interest to the growing study of all-cellulose composites (ACC's) [234, 235]. The preparation of an ACC with good mechanical properties requires the controlled partial dissolution of cellulosic fibres/yarns for optimum bonding, without significant loss of the mechanical properties [236]. The results presented here will hopefully assist in the optimisation of future cellulose based composites, through quantitative control of the dissolution using time, temperature and co-solvent concentration.

Chapter 5

Exploring The Influence Of Water On Dissolution

5.1 Introduction

The previous two chapters have explored the dissolution mechanics of flax yarns when submerged in [C2mim][OAc], both with and without a co-solvent. Within these chapters, time-temperature superposition was observed, dissolution rates quantified and activation energies determined. The following chapter now aims to explore the effects of H_2O on the system via the addition of small amounts of distilled water to the solvent bath.

5.1.1 Interactions between Ionic Liquids and Water

Ionic liquids (IL's) display their own hydrogen bond networks [237]. Within these networks, a single cation can h-bond with up to five different anions and the bond strength between cations and anions is comparable to the bond strength between cations and water molecules [238, 86]. This results in ionic liquids being generally hygroscopic, with a remarkable tendency to absorb atmospheric moisture [239, 240]. Even the allegedly hydrophobic IL's still saturate with a water content as high as 1.4 % by mass [241]. Once water has been absorbed by an IL however, it can also be desorbed by decreasing the humidity of the surrounding environment [241]. The amount of water uptake is amplified when the anion can strongly interact with water molecules via hydrogen bonding, forming an anion

$\cdots$ HOH $\cdots$

anion h-bonded structure [242, 243]. The bond strength between IL and water (approx. 75 kJ/mol) is roughly three times stronger than the bond strength between cellulose and water (21 kJ/mol) [217, 244, 86]. The h-bonds bonds between a single anion and cation within [C4mim][OAc] are shown in Figure 5.1.

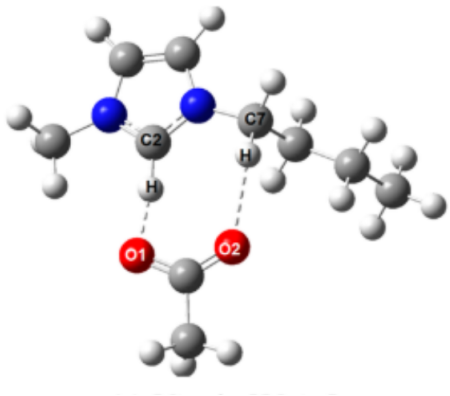

Figure 5.1: H-bonds (dashed lines) between the anion and cation within [C4mim][OAc]. Credit: Zhao 2015 [217]

Weldon et al. found that when room temperature ionic liquids absorb water molecules from the air, these molecules exist mostly in the 'free' state, bound via h-bonding with concentrations of 0.2-1.0 mol/dm^3. The energy of this bonding is in the range of 8-13 kJ/mol [245]. Among ionic liquids, those with an imidazolium base are particularity prone to water absorption [25, 15].

It has also been shown that the diffusivity of the anion and cation can be modified with water content. For imidazolium-based IL's, the cation diffuses faster than the anion when dry- a trend which can be reversed by the addition of water [164]. Studies have shown that the method of absorption is physical, not chemical – with water molecules attaching themselves via Van der Walls forces and h-bonds to the exposed surface of the IL [241]. It has been reported that as little as 1 % water by weight can significantly affect the properties of an ionic liquid- such as melting point, viscosity and vaporisation enthalpy [246, 247].

By absorbing water, the number of available h-bond sites on the anion is reduced. As a result, its capacity to dissolve cellulose is diminished [217]. Many studies have looked at the reduction in dissolving power of IL's as a function of moisture content and it has been reported that the presence of even small amounts of water may severely impede an IL's ability to solvate [248]. This detrimental effect of water on cellulose solvation is well documented [203, 249]. For example; in the cellulose dissolving system consisting of NMMO and H_2O, Cuissinat et al. report that cellulose fibres showed no signs of dissolution if the solvent water content was taken above 35 % by weight [250]. In another system containing [C2mim][OAc] and H_2O, Olsson et al. found that water concentrations as low as 10 % 'largely inhibited dissolution' [251]. A similar study found that cellulose was 'not completely dissolved' if the concentration of water exceeded 15 % by weight when using [C2mim][OAc] as a solvent. Other studies however, quote much higher acceptable values of water content when dissolving cellulose in various other ionic liquids; up to 50 % in some cases before dissolution is 'greatly impacted' [252].

5.1.2 Interactions between Cellulose and Water

As with ionic liquids, the absorption of atmospheric moisture by cellulose is also a well-documented phenomenon [240, 253, 254]. Cellulose features three hydrophilic O-H groups per glucose unit, making the polymer highly polar and prone to the uptake of water. Figure 5.2 shows the multiple ways in which H_2O molecules are able to bind to cellulose, with Figure 5.3 showing the vast h-bond network formed between many cellulose chains in the presence of water. The absorption of water can act to modify certain attributes of cellulose, such as its glass transition temperature and mechanical properties [255, 256], though the level of moisture retention under atmospheric conditions is relatively low (approx. 6 % by weight) [257].

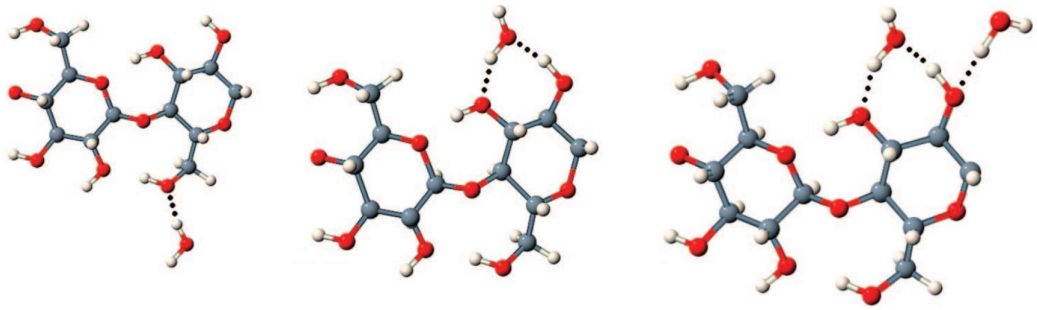

Figure 5.2: Water molecules attaching to multiple available sites on the cellulose polymer. H-bonds represented by black dotted lines. Credit: Deshpande et al. [258]

Within most polymer-water systems, water found within the polymeric matrix exhibits properties different to those of bulk water, with boiling/freezing occurring at different temperatures, if at all [259]. Within cellulose, three main types of water have been identified; *'Free water'* (unbound water with 1^{st} order transition temperatures equal to those of pure water), *'Bound water'* (restricted by hydroxyl groups of cellulose molecules, the transition temperature of which is lower than that of pure water) and *'Non-freezing Water'* (the fraction of water within the polymer phase which remains unfrozen at low temperatures).

Bound water is difficult to remove completely from the polymer matrix, though a fraction of it can be extracted via intensive heating [260, 261, 262]. Water has been shown to only diffuse into the amorphous regions of the polymer, meaning that the degree of absorption is highly dependent on the level of crystallinity [263]. Cellulose-cellulose, cellulose-water and water-water hydrogen bonds are all comparable in magnitude, at around 20 kJ/mol [70, 205]. Water is also well known to plasticise cellulose and as little as 5 % additional moisture can have a significant impact- altering the glass transition temperature by over 100 °C [1, 264].

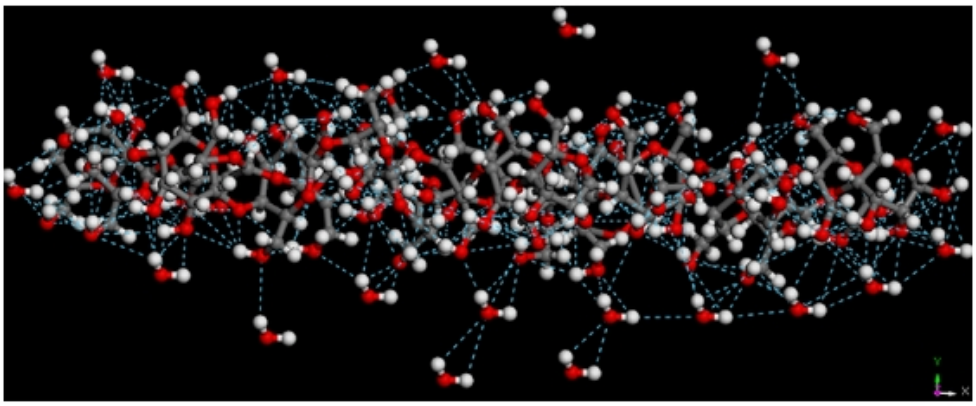

Figure 5.3: Hydrogen bond network between water molecules and cellulose chains. H-bonds shown with blue dashed lines. Credit: Khazraji et al. [263]

5.1.3 Ternary systems involving cellulose, [C2mim][OAc] and water

Few studies have explored the complex network of interactions between ionic liquids, water and cellulose in detail. Liu et al. however, recently reported on a ternary system involving water, cellulose and the ionic liquid [C2mim][OAc] [265]. They conclude that H_2O is able to disrupt the non-covalent interactions between anions and cellulose molecules. They also report that water does not only bind with the anion, but also weakly interacts with the cationic imidazolium ring. Within their simulations, each water molecule bound to [OAc] is seen to be surrounded by small clusters of yet more water molecules (see Figure 5.4). As the concentration of water increases, the hydrogen bonding between anions and water molecules becomes saturated, resulting in the formation of liquid like H_2O aggregates. Interestingly, this aggregation of water molecules means that IL's containing water may not be regarded as homogeneous solvents, but instead have to be considered as nano-structured networks of anions and cations. Within their work, they also discuss the various solvation shells existing around cellulose molecules. At high concentrations of [C2mim][OAc], the anion is shown to have

a very high probability of residing in a solvation shell with a radial distance of approx. 2.3 Å from the cellulose. As the water content is increased however, H_2O molecules diffuse into this solvation shell and begin to supplant some of the cellulose-anion bonds, thus creating a cellulose-water-anion h-bonding network. The authors also note the similarity of the bond strength between cellulose-acetate (12 kcal/mol) and water-acetate (15 kcal/mol). The water concentrations used by Liu et al. are, however, far higher than the concentrations used in this chapter (80 % by weight compared to a maximum of 8 % by weight respectively).

The authors conclude by stating "To date, experimental studies on cellulose/IL/anti-solvent ternary systems have not been conclusive and a mechanistic understanding of the interactions between water, IL and cellulose remains unknown."

It is hoped that the research presented in this chapter shall aid in the understanding of such ternary systems.

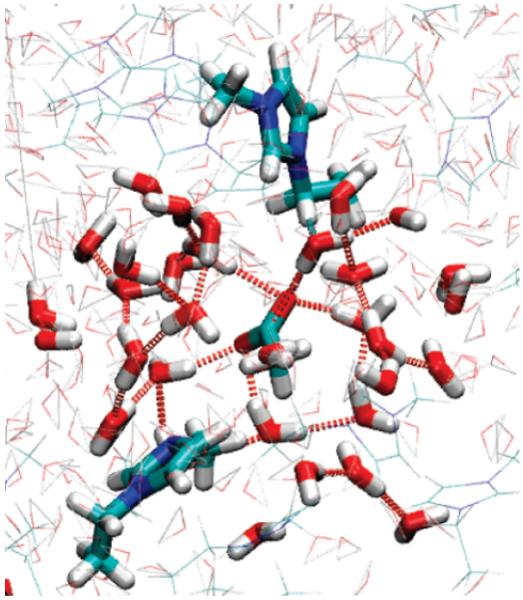

Figure 5.4: Simulation snapshot of H_2O molecules clustering around an anion within [C2mim][OAc]. Credit: Liu et al. [265]

5.2 Methods

Distilled water was added to the ionic liquid at various concentrations. In order to accurately measure the water content of the solvent bath, nuclear magnetic resonance (NMR) was performed using a 'Bruker 400 MHz Avance II NMR spectrometer' capable of measuring the amount of water to an accuracy of 0.5 % by weight. The resulting '^{1}H' scan shows the chemical shift of various hydrogen atoms in the IL. Such a spectrum is well documented for [C2mim][OAc] [266, 267], as shown in Figure 5.5.

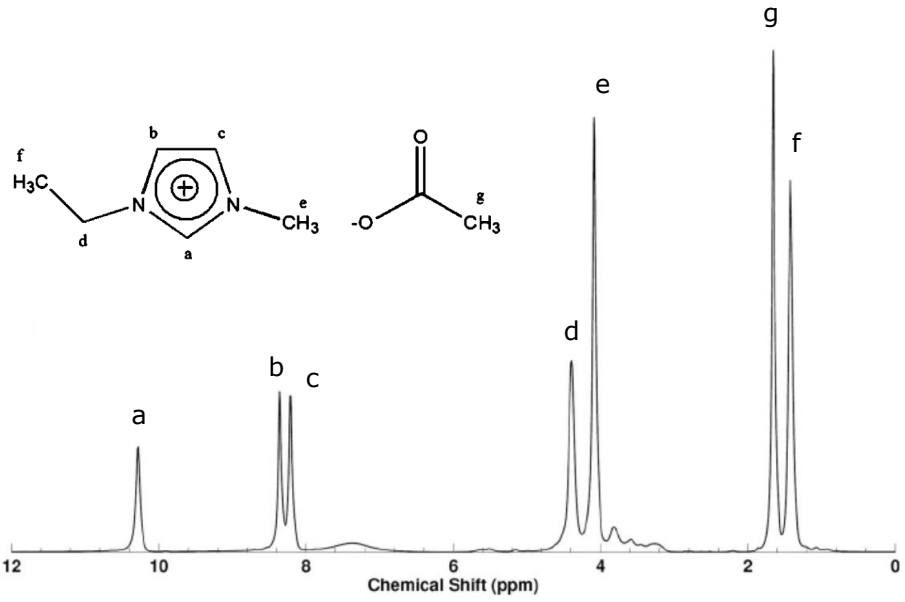

Figure 5.5: ^{1}H NMR spectrum of [C2mim][OAc] in glucose with inset showing the structure of [EMIM]+ and [Ac]- ions of the ionic liquid. Credit: D'Agostino et al. and Lovell et al. [268, 269]

Measuring Water Peak:

The hydrogen atoms within water molecules are also detectable on a ^{1}H NMR scan in the form of a single peak, the relative area of which can be used to determine the amount of water in the ionic liquid. Equation 5.1 provides an expression for the determination of solvent water content from a ^{1}H NMR scan.

$$Water\,Content = 100\left(\frac{18A_w}{2}\right)\left(\left(\frac{18A_w}{2}\right) + \left(\frac{170\sum_{n=1}^{7} A_n}{14}\right)\right)^{-1} \tag{5.1}$$

Where A_w is the area of the water peak and A_n is the area of the n'th ionic liquid peak. The pre-factors 18 and 170 correspond to the molecular weight of water and [C2mim][OAc] respectively, whereas the denominators 2 and 14 denote the number of hydrogen atoms in each substance.

Figure 5.6 shows NMR scans of [C2mim][OAc] after being left exposed to atmospheric moisture for various lengths of time. The water peak, seen fourth from the left, is seen to increase in size at time progresses. All peak locations are in good agreement with published data on the NMR spectra of [C2mim][OAc] [269].

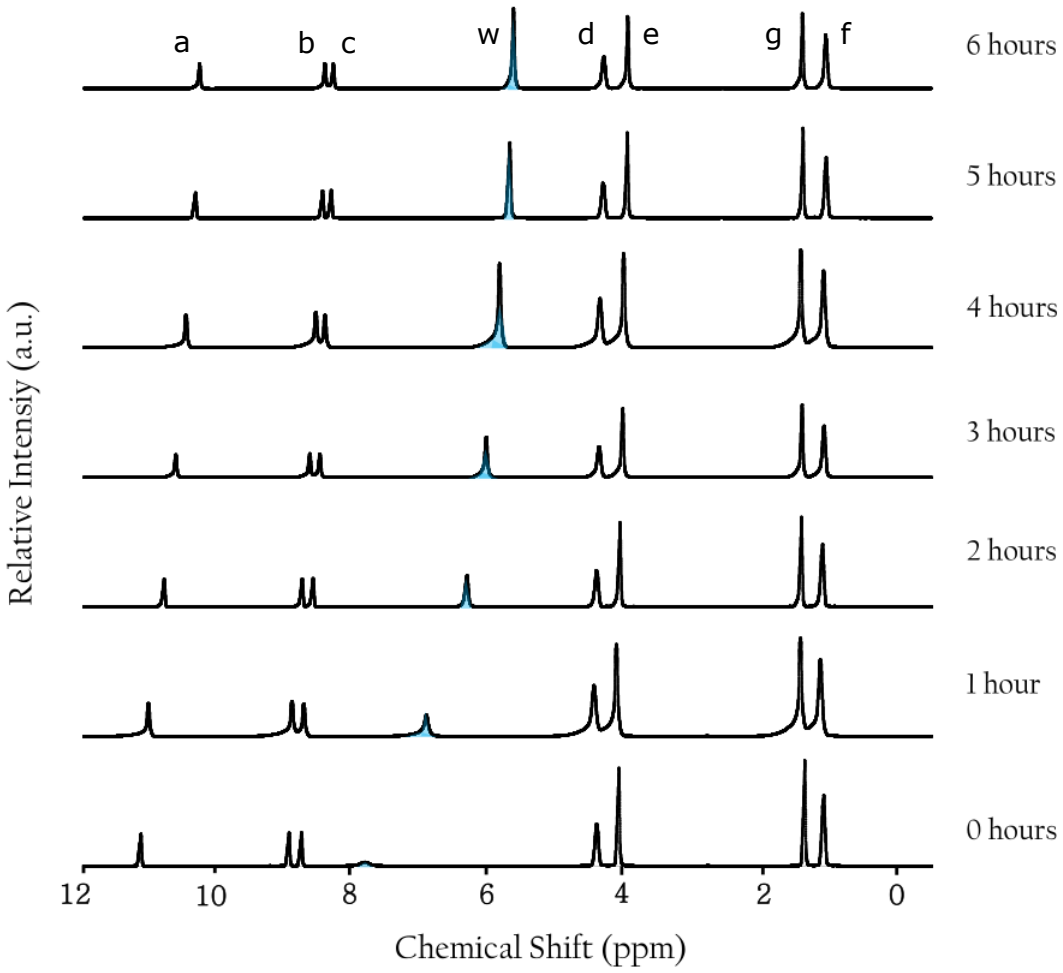

Figure 5.6: Magnetic resonance of protons within the ionic liquid/water system. Peaks *a*-*g* correspond to the H-atoms of the cation/anion (refer to Figure 5.5 for specifics), with the peak labelled '*w*' representing the H-atoms within water.

Equation 5.1 is used to determine the amount of water present in each scan featured in Figure 5.6. The results are shown in Figure 5.7. From this Figure, it is clear that dissolution cannot take place under atmospheric conditions if the water content is to be set and held at a constant value, nor can a vacuum be used- due to unwanted evaporation. For this reason, a nitrogen atmosphere was utilised during dissolution in a Leybold Sogevac vacuum oven.

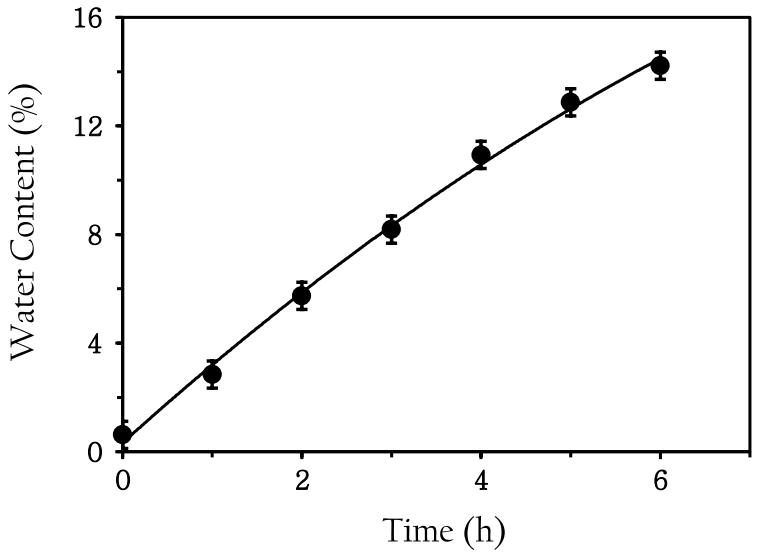

Figure 5.7: Uptake of atmospheric water by [C2mim][OAc] as a function of time under atmospheric conditions, with error bars representing the accuracy of the measuring apparatus (accurate to 0.5 %). Polynomial fit used to guide the eye.

From Figure 5.6, it is interesting to note that the IL from the bottle (i.e. '0 hours') displays a small water peak and is therefore not completely dry. This peak was found to correspond to 0.5 % water by weight. As the Bruker 400 MHz Avance II NMR spectrometer is only accurate to approx. 0.5 %, another experimental technique was utilised as a secondary method of water content determination. This complimentary method was chosen to be 'Karl Fischer Titration' (KFT), which was performed on a 'Metrohm 899 Coulometer'. Results from KFT showed the bottled IL to contain 0.53 % water - in close agreement with the NMR results.

Water was added to the solvent at the following concentrations: 2 %, 4 % and 8 % by weight. Once added, the mixture was mixed with a magnetic stirrer and left to preheat to the desired dissolution temperature.

All other experimental methods are identical to those outlined in section 2.1.

5.3 Results and Discussion

Figures 5.8, 5.9 and 5.10 display optical micrographs of yarns after various dissolution times at 60 °C. These figures correspond to yarns dissolved in solvent baths with water concentrations of 2 %, 4 % and 8 % respectively. For the 2 and 4 % systems, dissolution appears to occur in a similar fashion to that observed in the previous two chapters- with the formation and subsequent growth of a coagulated outer layer. In the system containing 8 % water however, no coagulated material is seen, even after 6 hours of dissolution.

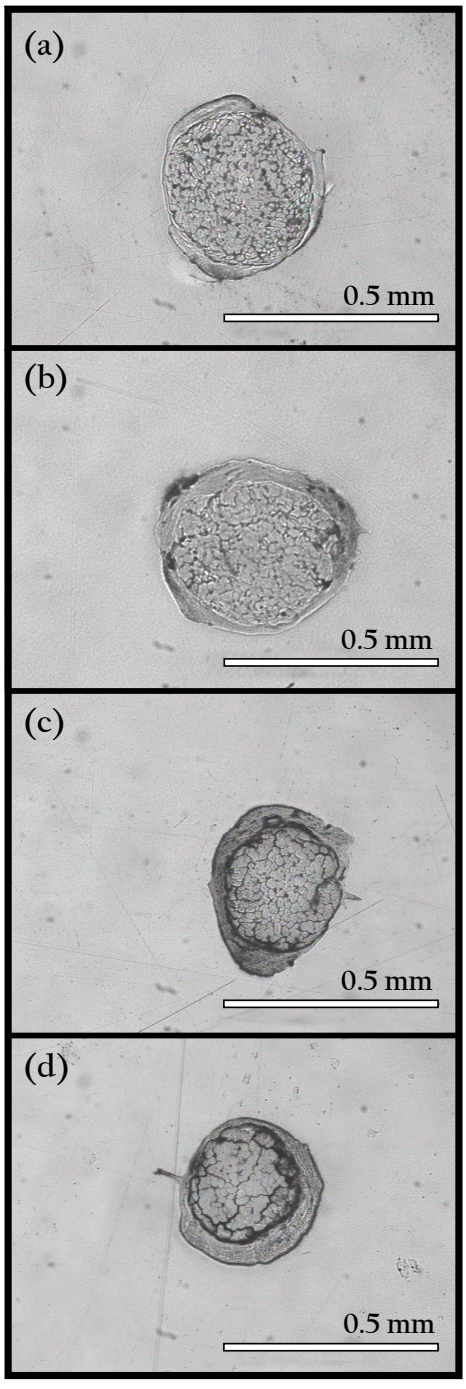

Figure 5.8: Cross sections of yarns processed at 60 ℃ for 0.5 hours (a), 1 hour (b), 1.5 hours (c) and 2 hours (d) when using a water concentration of 2 %.

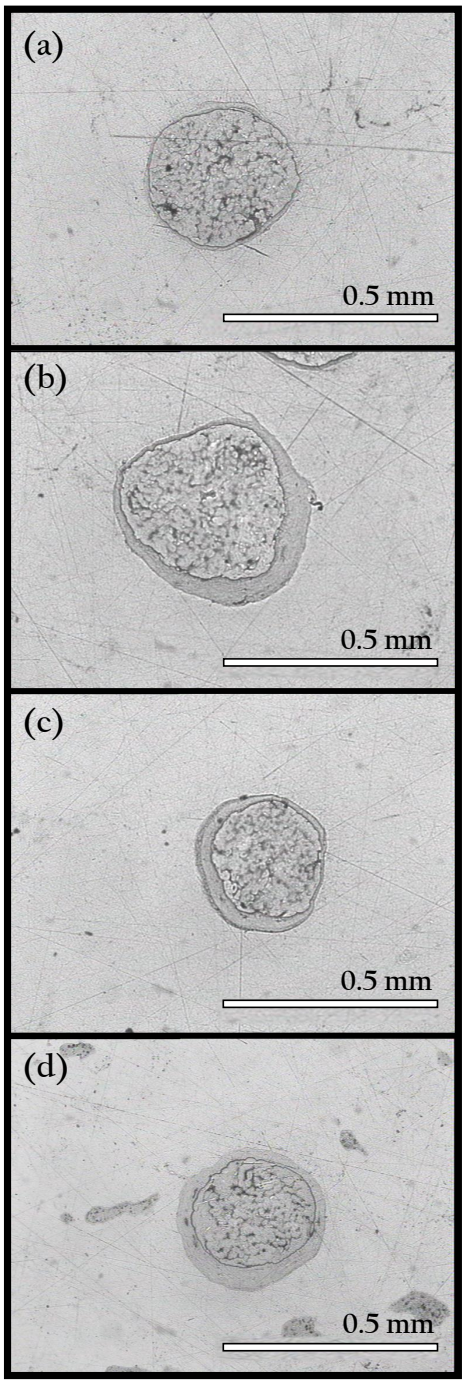

Figure 5.9: Cross sections of yarns processed at 60 °C for 2 hours (a), 4 hours (b), 6 hours (c) and 8 hours (d) when using a water concentration of 4 %.

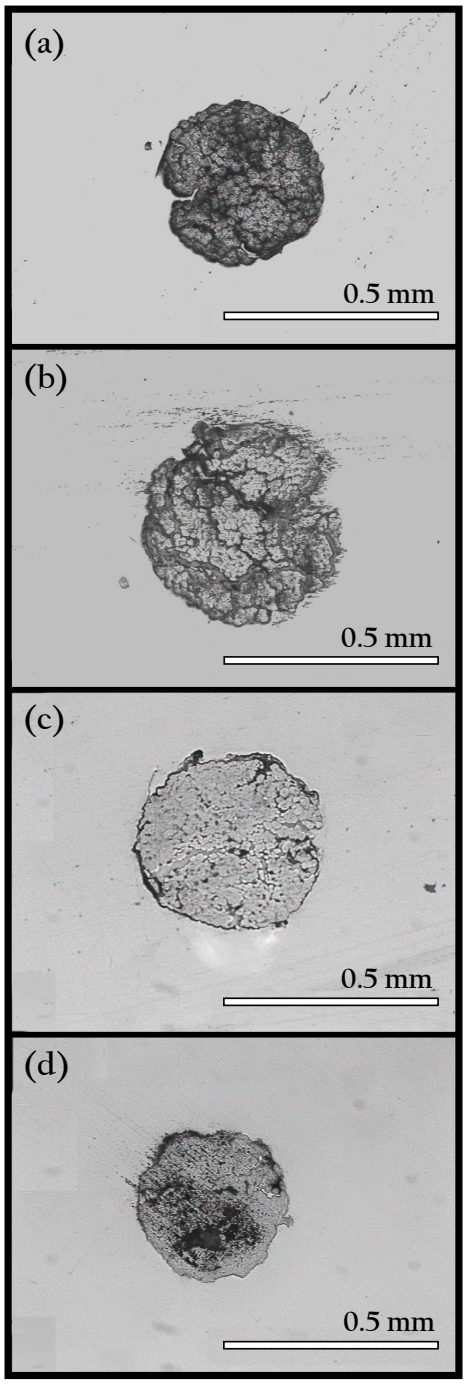

Figure 5.10: Cross sections of yarns processed at 60 °C for 1.5 hours (a), 3 hours (b), 4.5 hours (c) and 6 hours (d) when using a water concentration of 8 %.

As no discernible dissolution was seen to occur in the system containing 8 % water, this system was analysed no further. For the 2 and 4 % systems however, the coagulation fraction (CF) was plot as a function of both time and temperature, as seen in Figures 5.11 and 5.12. Within these figures, the CF data is first expressed in linear time, before being shifted in natural logarithmic time to form a master curve. The shift factors used to create this master curve are then plot against their respective dissolution temperatures to reveal a linear relation and thus, an activation energy. A detailed explanation of this procedure can be found in Chapter 3 section 3.3.1.

The activation energies of dissolution in the 2 and 4 % water systems were found to be 95 ± 5 kJ/mol and 109 ± 10 kJ/mol respectively. Both of these energies are within error of the activation energies determined in the previous chapters. Figure 5.13 highlights the consistency of the activation energy as a function of solvent water content.

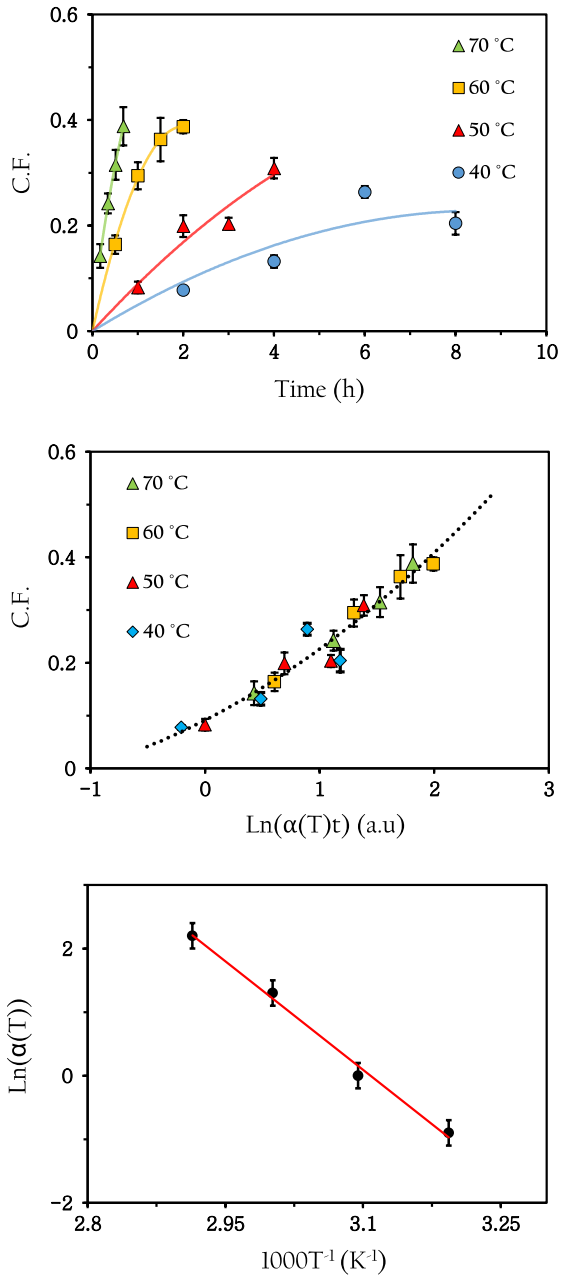

Figure 5.11: Data corresponding to the CF as a function of temperature (top), the shifted data expressed in ln time as a master curve (middle) and corresponding Arrhenius plot (bottom) when using 2 % water by weight. Polynomial fits used to guide the eye in top and middle plots, with a linear fit to the data in the bottom plot. Error bars used in all plots, though may be smaller than data points.

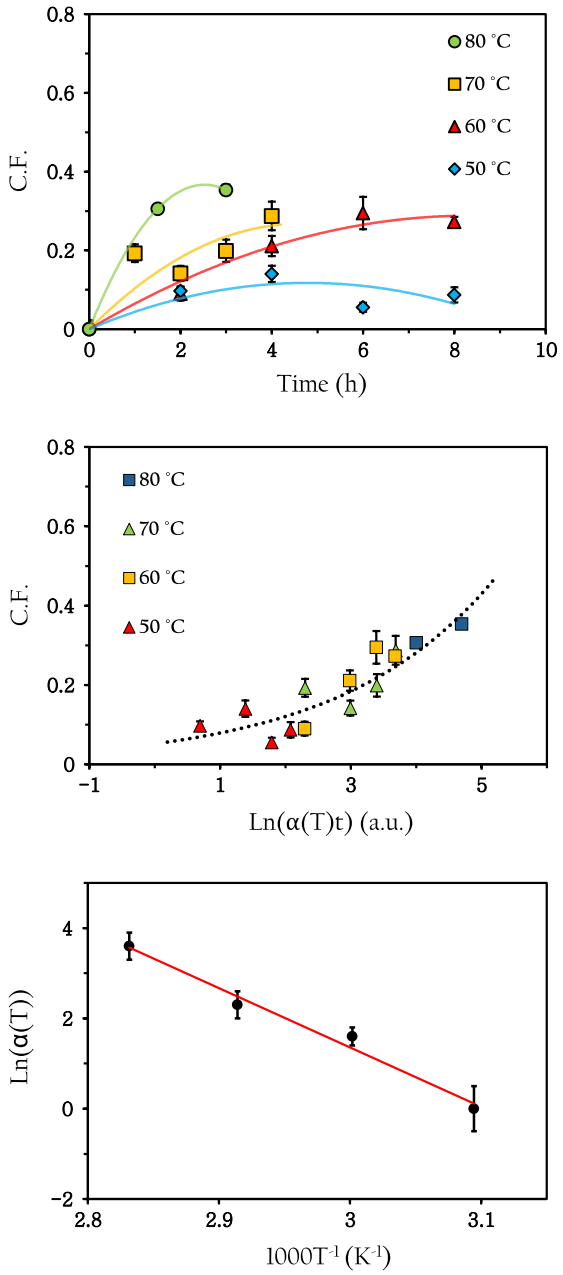

Figure 5.12: Data corresponding to the CF as a function of temperature (top), the shifted data expressed in ln time as a master curve (middle) and corresponding Arrhenius plot (bottom) when using 4 % water by weight. Polynomial fits used to guide the eye in top and middle plots, with a linear fit to the data in the bottom plot. Error bars used in all plots, though may be smaller than data points.

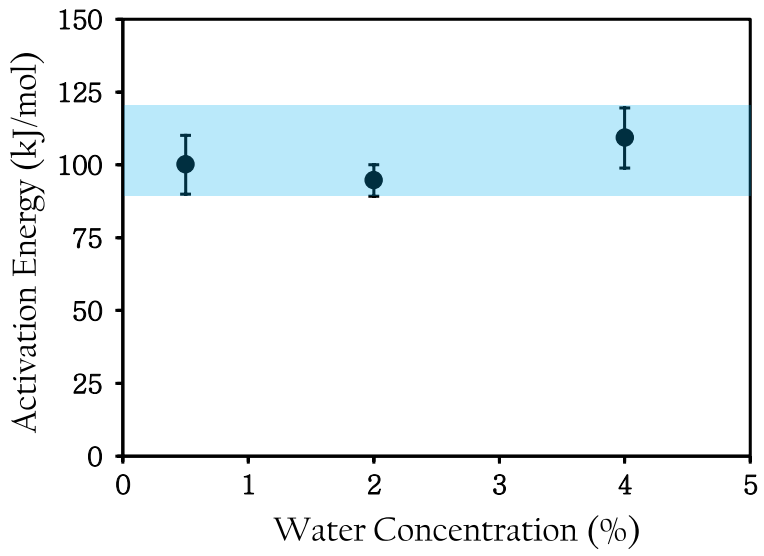

Figure 5.13: Activation energy required for dissolution as a function of H_2O concentration. Shaded area used to highlight the consistency of values.

The master curves generated for the 2 and 4 % water systems were next shifted in natural logarithmic time so as to overlap with the master curve seen prior in section 3.3.1, corresponding to the bottled IL (featuring 0.5 % water). The resultant curve including all systems is seen in Figure 5.14. The amounts by which each individual master curve had to be shifted (in order to overlap) provided a direct measure of the relative dissolution rates between systems. Figure 5.15 reveals that the dissolution rate decreases exponentially in accordance with increasing H_2O concentration within the solvent bath. Within Figure 5.15, error bars are determined by the error in the shifting of each data set to form the master curve (seen in Figure 5.14).

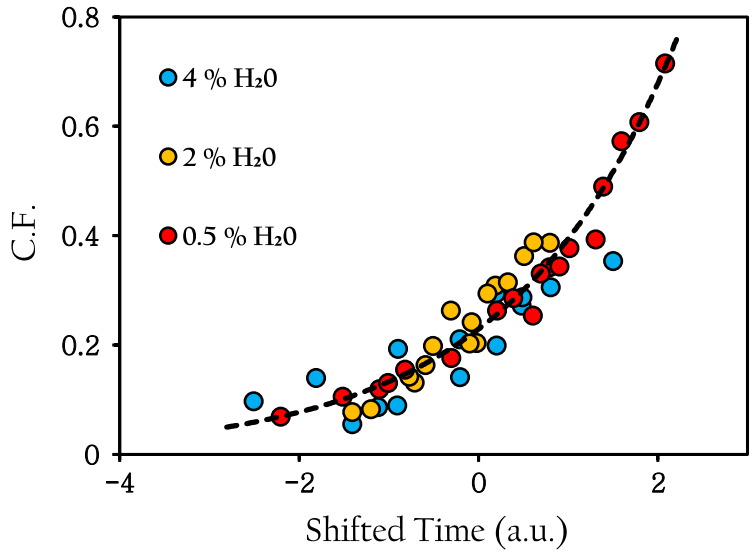

Figure 5.14: Master curve showing the coagulation fraction across all temperatures and all H_2O concentrations. Each data set uses 50 °C as the reference temperature. An exponential fit is used to guide the eye.

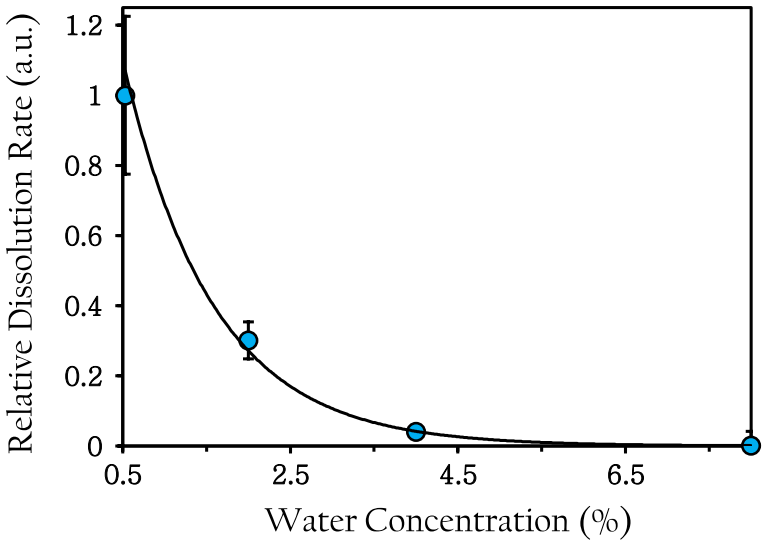

Figure 5.15: Relative dissolution rate of flax yarns as a function of solvent water content. Exponential decay fitted to data as a guide for the eye. Some error bars may be smaller than data points.

The natural logarithm of the data points presented in Figure 5.15 were next plot as a function of solvent water content. The resulting linear trend highlights the exponentially decaying nature of the dissolution rate as a function of H_2O concentration.

Rabideau et al. recently published results from simulations revealing the interactions between several ionic liquids, cellulose and water [270]. It was shown that anions can form up to four hydrogen bonds with cellulose and that the length of time spent bound is a function of the number of established bonds. With the introduction of water, a significant disruption in the frequency of h-bonds between anion and cellulose was observed. This was due to H_2O molecules crowding the h-bond accepting sites of the anion- preventing interactions with cellulose. They showed that the more water present, the more crowded these sites become. Thus, if a hydrogen bond between an anion and cellulose were to break, the likelihood of it being immediately replaced by a nearby water molecule increases accordingly. For a new hydrogen bond to form between the anion and cellulose, it was shown that an obstructing water molecule must first detach from the anion to make way for this new bond. They conclude by stating that "the presence of water leads to steep drops in hydrogen bonding between anions and cellulose" - this steep drop in bonding due to the crowding of anion h-bond sites may explain the exponential decline in the dissolution rate observed in Figure 5.15. Gupta et al. also report a similar decrease in anion-cellulose bonds as a function of water concentration in the context of cellulosic regeneration [123].

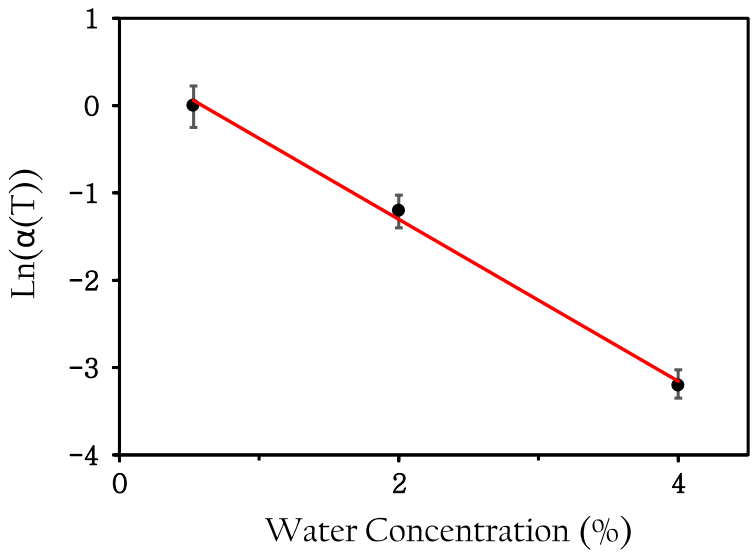

Figure 5.16: Data from Figure 5.15 expressed in natural logarithmic space, with the linear trend highlighting the exponentially decaying nature of the dissolution rate.

5.4 Conclusions

The dissolution rate and mechanism of flax yarns in the ionic liquid [C2mim][OAc] has been documented as a function of solvent water content and temperature. Optical microscopy has been used to view the cross sections of partially dissolved yarns, whereby a coagulated outer layer was seen to grow in accordance with dissolution time and temperature.

Three different H_2O concentrations have been used; 2 %, 4 % and 8 % by weight. Results from chapter 3 have also been recalled for the sake of comparison to the bottled IL (found to consist of 0.5 % water). For the systems involving 2 % and 4 % water, the coagulated outer layer was seen to form around the undissolved core as expected. The system involving 8 % water however, showed no signs of dissolution- implying that a solvent moisture content as little as 8 %

by weight is sufficient to halt the dissolution process on experimental time-scales.

As with the data in Chapters 3 and 4, the CF curves have been shifted in natural logarithmic time to form master curves. This procedure was repeated for each H_2O concentration used (aside from 8 %, whereby no coagulated material was evident). These master curves provided evidence of time-temperature superposition in the system when using both 2 % and 4 % water. The shift factors used to generate each master curve were next plot against the inverse of their respective dissolution temperatures to reveal Arrhenious behaviour in both cases. The resulting activation energies were found to be 95 $\pm$ 5 kJ/mol and 109 $\pm$ 10 kJ/mol for the systems containing 2 % and 4 % water respectively. These values are within error of the activation energies attained in Chapters 3 and 4 when using bottled IL containing 0.5 % water.

Master curves corresponding to the 2 and 4 % water systems were subsequently shifted in natural logarithmic time to overlap with that of the pure IL master curve (seen previously in Chapter 3). The shift factors used to create the resulting curve gave a direct measure of the relative dissolution rate between systems. Interestingly, the rate of dissolution was found to decrease exponentially in accordance with moisture content of the solvent. It is postulated that this exponential decline in dissolution rate is strongly related to the crowding of anion h-bond sites by H_2O molecules, diminishing interactions between solvent and solute.

Chapter 6

Conclusion and Outcomes

6.1 Research Outcomes

This thesis has set out to explore the dissolution behaviour of flax based yarns in the ionic liquid [C2mim][OAc]. Yarns have been submerged in the solvent for various lengths of time at a range of dissolution temperatures before being coagulated in water and analysed. The effect of the co-solvent dimethyl-sulfoxide (DMSO) and the anti-solvent H_2O have also been studied in conjunction with the primary solvent.

Dissolution in pure [C2mim][OAc]

When using pure [C2mim][OAc] as the solvent, three key methods of analysis were used to examine the resulting yarns: optical microscopy, X-ray diffraction and mechanical testing- with each method allowing for a distinct means of studying the dissolution behaviour.

Optical microscopy provided cross-sectional images of both raw and partially dissolved yarn. Within these images, the constituent sub-fibres were visible and a notably different outer layer was seen to form around the core as dissolution progressed. The magnitude of this outer layer (referred to as the 'coagulation fraction (CF)') was measured as a function of both dissolution time and temperature- which were subsequently found to be interchangeable. When each (temperature dependant) data set was scaled in the natural logarithmic time domain, a mas-

ter curve was formed. The shift factors used to create this curve were next plot against the inverse of their respective dissolution temperatures to reveal Arrhenius behaviour in the system. The Arrhenious equation was then used to determine an activation energy of 100 ± 10 kJ/mol; similar to values quoted in the literature when discussing cellulosic dissolution [145, 148, 206, 207].

Both digital and analogue X-ray diffraction have also been used to examine the dissolution behaviour. Digital X-ray diffraction provided a means of tracking the relative reduction in the cellulose I content, which proved to be a reliable marker of dissolution due to the irreversibility of the transition from cellulose I to cellulose II. The raw yarn was found to contain 53 % cellulose I, with the rest being amorphous material. As with the data attained from optical microscopy, the CF from digital X-ray data has also been shifted in the ln time domain to form a master curve. Arrhenius behaviour was revealed in relation to the growth of the coagulated fraction and a subsequent activation energy of 87 ± 16 kJ/mol was determined.

X-ray sensitive films were used to capture two dimensional diffraction patterns of the raw, partially and fully dissolved yarns. Bragg peaks associated with the cellulose I and II crystal structures were visible, with a bright ring representing the amorphous component. These films showed only cellulose I and amorphous material in the raw yarn, a mix of Cellulose I, II and amorphous in the partially dissolved yarn and only cellulose II and amorphous in the fully dissolved yarn.

Finally, mechanical testing revealed two more independent measures of the activation energy via measurements of the yarn's strength and modulus. These values were again derived via the creation of master curves and associated Arrhenius plots. The energies determined were 102 ± 17 kJ/mol and 107 ± 10 kJ/mol when analysing the strength and modulus data respectively. The raw yarn was found to have a strength of 398 ± 22 MPa and a modulus of 18.7 ± 1.7 GPa, in good agreement with published works [208, 199]. Interestingly, a 'pre-forming' phase was evident at low coagulation fractions, whereby the modulus and strength were seen to (counter-intuitively) increase in accordance with dissolution. This increasing trend was attributed to the gradual binding together of sub-fibres via the network of coagulated material; promoting superior load bearing capacities

as a result. As dissolution progressed further however, the favourable balance between fibrous cores and coagulated matrix was lost and both the strength and modulus were seen to drop as expected.

The activation energies resulting from each method of analysis as outlined above showed a high degree of consistency, with an average value of 99 ± 13 kJ/mol. This energy is assumed to relate to the de-construction of the fundamental bonds holding together the cellulose I crystal lattice, though the exact nature of the activation energy on a molecular level remains unclear.

Effect of the Co-Solvent Dimethyl-Sulfoxide

Next, the co-solvent dimethyl-sulfoxide was added to the [C2mim][OAc] at various concentrations, which noticeably altered the viscosity of the solvent bath. Analysis was performed using optical microscopy, whereby yarns were seen to dissolve in a similar manner to those dissolved in the pure [C2mim][OAc] system: a coagulated outer layer was again seen to form and increase in size in accordance with dissolution time and temperature. The rate of dissolution was, however, drastically altered at all co-solvent concentrations, reaching a maximum dissolution rate when using equal amounts ionic liquid to DMSO. Time-temperature equivalence was observed in all systems and activation energies were found to be within error of those determined previously (when using [C2mim][OAc] alone). These energies were determined to be 100 ± 11 kJ/mol, 91 ± 5 kJ/mol and 102 ± 3 kJ/mol for co-solvent concentrations of 20 %, 50 % and 75 % respectively. This finding proved interesting, as it suggested that the role of the co-solvent is not to reduce the activation energy of dissolution, rather, its function may be more closely related with providing solvent molecules more attempts per unit time to infiltrate the cellulose h-bond network. Lastly, it was suggested that the poor solvating capacities at high co-solvent concentrations is in part due to the tendency of the anion to bind with DMSO molecules (a phenomena documented in the literature [227]) as such bonding may prevent cellulose-anion interactions.

Influence of H_2O on the system

The aim of the final chapter has been to study the effects of water on the system by adding small amounts of distilled H_2O to the solvent bath. The [C2mim][OAc] used throughout this work was found to contain 0.5 % water, as determined via nuclear magnetic resonance and Karl Fischer titration. Optical microscopy was again the method of choice for tracking the growth of the coagulation fraction and surprisingly; as little as 8 % water by weight was proven sufficient to halt the dissolution process on experimental time-scales. For the systems involving both 2 % and 4 % water however, time-temperature superposition was again evident. This finding gave rise to master curves and Arrhenius plots, with corresponding activation energies of 95 ± 5 kJ/mol (2 % H_2O) and 109 ± 10 kJ/mol (4 % H_2O). The rate of dissolution was found to decrease exponentially in accordance with H_2O concentration. This exponential decline is thought to relate to the crowding of anion h-bond sites with water molecules- preventing interactions between the ionic liquid and cellulose hydroxyl groups.

6.2 Overarching Findings

The work presented in this thesis has identified an activation energy associated with the dissolution of flax based yarns in the ionic liquid [C2mim][OAc]. This energy is found to be to be remarkably consistent - existing within error of 100 kJ/mol no matter the measurement method (Optical microscopy/X-ray diffraction/mechanical testing), concentration of co-solvent (Dimethyl-sulfoxide) or anti-solvent (H_2O). Dimethyl-sulfoxide is shown to drastically alter the rate of dissolution, reaching a maximum when using equal amounts solvent to co-solvent, whereas H_2O is found to decrease this rate exponentially.

6.3 Future Directions

With the determination of a seemingly constant activation energy across all systems, the following questions naturally arise: Is this energy related solely to the structure of cellulose, or can it be modified with specific solvents, co-solvents or alternative dissolution procedures- such as microwave heating? Does the source of

cellulose, its molecular weight or crystallinity effect the activation energy? Is the equivalence between time and temperature valid across a broader experimental window and does the dissolution of cellulose powder/nano-particles etc. result in a similar activation energy to that of yarns? One could also experiment with other natural yarns such as silk, cotton or hemp and compare the resulting dissolution mechanisms/rates/energies to that of flax.

This work may also be of value to future researchers making all-cellulose composites, either in a batch process or a continuous commercial process- as this study has shown how the dissolution time may be decreased (using temperature or co-solvent concentration), how the fraction of expensive ionic liquid may be reduced (using DMSO) and how to accurately measure the coagulated material in order to attain an optimum composite matrix fraction (using optical microscopy, X-ray diffraction or mechanical testing.)

Notes and references

[1] Ludwik Szcześniak, Adam Rachocki, and Jadwiga Tritt-Goc. Glass transition temperature and thermal decomposition of cellulose powder. *Cellulose*, 15(3):445–451, 2008. 1, 7, 118

[2] David N.S. Hon. Cellulose: a random walk along its historical path. *Cellulose*, 1994. 1

[3] Haregewine Tadesse and Rafael Luque. Advances on biomass pretreatment using ionic liquids: An overview. *Energy and Environmental Science*, 4(10):3913–3929, 2011. 1

[4] Shannon M Notley, Bert Pettersson, and Lars Wa. Direct Measurement of Attractive van der Waals ' Forces between Regenerated Cellulose Surfaces in an Aqueous Environment. pages 13930–13931, 2004. 1

[5] Susan K. Cousins and R. Malcolm Brown. Cellulose I microfibril assembly: computational molecular mechanics energy analysis favours bonding by van der Waals forces as the initial step in crystallization. *Polymer*, 36(20):3885–3888, 1995. 1, 2

[6] Terry L. Bluhm and Anatole Sarko. Packing analysis of carbohydrates and polysaccharides. V. Crystal structures of two polymorphs of pachyman triacetate. *Biopolymers*, 16(9):2067–2089, 1977. 1, 4, 19

[7] M. J.A. van den Oever, H. L. Bos, and M. J.J.M. van Kemenade. Influence of the physical structure of flax fibres on the mechanical properties of flax fibre reinforced polypropylene composites. *Applied Composite Materials*, 7(5-6):387–402, 2000. 1

[8] Xiao Wei, Wei Wei, Yu Hu Cui, Ting Ju Lu, Man Jiang, Zuo Wan Zhou, and Yong Wang. All-cellulose composites with ultra-high mechanical properties prepared through using straw cellulose fiber. *RSC Advances*, 6(96):93428–93435, 2016. 1

[9] Sara Samiee, Hossein Ahmadzadeh, Majid Hosseini, and Stephen Lyon. *Algae as a Source of Microcrystalline Cellulose*. Elsevier Inc., 2019. 1

[10] Johnsy George and S. N. Sabapathi. Cellulose nanocrystals: Synthesis, functional properties, and applications. *Nanotechnology, Science and Applications*, 8:45–54, 2015. 1

[11] A. Parisot and J. Cyrot. The degree of polymerisation of cellulose. *Journal of the Textile Institute Proceedings*, 42(8):P783–P797, 1951. 1

[12] Mitchell S. Sweet and Jerrold E. Winandy. Influence of degree of polymerization of cellulose and hemicellulose on strength loss in fire-retardant-treated southern pine. *Holzforschung*, 53(3):311–317, 1999. 1

[13] Alfred D. French. Glucose, not cellobiose, is the repeating unit of cellulose and why that is important. *Cellulose*, 24(11):4605–4609, 2017. xi, 2

[14] Yanliang Gu, Tapas Kar, and Steve Scheiner. Fundamental properties of the CH ··· O interaction: Is it a true hydrogen bond? *Journal of the American Chemical Society*, 121(40):9411–9422, 1999. 2

[15] A. M. Bochek. Effect of hydrogen bonding on cellulose solubility in aqueous and nonaqueous solvents. *Russian Journal of Applied Chemistry*, 76(11):1711–1719, 2003. 2, 7, 65, 116

[16] Wilson Pires and Flauzino Neto. Morphological investigation of cellulose nanocrystals and nanocomposite applications. (January), 2017. xi, 2

[17] John Blackwell, David Kurz, Mao-Yao Su, and David M. Lee. X-ray Studies of the Structure of Cellulose Complexes. pages 199–213, 1987. xi, 3, 4

[18] Ray Horne, M.R.L. & Waldron, D. & Harwood, J.L. & Harwood. The Production and Extraction of Flax-Fibre for Textile Fibres. *Journal of Biobased Materials and Bioenergy.*, (4):98–105, 2010. xi, 3, 6

[19] Eric S. Gardiner and Anatole Sarko. Packing analysis of carbohydrates and polysaccharides. 16. The crystal structures of celluloses IV I and IV II . *Canadian Journal of Chemistry*, 63(1):173–180, 1985. 4

[20] Serge Pérez and Daniel Samain. Structure and Engineering of Celluloses. *Advances in Carbohydrate Chemistry and Biochemistry*, 64(C):25–116, 2010. 4, 19

[21] Kabindra Kafle, Kenneth Greeson, Christopher Lee, and Seong H. Kim. Cellulose polymorphs and physical properties of cotton fabrics processed with commercial textile mills for mercerization and liquid ammonia treatments. *Textile Research Journal*, 84(16):1692–1699, 2014. 4

[22] Jurgen Lange Bregado, Argimiro Resende Secchi, Frederico Wanderley Tavares, Dasciana de Sousa Rodrigues, and Rossano Gambetta. Amorphous paracrystalline structures from native crystalline cellulose: A molecular dynamics protocol. *Fluid Phase Equilibria*, 491:56–76, 2019. 4

[23] P. M. Visakh and Sabu Thomas. Preparation of bionanomaterials and their polymer nanocomposites from waste and biomass. *Waste and Biomass Valorization*, 1(1):121–134, 2010. 4

[24] Wilson Pires and Flauzino Neto. Etude morphologique des nanocristaux de cellulose et application nanocomposites. (January), 2017. xi, 5

[25] Hitomi Miyamoto, Udo Schnupf, and John W. Brady. Water structuring over the hydrophobic surface of cellulose. *Journal of Agricultural and Food Chemistry*, 62(46):11017–11023, 2014. 6, 116

[26] Saija Väisänen, Raili Pönni, Anna Hämäläinen, and Tapani Vuorinen. Quantification of accessible hydroxyl groups in cellulosic pulps by dynamic vapor sorption with deuterium exchange. *Cellulose*, 25(12):6923–6934, 2018. 6

[27] Chihiro Yamane, Takeshi Aoyagi, Mariko Ago, Kazuishi Sato, Kunihiko Okajima, and Toshisada Takahashi. Two different surface properties of regenerated cellulose due to structural anisotropy. *Polymer Journal*, 38(8):819–826, 2006. xi, 6, 19

[28] Marta Preisner, Wioleta Wojtasik, Anna Kulma, Magdalena Żuk, and Jan Szopa. *Flax Fiber*. Number September. 2014. 6

[29] Sullivan Renouard, Christophe Hano, Pierre Ouagne, Jean Philippe Blondeau, and Eric Lainé. Protection of flax fiber-based yarns against natural soil degradation by chitosan. *Materials Letters*, 137:269–273, 2014. 6

[30] Bapan Adak and Samrat Mukhopadhyay. Jute based all-cellulose composite laminates. *Indian Journal of Fibre and Textile Research*, 41(4):380–384, 2016. 7, 23

[31] A. K. Bledzki, A. A. Mamun, M. Lucka-Gabor, and V. S. Gutowski. The effects of acetylation on properties of flax fibre and its polypropylene composites. *Express Polymer Letters*, 2(6):413–422, 2008. 7

[32] Jochen Gassan and Andrzej K. Bledzki. Thermal degradation of flax and jute fibers. *Journal of Applied Polymer Science*, 82(6):1417–1422, 2001. 7

[33] Mark Hughes. Defects in natural fibres: Their origin, characteristics and implications for natural fibre-reinforced composites. *Journal of Materials Science*, 47(2):599–609, 2012. 7

[34] K. Charlet, S. Eve, J. P. Jernot, M. Gomina, and J. Breard. Tensile deformation of a flax fiber. *Procedia Engineering*, 1(1):233–236, 2009. 7

[35] David L. Minnick, Raul A. Flores, Matthew R. Destefano, and Aaron M. Scurto. Cellulose Solubility in Ionic Liquid Mixtures: Temperature, Cosolvent, and Antisolvent Effects. *Journal of Physical Chemistry B*, 120(32):7906–7919, 2016. 7

[36] Sania Naz, Naveed Ahmad, Javeed Akhtar, Nasir Mehmood Ahmad, Attarad Ali, and Muhammad Zia. Management of citrus waste by switching in the production of nanocellulose. *IET Nanobiotechnology*, 10(6):395–399, 2016. 7

[37] Hyung Min Cho, Adam S. Gross, and Jhih Wei Chu. Dissecting force interactions in cellulose deconstruction reveals the required solvent versatility for overcoming biomass recalcitrance. *Journal of the American Chemical Society*, 133(35):14033–14041, 2011. xi, 7, 8, 9

[38] Aya Zoghlami and Gabriel Paës. Lignocellulosic Biomass: Understanding Recalcitrance and Predicting Hydrolysis. *Frontiers in Chemistry*, 7(December), 2019. 7

[39] Thomas Auxenfans, Christine Terryn, and Gabriel Paës. Seeing biomass recalcitrance through fluorescence. *Scientific Reports*, 7(1):1–8, 2017. 7

[40] Chunxia Chen, Chao Duan, Jianguo Li, Yishan Liu, Xiaojuan Ma, Linqiang Zheng, Jaroslav Stavik, and Yonghao Ni. Cellulose (dissolving pulp) manufacturing processes and properties: A mini-review. *BioResources*, 11(2):5553–5564, 2016. 7, 15

[41] M. Mat Salleh, K. Magniez, S. Pang, J. W. Dormanns, and M. P. Staiger. Parametric optimization of the processing of all-cellulose composite laminae. *Advanced Manufacturing: Polymer and Composites Science*, 3(2):73–79, 2017. 7

[42] A. Das. Thermal degradation of cellulosic fibres. 60(4):343–349, 1981. 7

[43] James A. Schlademan. Melting points. *Adhesives Age*, 45(10):22–25, 2002. 7

[44] Björn Lindman, Bruno Medronho, Luis Alves, Carolina Costa, Håkan Edlund, and Magnus Norgren. The relevance of structural features of cellulose and its interactions to dissolution, regeneration, gelation and plasticization phenomena. *Physical Chemistry Chemical Physics*, 19(35):23704–23718, 2017. 7

[45] N. Mohd, S. F.S. Draman, M. S.N. Salleh, and N. B. Yusof. Dissolution of cellulose in ionic liquid: A review. *AIP Conference Proceedings*, 1809, 2017. 7

[46] Tim Huber, Jörg Müssig, Owen Curnow, Shusheng Pang, Simon Bickerton, and Mark P. Staiger. A critical review of all-cellulose composites. *Journal of Materials Science*, 47(3):1171–1186, 2012. 7, 16, 24

[47] Yakov M. Tseytlin. AFM with Higher Mode Oscillations and Higher Sensitivity. *Advanced Mechanical Models of DNA Elasticity*, pages 101–155, 2016. 7

[48] Carl J. Malm and Leo J. Tanghe. Chemical Reactions in the Making of Cellulose Acetate. *Industrial & Engineering Chemistry*, 47(5):995–999, 1955. 8

[49] Dieter Klemm, Brigitte Heublein, Hans Peter Fink, and Andreas Bohn. Cellulose: Fascinating biopolymer and sustainable raw material. *Angewandte Chemie - International Edition*, 44(22):3358–3393, 2005. 8

[50] Tasnim Shaikh, Satyajeet Chaudhari, and Alpa Varma. Viscose Rayon: A Legendary Development in the Manmade Textile. *Mrs. Alpa Varma / International Journal of Engineering Research and Applications (IJERA)*, 2(5):675–680, 2012. 8

[51] Mohammad Ghasemi, Marina Tsianou, and Paschalis Alexandridis. Assessment of solvents for cellulose dissolution. *Bioresource Technology*, 228:330–338, 2017. 8

[52] Guansen Jiang, Weifeng Huang, Baochun Wang, Yumei Zhang, and Huaping Wang. The changes of crystalline structure of cellulose during dissolution in 1-butyl-3-methylimidazolium chloride. *Cellulose*, 19(3):679–685, 2012. 8

[53] Xingya Kang, Shigenori Kuga, Limei Wang, Min Wu, and Yong Huang. Dissociation of intra / inter-molecular hydrogen bonds of cellulose molecules in the dissolution process : a mini review. *Journal of Bioresources and Bioproducts.*, 1(1):58–63, 2016. 8

[54] Pan Chen, Yoshiharu Nishiyama, Jean-luc Putaux, and Karim Mazeau. Diversity of potential hydrogen bonds in cellulose I revealed by molecular dynamics simulation Diversity of potential hydrogen bonds in cellulose I revealed by molecular dynamics simulation. (April), 2014. 8

[55] D. Gagnaire, D. Mancier, and M. Vincendon. Cellulose organic solutions: a nuclear magnetic resonance investigation. 18:13–25, 1980. 8

[56] Lisa Axelsson, Maria Franzén, Madelene Ostwald, Göran Berndes, G. Lakshmi, and N. H. Ravindranath. Perspective: Jatropha cultivation in south-

ern India: Assessing farmers' experiences. *Biofuels, Bioproducts and Biorefining*, 6(3):246–256, 2012. 8

[57] A. Padayachee, L. Day, K. Howell, and M. J. Gidley. Complexity and health functionality of plant cell wall fibers from fruits and vegetables. *Critical Reviews in Food Science and Nutrition*, 57(1):59–81, 2017. 8

[58] Thomas Auxenfans, David Crônier, Brigitte Chabbert, and Gabriel Paës. Understanding the structural and chemical changes of plant biomass following steam explosion pretreatment. *Biotechnology for Biofuels*, 10(1):1–16, 2017. 9

[59] P. Alvira, E. Tomás-Pejó, M. Ballesteros, and M. J. Negro. Pretreatment technologies for an efficient bioethanol production process based on enzymatic hydrolysis: A review. *Bioresource Technology*, 101(13):4851–4861, 2010. 9

[60] Nicolas Le Moigne, M Nicolas Le Moigne, M Jürgen Puls, and M Christoph Schrempf. Swelling and dissolution mechanisms of cellulose fibres. 2009. 10

[61] Beth A. Miller-Chou and Jack L. Koenig. A review of polymer dissolution. *Progress in Polymer Science (Oxford)*, 28(8):1223–1270, 2003. 10, 16

[62] N. Le Moigne and P. Navard. On the specific behaviour of native cellulose fibers upon dissolution. *ACS Symposium Series*, 1033:137–148, 2010. xii, 10

[63] J. S. Vrentas and C. M. Vrentas. Dissolution of rubbery and glassy polymers. *Journal of Polymer Science, Part B: Polymer Physics*, 36(14):2607–2614, 1998. 10

[64] Verne W. Tripp and Mary L. Rollins. Morphology and Chemical Composition of Certain Components of Cotton Fiber Cell Wall. *Analytical Chemistry*, 24(11):1721–1728, 1952. 10

[65] Charles W. Hock. Degradation of Cellulose as Revealed Microscopically. *Textile Research Journal*, 20(3):141–151, 1950. 10

[66] Céline Cuissinat and Patrick Navard. Swelling and dissolution of cellulose, Part III: Plant fibres in aqueous systems. *Cellulose*, 15(1):67–74, 2008. 11

[67] A. Isogai and R. H. Atalla. Dissolution of cellulose in aqueous NaOH solutions. *Cellulose*, 5(4):309–319, 1998. 11

[68] Santiago Fajardo, García-Galvan, Federico R., Violeta Barranco, Juan C. Galvan, and Sebastian Feliu Batlle. From Cellulose Dissolution and Regeneration to Added Value Applications — Synergism Between Molecular Understanding and Material Development. *Intech*, i(tourism):13, 2016. xii, 11

[69] Lina Zhang, Dong Ruan, and Shanjun Gao. Dissolution and regeneration of cellulose in NaOH/Thiourea aqueous solution. *Journal of Polymer Science, Part B: Polymer Physics*, 40(14):1521–1529, 2002. 11

[70] Björn Lindman, Gunnar Karlström, and Lars Stigsson. On the mechanism of dissolution of cellulose. *Journal of Molecular Liquids*, 156(1):76–81, 2010. 11, 65, 118

[71] Ali Khodayari, Aart W. Van Vuure, Ulrich Hirn, and David Seveno. Tensile behaviour of dislocated/crystalline cellulose fibrils at the nano scale. *Carbohydrate Polymers*, 235(October 2019):115946, 2020. 12

[72] Spyridon Varlas, Stefan B. Lawrenson, Lucy A. Arkinstall, Rachel K. O'Reilly, and Jeffrey C. Foster. Self-assembled nanostructures from amphiphilic block copolymers prepared via ring-opening metathesis polymerization (ROMP). *Progress in Polymer Science*, 107:101278, 2020. 12

[73] Wolfgang G. Glasser, Rajai H. Atalla, John Blackwell, Malcolm M. Brown, Walther Burchard, Alfred D. French, Dieter O. Klemm, and Yoshiharu Nishiyama. About the structure of cellulose: Debating the Lindman hypothesis. *Cellulose*, 19(3):589–598, 2012. 12

[74] Marc Kostag, Martin Gericke, Thomas Heinze, and Omar A. El Seoud. *Twenty-five years of cellulose chemistry: innovations in the dissolution of the biopolymer and its transformation into esters and ethers*, volume 26. Springer Netherlands, 2019. 13

[75] Horace G. Deming. Some new solvents for cellulose and their action on this substance. *Journal of the American Chemical Society*, 33(9):1515–1525, 1911. 13

[76] Sanghamitra Sen, James D. Martin, and Dimitris S. Argyropoulos. Review of cellulose non-derivatizing solvent interactions with emphasis on activity in inorganic molten salt hydrates. *ACS Sustainable Chemistry and Engineering*, 1(8):858–870, 2013. 13

[77] Vladimír Raus, Adriana Šturcová, Jiří Dybal, Miroslav Šlouf, Taťána Vacková, Petr Šálek, Libor Kobera, and Petr Vlček. Activation of cellulose by 1,4-dioxane for dissolution in N,N-dimethylacetamide/LiCl. *Cellulose*, 19(6):1893–1906, 2012. 13

[78] Yuri Nishiwaki-Akine, Sui Kanazawa, Takashi Uneyama, Koh Hei Nitta, Ryoko Yamamoto-Ikemoto, and Takashi Watanabe. Transparent Woody Film Made by Dissolution of Finely Divided Japanese Beech in Formic Acid at Room Temperature. *ACS Sustainable Chemistry and Engineering*, 5(12):11536–11542, 2017. 13

[79] Charles L. McCormick and Peter A. Callais. Derivatization of cellulose in lithium chloride and N-N-dimethylacetamide solutions. *Polymer*, 28(13):2317–2323, 1987. 13

[80] Tim Liebert, Friedrich Schiller, and D Jena. Cellulose Solvents – Remarkable History, Bright Future. *Cellulose Solvents: For Analysis, Shaping and Chemical Modification*, pages 3–54, 2010. 13

[81] H. Chanzy, E. Maia, and S. Pérez. Cellulose organic solvents. III. The structure of the N-methylmorpholine N-oxide–trans-1,2-cyclohexanediol complex. *Acta Crystallographica Section B Structural Crystallography and Crystal Chemistry*, 38(3):852–855, 1982. 13

[82] Thomas Heinze and Andreas Koschella. Solvents applied in the field of cellulose chemistry: a mini review. *Polímeros*, 15(2):84–90, 2005. xii, 14, 17

[83] Richard P Swatloski, Scott K Spear, John D Holbrey, and Robin D Rogers. ILcellulose.pdf. *Journal of the American Chemical Society*, pages 4974–4975, 2002. 15

[84] Khashayar Ghandi. A Review of Ionic Liquids, Their Limits and Applications. *Green and Sustainable Chemistry*, 04(01):44–53, 2014. 15

[85] Robin D. Rogers. Materials science: Reflections on ionic liquids. *Nature*, 447(7147):917–918, 2007. 15

[86] Kun Dong, Suojiang Zhang, and Jianji Wang. Understanding the hydrogen bonds in ionic liquids and their roles in properties and reactions. *Chemical Communications*, 52(41):6744–6764, 2016. 15, 115, 116

[87] Natalia V. Plechkova and Kenneth R. Seddon. Applications of ionic liquids in the chemical industry. *Chemical Society Reviews*, 37(1):123–150Plechkova, N. V., & Seddon, K. R. (2008). A, 2008. 15

[88] Keith E. Gutowski. Industrial uses and applications of ionic liquids. *Physical Sciences Reviews*, 3(5):1–10, 2018. 15

[89] Thomas Welton. Room-Temperature Ionic Liquids. Solvents for Synthesis and Catalysis. *Chemical Reviews*, 99(8):2071–2083, 1999. 15

[90] Niklas Meine, Flavio Benedito, and Roberto Rinaldi. Thermal stability of ionic liquids assessed by potentiometric titration. *Green Chemistry*, 12(10):1711–1714, 2010. 15, 16

[91] Robin D. Rogers and Kenneth R. Seddon. Ionic Liquids - Solvents of the Future? *Science*, 302(5646):792–793, 2003. 15

[92] Sebastian Ahrens, Anke Peritz, and Thomas Strassner. Tunable aryl alkyl ionic liquids (TAAILs): The next generation of ionic liquids. *Angewandte Chemie - International Edition*, 48(42):7908–7910, 2009. 15

[93] N. Liu, Z. Li, S. Chen, and H. Wang. Novel fibres prepared by cellulose diacetate using ionic liquid as plasticiser. *Materials Research Innovations*, 19:S9295–S9298, 2015. 15

[94] Brooks D. Rabideau, Animesh Agarwal, and Ahmed E. Ismail. The role of the cation in the solvation of cellulose by imidazolium-based ionic liquids. *Journal of Physical Chemistry B*, 118(6):1621–1629, 2014. 15

[95] Dan Xu, Qiwei Yang, Baogen Su, Zongbi Bao, Qilong Ren, and Huabin Xing. Enhancing the basicity of ionic liquids by tuning the cation-anion interaction strength and via the anion-tethered strategy. *Journal of Physical Chemistry B*, 118(4):1071–1079, 2014. 15

[96] Tom Welton. Ionic liquids: a brief history. *Biophysical Reviews*, 10(3):691–706, 2018. 16

[97] M Shukla, S Saha. A Comparative Study of Piperidinium and Imidazolium Based Ionic Liquids: Thermal, Spectroscopic and Theoretical Studies. *Intech*, 2016. 16

[98] Stephen M. Green, Michael E. Ries, Jamie Moffat, and Tatiana Budtova. NMR and Rheological Study of Anion Size Influence on the Properties of Two Imidazolium-based Ionic Liquids. *Scientific Reports*, 7(1):1–12, 2017. 16

[99] Michael E. Ries, Asanah Radhi, Alice S. Keating, Owen Parker, and Tatiana Budtova. Diffusion of 1-ethyl-3-methyl-imidazolium acetate in glucose, cellobiose, and cellulose solutions. *Biomacromolecules*, 15(2):609–617, 2014. 16

[100] Michael E. Ries, Asanah Radhi, Stephen M. Green, Jamie Moffat, and Tatiana Budtova. Microscopic and Macroscopic Properties of Carbohydrate Solutions in the Ionic Liquid 1-Ethyl-3-methyl-imidazolium Acetate. *Journal of Physical Chemistry B*, 122(37):8763–8771, 2018. 16

[101] Kim Anh Le, Romain Sescousse, and Tatiana Budtova. Influence of water on cellulose-EMIMAc solution properties: A viscometric study. *Cellulose*, 19(1):45–54, 2012. 16

[102] André Pinkert, Kenneth N. Marsh, Shusheng Pang, and Mark P. Staiger. Ionic liquids and their interaction with cellulose. *Chemical Reviews*, 109(12):6712–6728, 2009. 16, 23

[103] Richard P. Swatloski, Scott K. Spear, John D. Holbrey, and Robin D. Rogers. Dissolution of cellose with ionic liquids. *Journal of the American Chemical Society*, 124(18):4974–4975, 2002. 16

[104] N. Mohd, S. F.S. Draman, M. S.N. Salleh, and N. B. Yusof. Dissolution of cellulose in ionic liquid: A review. *AIP Conference Proceedings*, 1809, 2017. 16

[105] Matthew T. Clough, Karolin Geyer, Patricia A. Hunt, Sunghee Son, Uwe Vagt, and Tom Welton. Ionic liquids: Not always innocent solvents for cellulose. *Green Chemistry*, 17(1):231–243, 2015. 17

[106] Martin Gericke, Tim Liebert, Omar A.El Seoud, and Thomas Heinze. Tailored media for homogeneous cellulose chemistry: Ionic liquid/co-solvent mixtures. *Macromolecular Materials and Engineering*, 296(6):483–493, 2011. 17

[107] Marc Kostag, Kerstin Jedvert, Christian Achtel, Thomas Heinze, and Omar A. El Seoud. Recent advances in solvents for the dissolution, shaping and derivatization of cellulose: Quaternary ammonium electrolytes and their solutions in water and molecular solvents. *Molecules*, 23(3):1–39, 2018. 17

[108] Airong Xu, Lili Cao, Bingjun Wang, and Junying Ma. Dissolution behavior of cellulose in il + dmso solvent: Effect of alkyl length in imidazolium cation on cellulose dissolution. *Advances in Materials Science and Engineering*, 2015, 2015. 17

[109] Mai N. Nguyen, Udo Kragl, Dirk Michalik, Ralf Ludwig, and Dirk Hollmann. The Effect of Additives on the Viscosity and Dissolution of Cellulose in Tetrabutylphosphonium Hydroxide. *ChemSusChem*, 12(15):3458–3462, 2019. 17

[110] Ran Liu, Juan Zhang, Shuang Sun, Yuhang Bian, and Yanhui Hu. Dissolution and recovery of cellulose from pine wood bits in ionic liquids and a co-solvent component mixed system. *Journal of Engineered Fibers and Fabrics*, 14, 2019. 17

[111] Airong Xu, Yajuan Zhang, Yang Zhao, and Jianji Wang. Cellulose dissolution at ambient temperature: Role of preferential solvation of cations of ionic liquids by a cosolvent. *Carbohydrate Polymers*, 92(1):540–544, 2013. 17, 102

[112] Chandrabhan Verma, Ankush Mishra, S. Chauhan, Pratibha Verma, Vandana Srivastava, M. A. Quraishi, and E. E. Ebenso. Dissolution of cellulose in ionic liquids and their mixed cosolvents: A review. *Sustainable Chemistry and Pharmacy*, 13(July):100162, 2019. 17

[113] Omar A. El Seoud, Ludmila C. Fidale, Naiara Ruiz, Maria Luiza O. D'Almeida, and Elisabete Frollini. Cellulose swelling by protic solvents: Which properties of the biopolymer and the solvent matter? *Cellulose*, 15(3):371–392, 2008. 17

[114] Ximing Zhang, Tianjiao Qu, Nathan S. Mosier, Lujia Han, and Weihua Xiao. Cellulose modification by recyclable swelling solvents. *Biotechnology for Biofuels*, 11(1):1–13, 2018. 17

[115] Yuling Zhao, Xiaomin Liu, Jianji Wang, and Suojiang Zhang. Insight into the cosolvent effect of cellulose dissolution in imidazolium-based ionic liquid systems. *Journal of Physical Chemistry B*, 117(30):9042–9049, 2013. xii, 18, 101

[116] Daniel J. Eyckens, Baris Demir, Tiffany R. Walsh, Tom Welton, and Luke C. Henderson. Determination of Kamlet-Taft parameters for selected solvate ionic liquids. *Physical Chemistry Chemical Physics*, 18(19):13153–13157, 2016. 18

[117] Jong Min Lee, Sebastian Ruckes, and John M. Prausnitz. Solvent polarities and Kamlet-Taft parameters for ionic liquids containing a pyridinium cation. *Journal of Physical Chemistry B*, 112(5):1473–1476, 2008. 18

[118] Chenchen Zhu, Anastasia Koutsomitopoulou, Jeroen Van Duijneveldt, and Kevin Potter. Study of co-solvent effect on the dissolution of cellulose in ionic liquid and the properties of regenerated cellulose fibres. *ICCM International Conferences on Composite Materials*, 2017-Augus(August):12–20, 2017. 18

[119] Lauri K.J. Hauru, Michael Hummel, Alistair W.T. King, Ilkka Kilpeläinen, and Herbert Sixta. Role of solvent parameters in the regeneration of cellulose from ionic liquid solutions. *Biomacromolecules*, 13(9):2896–2905, 2012. 18

[120] Lina Zhang, Yuan Mao, Jinping Zhou, and Jie Cai. Effects of coagulation conditions on the properties of regenerated cellulose films prepared in NaOH/Urea aqueous solution. *Industrial and Engineering Chemistry Research*, 44(3):522–529, 2005. 18

[121] Krishna M. Gupta, Zhongqiao Hu, and Jianwen Jiang. Cellulose regeneration from a cellulose/ionic liquid mixture: The role of anti-solvents. *RSC Advances*, 3(31):12794–12801, 2013. 18

[122] B. Meenatchi, V. Renuga, and A. Manikandan. Cellulose dissolution and regeneration using various imidazolium based protic ionic liquids. *Journal of Molecular Liquids*, 238:582–588, 2017. 19

[123] Krishna M. Gupta, Zhongqiao Hu, and Jianwen Jiang. Molecular insight into cellulose regeneration from a cellulose/ionic liquid mixture: Effects of water concentration and temperature. *RSC Advances*, 3(13):4425–4433, 2013. xii, 19, 134

[124] K. G. Bogolitsyn, D. V. Ovchinnikov, P. A. Kaplitsin, A. S. Druzhinina, A. E. Parshina, E. V. Shul'gina, M. P. Semushina, and L. A. Aleshina. Isolation and Structural Characterization of Cellulose from Arctic Brown Algae. *Chemistry of Natural Compounds*, 53(3):533–537, 2017. 19

[125] Yong Bum Park, Kabindra Kafle, Christopher M. Lee, Daniel J. Cosgrove, and Seong H. Kim. Does cellulose II exist in native alga cell walls? Cellulose structure of Derbesia cell walls studied with SFG, IR and XRD. *Cellulose*, 22(6):3531–3540, 2015. 19

[126] Xiaoyan Tan, Ling Chen, Xiaoxi Li, and Fengwei Xie. Effect of anti-solvents on the characteristics of regenerated cellulose from 1-ethyl-3-methylimidazolium acetate ionic liquid. *International Journal of Biological Macromolecules*, 124:314–320, 2019. 20

[127] Rasike De Silva, Kylie Vongsanga, Xungai Wang, and Nolene Byrne. Cellulose regeneration in ionic liquids: factors controlling the degree of polymerisation. *Cellulose*, 22(5):2845–2849, 2015. 20

[128] Chihiro Yamane, Hitomi Miyamoto, Daichi Hayakawa, and Kazuyoshi Ueda. Folded-chain structure of cellulose II suggested by molecular dynamics simulation. *Carbohydrate Research*, 379:30–37, 2013. xii, 20

[129] V Frolov. Strength of a composite material for structural applications. (2):218–224, 1987. 21

[130] M. Herráez, A. Fernández, C. S. Lopes, and C. González. Strength and toughness of structural fibres for composite material reinforcement. *Philosophical Transactions of the Royal Society A: Mathematical, Physical and Engineering Sciences*, 374(2071), 2016. 21

[131] Francesco Tornabene. Journal of Composites Science: A New Journal for Composite Materials, Structures and Experiments. *Journal of Composites Science*, 1(1):1, 2017. 21

[132] M. J. Biercuk, M. C. Llaguno, M. Radosavljevic, J. K. Hyun, A. T. Johnson, and J. E. Fischer. Carbon nanotube composites for thermal management. *Applied Physics Letters*, 80(15):2767–2769, 2002. 21

[133] Ismail Ibrahim Marhoon. Mechanical properties of composite materials reinforced with short random glass fibers and ceramics particles. *International Journal of Scientific and Technology Research*, 7(8):50–53, 2018. 21

[134] M. Haghshenas. Metal–Matrix Composites. *Reference Module in Materials Science and Materials Engineering*, (October 2015):0–28, 2016. 21

[135] Galvan, Federico R., Violeta Barranco, Juan C. Galvan, Santiago Batlle, Sebastian FeliuFajardo, and García. Introduction to Composite Materials. *Intech*, i(tourism):13, 2016. 21

[136] Karl Ulrich Kainer. *Basics of Metal Matrix Composites*. 2006. xii, 22

[137] Technische Universiteit Eindhoven and Document Version. *The potential of flax fibres as reinforcement for composite materials The Potential of Flax*

Fibres as Reinforcement for Composite Materials. Number 2004. 2020. 22, 23

[138] Cileide Maria Medeiros Coelho, Cláudia de Mattos Bellato, Julio Cesar Pires Santos, Edwin Moises Marcos Ortega, and Siu Mui Tsai. Effect of phytate and storage conditions on the development of the ‘ hard-to-cook ’. *Journal of the science of food and agriculture*, 1243(December 2005):1237–1243, 2007. 22

[139] Maya Jacob John and Sabu Thomas. Biofibres and biocomposites. *Carbohydrate Polymers*, 71(3):343–364, 2008. 22

[140] Koronis Georgios, Arlindo Silva, and Samuel Furtado. Applications of Green Composite Materials. *Biodegradable Green Composites*, (February):312–337, 2016. 22

[141] Nattakan Soykeabkaew, Noriko Arimoto, Takashi Nishino, and Ton Peijs. All-Cellulose Composites by Surface Selective Dissolution of Aligned Lignocellulosic Fibres. 2011. 22

[142] P. J. Hine, I. M. Ward, R. H. Olley, and D. C. Bassett. The hot compaction of high modulus melt-spun polyethylene fibres. *Journal of Materials Science*, 28(2):316–324, 1993. 22

[143] C. Narayan, G. Madhu, and B. Diksha. Evaluation of Biodegradability Characteristics of Cellulose-based Film as per IS / ISO 14855-1. *Applied Packaging reserarch*, 11(3), 2.:12–23, 2019. 23

[144] Vijay Kumar Thakur, Manju Kumari Thakur, and Raju Kumar Gupta. Review: Raw Natural Fiber-Based Polymer Composites. *International Journal of Polymer Analysis and Characterization*, 19(3):256–271, 2014. 23

[145] Ying Wang and Yulin Deng. The kinetics of cellulose dissolution in sodium hydroxide solution at low temperatures. *Biotechnology and Bioengineering*, 102(5):1398–1405, 2009. 23, 65, 138

[146] Mark D Lingwood, Zhiyang Zhang, Bryce E Kidd, and Kacey B Mccreary. polymer ion conductor †‡. pages 4283–4285, 2013. 23, 67

[147] Ke Chen, Weixin Xu, Yun Ding, Ping Xue, Pinghou Sheng, Hui Qiao, and Jimin He. Hemp-based all-cellulose composites through ionic liquid promoted controllable dissolution and structural control. *Carbohydrate Polymers*, 235(November 2019):116027, 2020. 23, 112

[148] Junhua Zhang, Jingqiang Zhang, Lu Lin, Tianming Chen, Jun Zhang, Shijie Liu, Zhenjiang Li, and Pingkai Ouyang. Dissolution of microcrystalline cellulose in phosphoric acid-molecular changes and kinetics. *Molecules*, 14(12):5027–5041, 2009. 23, 65, 138

[149] Marcus Eriksen, Laurent C.M. Lebreton, Henry S. Carson, Martin Thiel, Charles J. Moore, Jose C. Borerro, Francois Galgani, Peter G. Ryan, and Julia Reisser. Plastic Pollution in the World's Oceans: More than 5 Trillion Plastic Pieces Weighing over 250,000 Tons Afloat at Sea. *PLoS ONE*, 9(12):1–15, 2014. 24

[150] Kara Lavender Law, Skye E. Morét-Ferguson, Deborah S. Goodwin, Erik R. Zettler, Emelia Deforce, Tobias Kukulka, and Giora Proskurowski. Distribution of surface plastic debris in the eastern pacific ocean from an 11-year data set. *Environmental Science and Technology*, 48(9):4732–4738, 2014. 24

[151] Marcus Eriksen, Nikolai Maximenko, Martin Thiel, Anna Cummins, Gwen Lattin, Stiv Wilson, Jan Hafner, Ann Zellers, and Samuel Rifman. Plastic pollution in the South Pacific subtropical gyre. *Marine Pollution Bulletin*, 68(1-2):71–76, 2013. 24

[152] David K.A. Barnes, Francois Galgani, Richard C. Thompson, and Morton Barlaz. Accumulation and fragmentation of plastic debris in global environments. *Philosophical Transactions of the Royal Society B: Biological Sciences*, 364(1526):1985–1998, 2009. 24

[153] Takashi Nishino, Ikuyo Matsuda, and Koichi Hirao. All-cellulose composite. *Macromolecules*, 37(20):7683–7687, 2004. 24

[154] M. Mat Salleh, K. Magniez, S. Pang, J. W. Dormanns, and M. P. Staiger. Parametric optimization of the processing of all-cellulose composite lami-

nae. *Advanced Manufacturing: Polymer and Composites Science*, 3(2):73–79, 2017. 24

[155] Takashi Nishino and Noriko Arimoto. All-cellulose composite prepared by selective dissolving of fiber surface. *Biomacromolecules*, 8(9):2712–2716, 2007. 24

[156] Michael P.M. Dicker, Peter F. Duckworth, Anna B. Baker, Guillaume Francois, Mark K. Hazzard, and Paul M. Weaver. Green composites: A review of material attributes and complementary applications. *Composites Part A: Applied Science and Manufacturing*, 56:280–289, 2014. 24

[157] N. P.G. Suardana, A. Abdalla, H. K. Kim, K. S. Choi, and Jae Kyoo Lim. Mechanical properties and biodegradability of green composites based on polylactic-acid polymer. *ICCM International Conferences on Composite Materials*, 2011. 24

[158] Rie Nakamura and Anil Netravali. *Fully Biodegradable "Green" Composites*, pages 431–463. 2013. 24

[159] Cristina Luján-Ornelas, Leonor Patricia Güereca, María Laura Franco-García, and Michiel Heldeweg. A life cycle thinking approach to analyse sustainability in the textile industry: A literature review. *Sustainability (Switzerland)*, 12(23):1–19, 2020. 24

[160] Samir I. Ionic Liquids Recycling for Reuse. *Ionic Liquids - Classes and Properties*, (June), 2011. 24

[161] Mingkun Yang, Wenwen Zhao, Shizeng Wang, Changyuan Yu, Seema Singh, Blake Simmons, and Gang Cheng. Dimethyl sulfoxide assisted dissolution of cellulose in 1-ethyl-3-methylimidazoium acetate: small angle neutron scattering and rheological studies. *Cellulose*, 26(4):2243–2253, 2019. 27

[162] Xiaoyan Tan, Xiaoxi Li, Ling Chen, and Fengwei Xie. in 1-ethyl-3-methylimidazolium acetate ionic. pages 27584–27593, 2016. 27

[163] Gang Cheng, Patanjali Varanasi, Rohit Arora, Vitalie Stavila, Blake A. Simmons, Michael S. Kent, and Seema Singh. Impact of ionic liquid pretreatment conditions on cellulose crystalline structure using 1-ethyl-3-methylimidazolium acetate. *Journal of Physical Chemistry B*, 116(33):10049–10054, 2012. 27

[164] Craig A. Hall, Kim A. Le, Cyrielle Rudaz, Asanah Radhi, Christopher S. Lovell, Robin A. Damion, Tatiana Budtova, and Michael E. Ries. Macroscopic and microscopic study of 1-Ethyl-3-methyl-imidazolium acetate-water mixtures. *Journal of Physical Chemistry B*, 116(42):12810–12818, 2012. 27, 35, 116

[165] Morteza Jabbari, Negar Khosravi, Mina Feizabadi, and Davood Ajloo. Solubility temperature and solvent dependence and preferential solvation of citrus flavonoid naringin in aqueous DMSO mixtures: an experimental and molecular dynamics simulation study. *RSC Advances*, 7(24):14776–14789, 2017. 35

[166] Valter H. Carvalho-Silva, Nayara D. Coutinho, and Vincenzo Aquilanti. Temperature dependence of rate processes beyond Arrhenius and eyring: Activation and transitivity. *Frontiers in Chemistry*, 7(MAY):1–11, 2019. 35

[167] Wu Xu, Emanuel I. Cooper, and C. Austen Angell. Ionic liquids: Ion mobilities, glass temperatures, and fragilities. *Journal of Physical Chemistry B*, 107(25):6170–6178, 2003. 35

[168] Ravi Jethra. Temperature Measurement Applications in Power Plants. 2009. 35

[169] S Wolf, J Lambauer, U Fahl, M Blesl, and A Voss. Industrial heat pumps in Germany - potentials , technological development and application examples. *ECEEE 2012 Summer Study - Energy Efficiency in Industry*, (September):543–550, 2012. 35

[170] Shudhakar Gopalsamy. Analysis of heat loss in kiln in cement industry - A review. 2016. 35

[171] G. Alonso-Ramírez, F. Sánchez-Minero, Jorge Ramírez, Rogelio Cuevas-Garcia, and N. Moreno-Montiel. Analysis of the thermal hydrocracking of heavy fuel oil. *Petroleum Science and Technology*, 36(7):507–513, 2018. 35

[172] Pooja Bhatt and Alka Goe. Carbon Fibres: Production, Properties and Potential Use. *Material Science Research India*, 14(1):52–57, 2017. 36

[173] Bo Tang, Ying Wang, Li Hu, Lianbin Lin, Chenxi Ma, Chongyin Zhang, Yonggen Lu, Kai Sun, and Xinfeng Wu. Preparation and properties of lightweight carbon/carbon fiber composite thermal field insulation materials for high-temperature furnace. *Journal of Engineered Fibers and Fabrics*, 14, 2019. 36

[174] Ronalds Gonzalez, Hasan Jameel, Hou-Min Chang, Trevor Treasure, Adrian Pirraglia, and Daniel Saloni. Thermo-mechanical pulping as a pretreatment for agricultural biomass for biochemical conversion. *BioResources*, 6, 2011. 36

[175] L. G. Anikanova and N. V. Dvoretskii. Effect of Doubly Charged Ion Additives on the Activity and Chemical Stability of Catalytically Active Potassium Ferrites. *Catalysis in Industry*, 12(3):201–206, 2020. 36

[176] A. S. Klimenko, D. V. Andreev, S. A. Prikhod'ko, A. G. Gribovskii, L. L. Makarshin, and N. Yu Adonin. Using a Microchannel Reactor to Optimize the Production of 1-Alkyl-3-Methylimidazolium Chlorides. *Catalysis in Industry*, 12(3):207–215, 2020. 36

[177] Abdelaziz Abdelaziz, Rahman Saidur, and Saad Mekhilef. A review on energy saving strategies in industrial sector. *Renewable and Sustainable Energy Reviews*, 15:150–168, 2011. 36

[178] Feng Chen, Daisuke Sawada, Michael Hummel, Herbert Sixta, and Tatiana Budtova. Swelling and dissolution kinetics of natural and man-made cellulose fibers in solvent power tuned ionic liquid. *Cellulose*, 5, 2020. 36, 66, 105, 113

[179] Yoshiharu Nishiyama, Junji Sugiyama, Henri Chanzy, and Paul Langan. Crystal Structure and Hydrogen Bonding System in Cellulose Iα from Syn-

chrotron X-ray and Neutron Fiber Diffraction. *Journal of the American Chemical Society*, 125(47):14300–14306, 2003. 36

[180] Ran Liu, Juan Zhang, Shuang Sun, Yuhang Bian, and Yanhui Hu. Dissolution and recovery of cellulose from pine wood bits in ionic liquids and a co-solvent component mixed system. *Journal of Engineered Fibers and Fabrics*, 14, 2019. 36

[181] Masae Takahashi and Haruko Takenaka. Transition from cellulose i family to cellulose ii family. *Polymer Journal*, 19(7):855–861, 1987. 36

[182] Ge Wang, Sheldon Q Shi, Jinwu Wang, Yan Yu, Shuangping Cao, and Haitao Cheng. Tensile properties of four types of individual cellulosic fibres. *Wood and Fiber Science*, 43(4):353–364, 2011. 37

[183] Hao Wang, Peter Schubel, Xiaosu Yi, Jin Zhu, Chad Ulven, and Yiping Qiu. Green composite materials. *Advances in Materials Science and Engineering*, 2015, 2015. 37

[184] Xiaohui Ju, Mark Bowden, Elvie E. Brown, and Xiao Zhang. An improved X-ray diffraction method for cellulose crystallinity measurement. *Carbohydrate Polymers*, 123:476–481, 2015. 38

[185] Petru. Poni, Florin. Ciolacu, and Valentin. Popa. Amorphous Cellulose – Structure and characterisation. *Cellulose chemistry and technology*, 2010. 39

[186] C. Trilokesh and Kiran Babu Uppuluri. Isolation and characterization of cellulose nanocrystals from jackfruit peel. *Scientific Reports*, 9(1):1–8, 2019. 39

[187] Christopher J. Garvey, Ian H. Parker, and George P. Simon. On the interpretation of X-ray diffraction powder patterns in terms of the nanostructure of cellulose I fibres. *Macromolecular Chemistry and Physics*, 206(15):1568–1575, 2005. 41

[188] Kazuho Daicho, Tsuguyuki Saito, Shuji Fujisawa, and Akira Isogai. The Crystallinity of Nanocellulose: Dispersion-Induced Disordering of the Grain

Boundary in Biologically Structured Cellulose. *ACS Applied Nano Materials*, 1(10):5774–5785, 2018. 41

[189] Carlos Driemeier and Guilherme A. Calligaris. Theoretical and experimental developments for accurate determination of crystallinity of cellulose i materials. *Journal of Applied Crystallography*, 44(1):184–192, 2011. 41

[190] Alfred D. French. Idealized powder diffraction patterns for cellulose polymorphs. *Cellulose*, 21(2):885–896, 2014. 41

[191] Lynne H. Thomas, V. Trevor Forsyth, Anne Martel, Isabelle Grillo, Clemens M. Altaner, and Michael C. Jarvis. Diffraction evidence for the structure of cellulose microfibrils in bamboo, a model for grass and cereal celluloses. *BMC Plant Biology*, 15(1):1–7, 2015. 41

[192] Akira Isogai, Makoto Usuda, Takashi Kato, Toshiyuki Uryu, and Rajai H. Atalla. Solid-State CP/MAS 13C NMR Study of Cellulose Polymorphs. *Macromolecules*, 22(7):3168–3172, 1989. 44

[193] Hanbin Liu, Gang Cheng, Michael Kent, Vitalie Stavila, Blake A. Simmons, Kenneth L. Sale, and Seema Singh. Simulations reveal conformational changes of methylhydroxyl groups during dissolution of cellulose Iβ in ionic liquid 1-ethyl-3- methylimidazolium acetate. *Journal of Physical Chemistry B*, 116(28):8131–8138, 2012. xiv, 47

[194] Malgorzata Zimniewska. Antioxidant activity of fibres originating from traditional varieties of polish flax plants. *Fibres and Textiles in Eastern Europe*, 23(6):41–47, 2015. 49, 71

[195] Libo Yan, Nawawi Chouw, and Krishnan Jayaraman. Flax fibre and its composites - A review. *Composites Part B: Engineering*, 56:296–317, 2014. 49, 71

[196] Changquan Sun. True density of microcrystalline cellulose. *Journal of Pharmaceutical Sciences*, 94(10):2132–2134, 2005. 52

[197] P H Hermans and D Vermaas. Fibers. I. Introduction and Experiments. 1(3):149–155, 1946. 52

[198] Julie Grandgirard, Denis Poinsot, Liliane Krespi, Jean Pierre Nénon, and Anne Marie Cortesero. Costs of secondary parasitism in the facultative hyperparasitoid Pachycrepoideus dubius: Does host size matter? *Entomologia Experimentalis et Applicata*, 103(3):239–248, 2002. 52

[199] Mustafa Aslan, Gary Chinga-Carrasco, Bent F. Sørensen, and Bo Madsen. Strength variability of single flax fibres. *Journal of Materials Science*, 46(19):6344–6354, 2011. 53, 86, 138

[200] Donald Plazek. Time-temperature superposition-a users guide. (November), 2017. 61

[201] Marnix van Gurp and Jo Palmen. Time-temperature superposition for polymeric blends. *J Rheol Bull*, 65(May):5–8, 1998. 61

[202] Takuya Uto, Kazuya Yamamoto, and Jun-ichi Kadokawa. Cellulose Crystal Dissolution in Imidazolium-Based Ionic Liquids: A Theoretical Study. *Physical Chemistry B*, (122):258 – 266, 2018. 65

[203] Bharat Manna and Amit Ghosh. Dissolution of cellulose in ionic liquid and water mixtures as revealed by molecular dynamics simulations. *Journal of Biomolecular Structure and Dynamics*, 37(15):3987–4005, 2019. 65, 117

[204] Rajdeep Singh Payal and Sundaram Balasubramanian. Dissolution of cellulose in ionic liquids: An ab initio molecular dynamics simulation study. *Physical Chemistry Chemical Physics*, 16(33):17458–17465, 2014. 65

[205] Martin Kihlman, Bruno F. Medronho, Anabela L. Romano, Ulf Germgård, and Bjorn Lindman. Cellulose dissolution in an alkali based solvent: Influence of additives and pretreatments. *Journal of the Brazilian Chemical Society*, 24(2):295–303, 2013. 65, 118

[206] Martin Brehm, Martin Pulst, Jörg Kressler, and Daniel Sebastiani. Triazolium-Based Ionic Liquids: A Novel Class of Cellulose Solvents. *Journal of Physical Chemistry B*, 123(18):3994–4003, 2019. 65, 138

[207] Martin Brehm, Julian Radicke, Martin Pulst, Farzaneh Shaabani, Daniel Sebastiani, and Jörg Kressler. Dissolving Cellulose in 1,2,3-Triazolium-

and Imidazolium-Based Ionic Liquids with Aromatic Anions. *Molecules*, 25:3539, 2020. 66, 138

[208] Karine Charlet, Jean Paul Jernot, Moussa Gomina, Laurent Bizet, and Joël Bréard. Mechanical properties of flax fibers and of the derived unidirectional composites. *Journal of Composite Materials*, 44(24):2887–2896, 2010. 86, 138

[209] Yonghui Zhou, Mizi Fan, and Lihui Chen. Interface and bonding mechanisms of plant fibre composites: An overview. *Composites Part B: Engineering*, 101:31–45, 2016. 88

[210] Koon Yang Lee, Yvonne Aitomäki, Lars A. Berglund, Kristiina Oksman, and Alexander Bismarck. On the use of nanocellulose as reinforcement in polymer matrix composites. *Composites Science and Technology*, 105:15–27, 2014. 88

[211] A. J. Kinloch, B. R.K. Blackman, and W. S. Teo. The adhesive bonding of polymeric matrix composites. *ICCM International Conferences on Composite Materials*, (July), 2009. 88

[212] Sai Venkatesh, Micholas Dean, Shih-hsien Liu, Takat B Rawal, Yunqiao Pu, and Riddhi Shah. Deconstruction of biomass enabled by local demixing of cosolvents at cellulose and lignin surfaces. 117(29):16776–16781, 2020. 101

[213] Yu Cao and Huimin Tan. Improvement of alkali solubility of cellulose with enzymatic treatment. *Applied Microbiology and Biotechnology*, 70(2):176–182, 2006. 101

[214] Kara Capriotti and Joseph A. Capriotti. Dimethyl sulfoxide: History, chemistry, and clinical utility in dermatology. *Journal of Clinical and Aesthetic Dermatology*, 5(9):24–26, 2012. 102

[215] M. Verheijen, M. Lienhard, Y. Schrooders, O. Clayton, R. Nudischer, S. Boerno, B. Timmermann, N. Selevsek, R. Schlapbach, H. Gmuender, S. Gotta, J. Geraedts, R. Herwig, J. Kleinjans, and F. Caiment. DMSO induces drastic changes in human cellular processes and epigenetic landscape in vitro. *Scientific Reports*, 9(1):1–12, 2019. 102

[216] S. E. Gad and D. W. Sullivan. Dimethyl Sulfoxide (DMSO). *Encyclopedia of Toxicology: Third Edition*, 30:166–168, 2014. 102

[217] Yuling Zhao, Jianji Wang, Huiyong Wang, Zhiyong Li, Xiaomin Liu, and Suojiang Zhang. Is There Any Preferential Interaction of Ions of Ionic Liquids with DMSO and H 2 O ? A Comparative Study from MD Simulation. 2015. xix, 102, 116, 117

[218] Jean Michel Andanson, Emilie Bordes, Julien Devémy, Fabrice Leroux, Agilio A.H. Pádua, and Margarida F.Costa Gomes. Understanding the role of co-solvents in the dissolution of cellulose in ionic liquids. *Green Chemistry*, 16(5):2528–2538, 2014. 102, 105

[219] Asanah Radhi, Kim Anh Le, Michael E. Ries, and Tatiana Budtova. Macroscopic and microscopic study of 1-ethyl-3-methyl-imidazolium acetate-DMSO mixtures. *Journal of Physical Chemistry B*, 119(4):1633–1640, 2015. 102, 104

[220] Daryl B. Wong, Kathleen P. Sokolowsky, Musa I. El-Barghouthi, Emily E. Fenn, Chiara H. Giammanco, Adam L. Sturlaugson, and Michael D. Fayer. Water dynamics in water/DMSO binary mixtures. *Journal of Physical Chemistry B*, 116(18):5479–5490, 2012. xviii, 103

[221] Ivana A. Borin. Molecular association between water and dimethyl sulfoxide in solution: A molecular dynamics simulation study. *Journal of Chemical Physics*, 110(13):6412–6420, 1999. 103

[222] Ortrud Aschenbrenner, Somsak Supasitmongkol, Marie Taylor, and Peter Styring. Measurement of vapour pressures of ionic liquids and other low vapour pressure solvents. *Green Chemistry*, 11(8):1217–1221, 2009. 103

[223] Alan N. Campbell. The density and vapour pressure of dimethylsulfoxide at various temperatures and the (hypothetical) critical density. *Canadian Journal of Chemistry*, 57(6):705–707, 1979. 103

[224] Fei Lu, Lejun Wang, Chao Zhang, Bowen Cheng, Ruigang Liu, and Yong Huang. Influence of temperature on the solution rheology of cellu-

lose in 1-ethyl-3-methylimidazolium chloride/dimethyl sulfoxide. *Cellulose*, 22(5):3077–3087, 2015. 104

[225] Yuxia Lv, Jin Wu, Jinming Zhang, Yanhua Niu, Chen Yang Liu, Jiasong He, and Jun Zhang. Rheological properties of cellulose/ionic liquid/dimethylsulfoxide (DMSO) solutions. *Polymer*, 53(12):2524–2531, 2012. 105

[226] Sadiye Velioglu, Xun Yao, Julien Devémy, M. Goktug Ahunbay, S. Birgul Tantekin-Ersolmaz, Alain Dequidt, Margarida F. Costa Gomes, and Agílio A.H. Pádua. Solvation of a cellulose microfibril in imidazolium acetate ionic liquids: Effect of a cosolvent. *Journal of Physical Chemistry B*, 118(51):14860–14869, 2014. 109

[227] Asanah Radhi, Kim Anh Le, Michael E. Ries, and Tatiana Budtova. Macroscopic and microscopic study of 1-ethyl-3-methyl-imidazolium acetate-DMSO mixtures. *Journal of Physical Chemistry B*, 119(4):1633–1640, 2015. 111, 139

[228] Jinming Zhang, Lili Xu, Jian Yu, Jin Wu, Xiaoyu Zhang, Jiasong He, and Jun Zhang. Understanding cellulose dissolution: effect of the cation and anion structure of ionic liquids on the solubility of cellulose. *Science China Chemistry*, 59(11):1421–1429, 2016. 111

[229] Jean Michel Andanson, Emilie Bordes, Julien Devémy, Fabrice Leroux, Agilio A.H. Pádua, and Margarida F.Costa Gomes. Understanding the role of co-solvents in the dissolution of cellulose in ionic liquids. *Green Chemistry*, 16(5):2528–2538, 2014. 112

[230] Celine Cuissinat and Patrick Navard. Swelling and dissolution of cellulose part 1: Free floating cotton and wood fibres in N-methylmorpholine-N-oxide-water mixtures. *Macromolecular Symposia*, 244:1–18, 2006. 113

[231] Celine Cuissinat and Patrick Navard. Swelling and dissolution of cellulose part II: Free floating cotton and wood fibres in NaOH-water-additives systems. *Macromolecular Symposia*, 244:19–30, 2006. 113

[232] Céline Cuissinat, Patrick Navard, and Thomas Heinze. Swelling and dissolution of cellulose. Part IV: Free floating cotton and wood fibres in ionic liquids. *Carbohydrate Polymers*, 72(4):590–596, 2008. 113

[233] Céline Cuissinat, Patrick Navard, and Thomas Heinze. Swelling and dissolution of cellulose, Part V: Cellulose derivatives fibres in aqueous systems and ionic liquids. *Cellulose*, 15(1):75–80, 2008. 113

[234] Takashi Nishino, Ikuyo Matsuda, and Koichi Hirao. All-cellulose composite. *Macromolecules*, 37(20):7683–7687, 2004. 114

[235] W Gindl and J Keckes. All-cellulose nanocomposite. 46:10221–10225, 2005. 114

[236] Feng Chen, Daisuke Sawada, Michael Hummel, Herbert Sixta, and Tatiana Budtova. Unidirectional all-cellulose composites from flax via controlled impregnation with ionic liquid. *Polymers*, 12(5):6–8, 2020. 114

[237] Tobias Zentel, Viviane Overbeck, Dirk Michalik, Oliver Kühn, and Ralf Ludwig. Hydrogen bonding in protic ionic liquids: Structural correlations, vibrational spectroscopy, and rotational dynamics of liquid ethylammonium nitrate. *arXiv*, 2017. 115

[238] Mateusz Z. Brela, Piotr Kubisiak, and Andrzej Eilmes. Understanding the Structure of the Hydrogen Bond Network and Its Influence on Vibrational Spectra in a Prototypical Aprotic Ionic Liquid. *Journal of Physical Chemistry B*, 122(41):9527–9537, 2018. 115

[239] Chieu D. Tran, Silvia H. De Paoli Lacerda, and Daniel Oliveira. Absorption of water by room-temperature ionic liquids: Effect of anions on concentration and state of water. *Applied Spectroscopy*, 57(2):152–157, 2003. 115

[240] María Villanueva and Carlos Fernández-Leira. Water Absorption and Effect of Water Content on Viscosity and Electrical Conductivity of Two Diethylmethylammonium Ionic Liquids. *Proceedings*, 9(1):58, 2018. 115, 117

[241] S. Cuadrado-Prado, M. Domínguez-Pérez, E. Rilo, S. García-Garabal, L. Segade, C. Franjo, and O. Cabeza. Experimental measurement of the hygroscopic grade on eight imidazolium based ionic liquids. *Fluid Phase Equilibria*, 278(1-2):36–40, 2009. 115, 116

[242] Zhaoyang Ju, Weihua Xiao, Xingmei Lu, Xiaomin Liu, Xiaoqian Yao, Xiaochun Zhang, and Suojiang Zhang. Theoretical studies on glycolysis of poly(ethylene terephthalate) in ionic liquids. *RSC Advances*, 8(15):8209–8219, 2018. 116

[243] Kim Anh Le, Romain Sescousse, and Tatiana Budtova. Influence of water on cellulose-EMIMAc solution properties: A viscometric study. *Cellulose*, 19(1):45–54, 2012. 116

[244] Bruno Medronho, Anabela Romano, Maria Graça Miguel, Lars Stigsson, and Björn Lindman. Rationalizing cellulose (in)solubility: Reviewing basic physicochemical aspects and role of hydrophobic interactions. *Cellulose*, 19(3):581–587, 2012. 116

[245] L. Cammarata, S. G. Kazarian, P. A. Salter, and T. Welton. Molecular states of water in room temperature ionic liquids. *Physical Chemistry Chemical Physics*, 3(23):5192–5200, 2001. 116

[246] Benoît J.C. Duchemin, Mark P. Staiger, and Roger H. Newman. High-temperature viscoelastic relaxation in all-cellulose composites. *Macromolecular Symposia*, 340(1):52–58, 2014. 116

[247] J. Jacquemin, P. Husson, A. A.H. Padua, and V. Majer. Density and viscosity of several pure and water-saturated ionic liquids. *Green Chemistry*, 8(2):172–180, 2006. 116

[248] Kim Anh Le, Romain Sescousse, and Tatiana Budtova. Influence of water on cellulose-EMIMAc solution properties: A viscometric study. *Cellulose*, 19(1):45–54, 2012. 117

[249] Mathieu Mazza, Dan Andrei Catana, Carlos Vaca-Garcia, and Christine Cecutti. Influence of water on the dissolution of cellulose in selected ionic liquids. *Cellulose*, 16(2):207–215, 2009. 117

[250] Celine Cuissinat and Patrick Navard. Swelling and Dissolution of Cellulose Part 1: Free Floating Cotton and Wood Fibres in N-Methylmorpholine-N-oxide–Water Mixtures. *Macromolecular Symposia*, 244(1):1–18, dec 2006. 117

[251] Carina Olsson, Alexander Idström, Lars Nordstierna, and Gunnar Westman. Influence of water on swelling and dissolution of cellulose in 1-ethyl-3-methylimidazolium acetate. *Carbohydrate Polymers*, 99:438–446, 2014. 117

[252] Ramakrishnan Parthasarathi, Kanagasabai Balamurugan, Jian Shi, Venkatesan Subramanian, Blake A Simmons, and Seema Singh. Theoretical Insights into the Role of Water in the Dissolution of Cellulose Using IL/Water Mixed Solvent Systems. 2015. 117

[253] Ana Espert, Francisco Vilaplana, and Sigbritt Karlsson. Comparison of water absorption in natural cellulosic fibres from wood and one-year crops in polypropylene composites and its influence on their mechanical properties. *Composites Part A: Applied Science and Manufacturing*, 35(11):1267–1276, 2004. 117

[254] Liping Guo, Wenxiao Zhang, Wei Sun, Bo Chen, and Yafan Liu. High-temperature performance and multiscale damage mechanisms of hollow cellulose fiber-reinforced concrete. *Advances in Materials Science and Engineering*, 2016(January 2015), 2016. 117

[255] Iwan H. Sahputra, Alessio Alexiadis, and Michael J. Adams. Effects of Moisture on the Mechanical Properties of Microcrystalline Cellulose and the Mobility of the Water Molecules as Studied by the Hybrid Molecular Mechanics–Molecular Dynamics Simulation Method. *Journal of Polymer Science, Part B: Polymer Physics*, 57(8):454–464, 2019. 117

[256] N. L. Salmen and E. L. Back. Influence of Water on the Glass Transition Temperature of Cellulose., 1977. 117

[257] Patrice Kreiml. Investigation of water absorption of cellulose fibers by gravimetric analysis and atomic force microscopy by. pages 1–71, 2016. 117

[258] M. D. Deshpande, Ralph H. Scheicher, Rajeev Ahuja, and Ravindra Pandey. Binding strength of sodium ions in cellulose for different water contents. *Journal of Physical Chemistry B*, 112(30):8985–8989, 2008. xix, 118

[259] Isabelle Pochard, Sara Frykstrand, Olle Ahlström, Johan Forsgren, and Maria Strømme. Water and ion transport in ultra-adsorbing porous magnesium carbonate studied by dielectric spectroscopy. *Journal of Applied Physics*, 115(4), 2014. 118

[260] Jameel Park, Sunkyu, Venditti, Richard. Hard-to-remove water in cellulose fibers characterized by thermal analysis: A model for the drying of wood-based fibers. *Tappi Journal*, 6. 10-16(6), 2007. 118

[261] Hugh O'Neill, Sai Venkatesh Pingali, Loukas Petridis, Junhong He, Eugene Mamontov, Liang Hong, Volker Urban, Barbara Evans, Paul Langan, Jeremy C. Smith, and Brian H. Davison. Dynamics of water bound to crystalline cellulose. *Scientific Reports*, 7(1):1–13, 2017. 118

[262] K. Nakamura, T. Hatakeyama, and H. Hatakeyama. Studies on bound water of cellulose by differential scanning calorimetry. pages 607–613, 1981. 118

[263] Ali Chami Khazraji and Sylvain Robert. Interaction effects between cellulose and water in nanocrystalline and amorphous regions: A novel approach using molecular modeling. *Journal of Nanomaterials*, 2013, 2013. xix, 118, 119

[264] Frédéric Roig, Eric Dantras, Jany Dandurand, and Colette Lacabanne. Influence of hydrogen bonds on glass transition and dielectric relaxations of cellulose. *Journal of Physics D: Applied Physics*, 44(4), 2011. 118

[265] Hanbin Liu, Kenneth L. Sale, Blake A. Simmons, and Seema Singh. Molecular Dynamics Study of Polysaccharides in Binary Solvent Mixtures of an Ionic Liquid and Water. *The Journal of Physical Chemistry B*, 115(34):10251–10258, sep 2011. xix, 119, 120

[266] Dean C. Dibble, Chenlin Li, Lan Sun, Anthe George, Aurelia Cheng, Özgül Persil Çetinkol, Peter Benke, Bradley M. Holmes, Seema Singh, and

Blake A. Simmons. A facile method for the recovery of ionic liquid and lignin from biomass pretreatment. *Green Chemistry*, 13(11):3255–3264, 2011. 121

[267] Andrei Filippov, Oleg N. Antzutkin, and Faiz Ullah Shah. Rapid carbene formation increases ion diffusivity in an imidazolium acetate ionic liquid confined between polar glass plates. *Physical Chemistry Chemical Physics*, 21(40):22531–22538, 2019. 121

[268] Carmine D'Agostino, Mick D. Mantle, Claire L. Mullan, Christopher Hardacre, and Lynn F. Gladden. Diffusion, Ion Pairing and Aggregation in 1-Ethyl-3-Methylimidazolium-Based Ionic Liquids Studied by 1H and 19F PFG NMR: Effect of Temperature, Anion and Glucose Dissolution. *ChemPhysChem*, 19(9):1081–1088, 2018. xix, 121

[269] Christopher S. Lovell, Adam Walker, Robin A. Damion, Asanah Radhi, Steven F. Tanner, Tatiana Budtova, and Michael E. Ries. Influence of cellulose on ion diffusivity in 1-ethyl-3-methyl-imidazolium acetate cellulose solutions. *Biomacromolecules*, 11(11):2927–2935, 2010. xix, 121, 122

[270] Brooks D. Rabideau and Ahmed E. Ismail. Mechanisms of hydrogen bond formation between ionic liquids and cellulose and the influence of water content. *Physical Chemistry Chemical Physics*, 17(8):5767–5775, 2015. 134